Towards a structural understanding of plant-microbiota interactions using cryo-EM techniques

Liedtke, J.

Citation

Liedtke, J. (2025, December 4). *Towards a structural understanding of plant-microbiota interactions using cryo-EM techniques*. Retrieved from https://hdl.handle.net/1887/4284406

Towards a Structural Understanding of Plant–Microbiota Interactions using cryo-EM Techniques

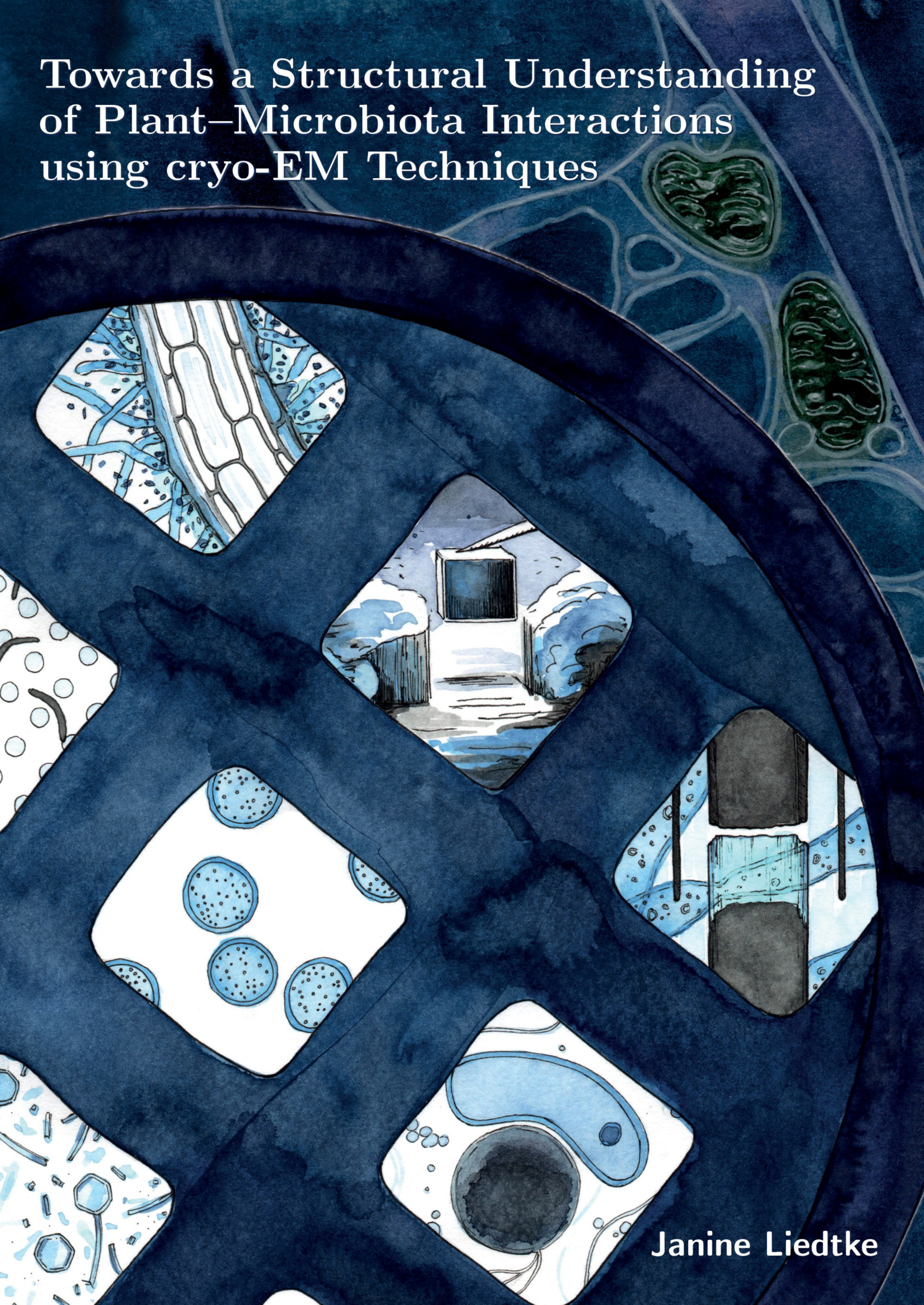

Janine Liedtke

Towards a Structural Understanding of Plant–Microbiota Interactions using cryo-EM Techniques

Janine Liedtke

PhD. Thesis, Leiden University, 2025

Towards a Structural Understanding of Plant–Microbiota Interactions using cryo-EM Techniques

ISBN	978-94-6496-461-5
Printed by:	Gildeprint, gildeprint.nl
Cover design:	Lucia Berti, orangethetiger.com
Layout:	Janine Liedtke

An electronic version of this dissertation is available at
http://openaccess.leidenuniv.nl.

Towards a Structural Understanding of Plant–Microbiota Interactions using cryo-EM Techniques

Proefschrift

ter verkrijging van
de graad van doctor aan de Universiteit Leiden,
op gezag van rector magnificus prof.dr.ir. H. Bijl,
volgens besluit van het college voor promoties
te verdedigen op donderdag 4 december 2025
klokke 10:00 uur

door

Janine Liedtke

geboren te Berlin, Duitsland.

Promotores

Prof. dr. A. Briegel
Prof. dr. G. P. van Wezel

Promotiecommissie:

Prof. dr. A. H. Meijer	
Prof. dr. D. Claessen	
Dr. J. Willemse	
Prof. dr. C. M. J. Pieterse	Utrecht University
Dr. S. C. Howes	Utrecht University

… für Papa

Denn die einen sind im Dunkeln
Und die anderen sind im Licht.
Und man siehet die im Lichte
Die im Dunkeln sieht man nicht.

Brecht

CONTENTS

1

General Introduction and Thesis Outline

INTRODUCTION

As Newton once said, "What we know is a drop, what we do not know is an ocean". Just as this applies to the universe it also holds true for our understanding of plant-associated microbiota. The microbiota refers to an assembly of living microorganisms within a spatially and temporally defined environment, including bacteria, archaea, fungi, algae, and small protists. According to Berg *et al.* (2020) [1], it also includes mobile genetic elements such as transposons, viruses, and bacteriophages. The diversity and function of microbial communities are crucial for almost all ecosystems, as they play a central role in geochemical cycles, drive nutrient dynamics, and help maintain ecological balance. Consequently, they also play a vital role in their host plant by enhancing nutrient uptake, mitigating the effects of abiotic stressors such as heat and drought, and providing protection against pathogens.

Rather than being passive recipients of microbial colonization and interactions, plants actively shape their microbiota through their physiology, root architecture, and a process known as the "cry-for-help" strategy [2, 3]. In this view, plants release specific compounds in the form of root exudates, which allow them to influence both the composition and functional properties of their microbiota while selectively attracting and enriching beneficial microorganisms. These interactions can extend to the point where they lead to the development of disease-suppressive soils, a phenomenon that has been shown to persist across plant generations through soil-borne legacy effects [4].

However, plant-microbiota interactions expand beyond the soil-root interface (the rhizosphere). In fact, they occur throughout the entire plant, including the internal tissues. Microorganisms that colonize plant tissues without causing harm or negatively affecting their host are referred to as endophytes. These endophytic communities are present in all plant compartments, but their composition varies between tissues. More specifically, plants show selective colonization patterns, favouring certain microbes while restricting others [5]. The microbiotas in different plant tissues are not isolated but interact and influence each other, including those on the plant surface and in the rhizosphere, leading to a complex network of interactions that shape the plant's microbial community. In recent years, the plant-associated microbiota has gained attention for its potential to enhance plant health and resilience, offering a sustainable alternative to chemical-based agricultural practices. Various strategies have been explored, including microbiome transplantation, microbial inoculants, and the use of microbial and plant extracts [6, 7]. In this context, studies have revealed that a subset of core microorganisms (also referred to as key microorganisms) is necessary for the long-term success of plant-microbiota treatments [1]. Core microorganisms are members of the microbiota that are consistently present and associated with specific host genotypes or environmental conditions. They play a critical role in maintaining both host and microbiota fitness. Thus, identifying these core microorganisms, as well as understanding their interactions with the host plant and the surrounding microbiota, is essential for optimizing plant health and productivity. Just as plants shape their microbiota through metabolites, microorganisms use their own metabolites to interact between species, influencing microbiota composition and function as well as host plant physiology.

Since bacteria dominate the plant-microbiota, they have become the main focus of research in the identification of potential core microbiota members. The most abundant bacterial phyla include Proteobacteria, Firmicutes, Bacteroidota (formerly known as Bacteroidetes), and Actinobacteria. Particularly, members of the Bacteroidota phylum have gained interest, as the majority of these bacteria tend to engage in mutualistic interactions, either directly supporting their host or indirectly benefiting other microbiota members [8]. For example, the strains *Chitinophaga pinensis* and *Flavobacterium anhuiense* are known to enhance plant resilience to fungal pathogens as well as abiotic stressors such as heat and drought. Besides its role in plant resilience, *C. pinensis* exhibits the ability to degrade complex polysaccharides, which may contribute to its ecological function within the plant-associated microbiota. However, the precise role of these metabolic capabilities in microbiota interactions and plant association remains unclear. Additionally, it is not yet known how these microorganisms establish stable associations within the plant microbiota despite environmental challenges. Further research is needed to determine whether, in addition to chemical signals, possible physical nanostructures facilitate host interactions and to what extent *C. pinensis* morphology influences its ability to interact with its microbiota and host plants.

The dynamic interactions within the microbiota, as well as between the host and its microbiota, are complex and influence each other's physiology. To maintain balance and ensure long-term persistence despite environmental challenges, regulatory mechanisms are essential to prevent the overgrowth of single species. In this context, bacteriophages play a crucial role, as proposed by the 'kill the winner' theory, which suggests that bacteriophages target bacterial populations that thrive under certain conditions [9]. Bacteriophages, or phages for short, are viruses that exclusively infect bacteria to hijack their replication system for propagation. They follow two distinct replication strategies, the lytic and the lysogenic replication cycle. In the lytic cycle, the phage attaches to the susceptible host bacteria to inject its genome into the cytoplasm and redirects the host's replication system to produce and assemble new virions. The cycle ends with the release of phages through cell lysis. In contrast, during the lysogenic cycle, the phage genome integrates into the host genome, and remains dormant as a prophage, replicating along with the host. Once triggered, the prophage switches to the lytic cycle, leading to host lysis and the release of new phages. Beyond their regulatory function within microbiotas, phages can also benefit their host by introducing additional metabolic capabilities, conferring antimicrobial resistance, or modulating bacterial morphology in ways that provide competitive advantages within the microbial communities [10–12]. However, little is known about phages that target Bacteroidota nor is it clear to what extent they play a role in the mutualistic endophytic lifestyle of Bacteroidota.

In addition to bacteria, fungi also play an important role in the plant-associated microbiota, with arbuscular mycorrhizal fungi (AMF) in particular considered core microorganisms. AMF have been closely associated with plants for more than 450 million years, forming symbiotic relationships with more than 72% of vascular plant species. This symbiosis is so intimate that the plant allows the fungus to invade its cells and form a specialized structure for nutrient exchange, known as an arbuscule [13]. AMFs help plants to overcome site-specific resource limitations through their extensive hyphal network that connects host plants across species. Interestingly, this fungal network not only facilitates resource exchange between hosts but may also serve as a potential transport route for phages and bacteria. However, little is known about how these exchanges of resources and transport processes are regulated, or which structures are involved.

Although microbial interactions play a crucial ecological role, their ultrastructural basis remains largely unknown. Cryo-electron microscopy (cryo-EM) has emerged as a powerful tool for visualizing the structural interaction between host and microbe in their native cellular environment. The technique offers the possibility to gain insight into the nanoscale features involved in microbial interactions in a near-native state and in three dimensions. However, to date, cryo-EM has been primarily used to study the ultrastructure of isolated proteins and single cells. Cryo-EM is based on freezing samples in vitreous ice [14]. To achieve this, samples are rapidly frozen using plunge freezing, where they are submerged in liquid ethane cooled by liquid nitrogen (-194 °C). This rapid process prevents the formation of crystalline ice, instead forming electron permeable amorphous (vitreous) ice that preserves the sample in its native hydrated state without structural alteration.

Initially, cryo-EM imaging was limited to samples with a maximum thickness of 500 nm due to electron beam penetration constraints. The development of focus ion beam scanning electron microscopy (FIB/SEM) overcame this limitation by utilizing an ion beam to selectively thin a predefined rectangular area (lamella) to 200 nm, making it electron permeable and thus accessible for high-resolution imaging. This advancement allowed cryo-EM imaging of samples with an initial thickness of up to 20 μm for the first time. Another breakthrough came with high-pressure freezing (HPF), which overcame the vitrification limitations of plunge freezing.

Due to water's poor thermal conductivity, plunge freezing is limited to sample thinner than ~10 μm, as heat cannot dissipate fast enough, leading to the formation of crystalline instead of vitrified ice. HPF addresses this issue by applying 210 MPa (~2100 bar) of pressure during vitrification, preventing water expansion, lowering the freezing point, and improving cooling efficiency. This allows the vitrification of thicker samples up to ~200 μm [15, 16].

However, increasing sample thickness introduced new challenges, particularly in lamella preparation, as prolonged thinning times increased the risk of de-vitrification, crystalline ice contamination, and beam-induced damage.

In recent years, these limitations have been overcome through advancements in cryo-lift-out techniques and the refinement of FIB/SEM into plasma-FIB/SEM (PFIB/SEM), significantly reducing thinning times and improving sample integrity. The combination of these methods has already enabled the acquisition of high-resolution cryo-EM images from metazoan tissue. While these developments represent a promising step forward, sample preparation for cryo-EM imaging remains an ongoing challenge. It is still unclear whether these techniques can be adapted to visualize the ultrastructure of plant tissue in a near-native state with nanoscale detail as well, along with the microbiota residing within, and their interactions.

THESIS OUTLINE

This thesis was carried out as part of the NWO-GROOT project "Unwiring beneficial functions and regulatory networks in the plant endosphere" (OCENW.GROOT.2019.063), which investigates how endophytic microorganisms contribute to plant health and resilience.

The focus of this thesis is the structural investigation of key members of endophytic microbiota and the development of a workflow for large-volume sample preparation, making plant tissue accessible for cryo-EM imaging and data collection. The structural analysis provided new insights into the morphology of *C. pinensis* and the cellular organization of AMF hyphae.

Chapter 2 reviews the technical developments in cryo-electron tomography and the novel insights they have provided into the structural organization of bacteria. In addition, the combination of methods and techniques in sample preparation, sample volume thinning and lamella preparation, along with automated data acquisition as well and advances in data processing, has enabled a deeper investigation of bacterial molecular machines regarding their structural organization and function.

In **Chapter 3**, the morphological structures in *C. pinensis* were explored in detail to identify potential adaptations that facilitate host-microbiota interactions. This revealed a drastic transition in morphology, from long filamentous to small spherical cells. However, the spherical cells did not exhibit characteristic features of spores, dormant cells, or persister cells, such as increased resistance or structural modifications of the cell wall. The potential advantages of this reduced cell size were analysed further and revealed that small spherical cells exhibit hitchhiking behaviour in the presence of motile bacteria.

Chapter 4 focuses on, optimization of the vitrification procedure for AMF samples and on the development of a workflow to prepare AMF hyphal network samples and spores for cryo-EM imaging. This study presents the first insights into vitrified AMF hyphae, revealing their structural organization in unprecedented detail. This workflow supports future research in elucidating the ultrastructure of AMF hyphal networks and investigating the mechanisms of their trading system, as well as its regulatory processes, at the nanoscale level.

Chapter 5 describes the development of a workflow for large-volume sample preparation of plant roots, making them accessible for cryo-EM imaging and tomography data collection. Additionally, root tissue from different plant species was tested, leading to the identification of root-organs as an optimal model system for this workflow. Notably, root-organs are already well-established models for studying plant-microbiota interactions. This workflow enables the vitrification of root tissue for cryo-EM imaging, providing the first insights into plant-microbiota interactions in root tissue at the nanoscale level. Future research will benefit from this workflow, as well as from the identification of root-organs as a suitable model system for nanoscale plant-microbiota interaction studies.

Chapter 6 describes the challenges in detecting and isolating lytic phages from soil samples, as well as the distribution of temperate phages (prophages) among endophytic Bacteroidota strains. This study revealed that all tested strains harboured active and inducible prophage sequences with a broad host range. The results provide a solid foundation for future research to investigate the potential role of active and cryptic prophage sequences in the endophytic lifestyle of Bacteroidota members.

Chapter 7, discusses and summarizes the outcomes of this thesis and their broader implications. Additionally, it addresses challenges in large-volume sample preparation for cryo-EM imaging and outlines future perspectives.

2

HOW ADVANCES IN CRYO-ELECTRON TOMOGRAPHY HAVE CONTRIBUTED TO OUR CURRENT VIEW OF BACTERIAL CELL BIOLOGY

Advancements in the field of cryo-electron tomography have greatly contributed to our current understanding of prokaryotic cell organization and revealed intracellular structures with remarkable architecture. In this review, we present some of the prominent advancements in cryo-electron tomography, illustrated by a subset of structural examples to demonstrate the power of the technique. More specifically, we focus on technical advances in automation of data collection and processing, sample thinning approaches, correlative cryo-light and electron microscopy, and sub-tomogram averaging methods. In turn, each of these advances enabled new insights into bacterial cell architecture, cell cycle progression, and the structure and function of molecular machines. Taken together, these significant advances within the cryo-electron tomography workflow have led to a greater understanding of prokaryotic biology. The advances made the technique available to a wider audience and more biological questions and provide the basis for continued advances in the near future.

This chapter is based on a published article by **Liedtke, J.**, Depelteau, J. S., and Briegel, A. (2022): *How advances in cryo-electron tomography have contributed to our current view of bacterial cell biology. Journal of Structural Biology: X*, 6, 100065.

2.1 INTRODUCTION

Microscopy has played a crucial role in gaining insights into the hidden world of bacteria. The ability to directly observe live bacterial cells has allowed us to gain insight into the basic biology of these organisms, such as their shape, growth and division cycles, and motility behaviours. With the advent of traditional electron microscopy (EM), the finer structural details of bacteria became clearer: differences in cell envelope structures could be distinguished, and the intercellular contents, such as the nucleoid and storage, could be identified. However, more detailed information could not be gained due to the nature of the sample preparation; Chemical fixation, dehydration, plastic embedding, and staining of the sample largely obscured the delicate ultrastructure of the bacterial cells (Figure 2.1 A). Subsequently, the usefulness of EM was thought to be limited and significant advances in genetic engineering and the development of fluorescent tags rendered EM a niche method. Therefore, despite increasingly detailed insights into the biology of bacterial cells gained by such alternative microbiological methods, many structural aspects of bacteria remained obscure. This lack of insight is still evident in the typical cell architecture comparisons between eukaryotic and bacterial cells in textbooks. While eukaryotic cell types were known to contain a myriad of structures, such as a diverse cytoskeleton, Golgi apparatus, and mitochondria, bacterial cells were often depicted with a generic rod-shaped cell containing only a nucleoid, ribosomes, cell envelope layers, and occasional appendages (Figure 2.1 B).

The introduction of cryogenic electron tomography (cryo-ET) made it possible to elucidate the finer structural features of bacterial cells in a near-native state, in three dimensions, and at macromolecular resolution. To do this, the bacterial cells are flash-frozen on an EM support grid in a liquid-nitrogen-cooled cryogen [17]. This freezing process is so fast that water molecules do not form ice crystals. Instead, the sample is embedded in a glass-like state (referred to as vitrification) that preserves the delicate ultrastructure of the cells [14, 17]. Vitrified samples are then imaged using a cryogenic transmission electron microscope (cryo-TEM). The cryo-TEM collects a series of 2-dimensional (2D) images while the sample is being tilted with respect to the electron beam. The resulting set of images, referred to as a tilt-series, can then be computationally back-projected to generate a 3-dimensional (3D) volume of the target (referred to as a tomogram). However, the potential impact of this workflow, called cryogenic electron tomography (cryo-ET), on the current understandings of bacterial ultrastructures was not immediately realized by microbiologists. A decade after its advent, the Baumeister group first applied this technology to prokaryotic cells in 1998 [18]. Even still, only a small number of studies used this method on bacterial cells for an additional decade [19].

Today, cryo-ET is widely recognized as a powerful tool to unravel the structural aspects of microbes. This method has greatly contributed to our understanding of how microbes are structurally organized, how they grow and divide using a highly complex cytoskeleton, and how they use molecular machines such as secretion systems, cell appendages, and chemotaxis arrays to navigate and interact with the environment (Figure 2.1 C). In its early days, data collection was practically manual, requiring constant supervision. However, automation of the technique quickly advanced and the data collection process is now largely self-operating. In addition, improvements in the hardware, such as new types of

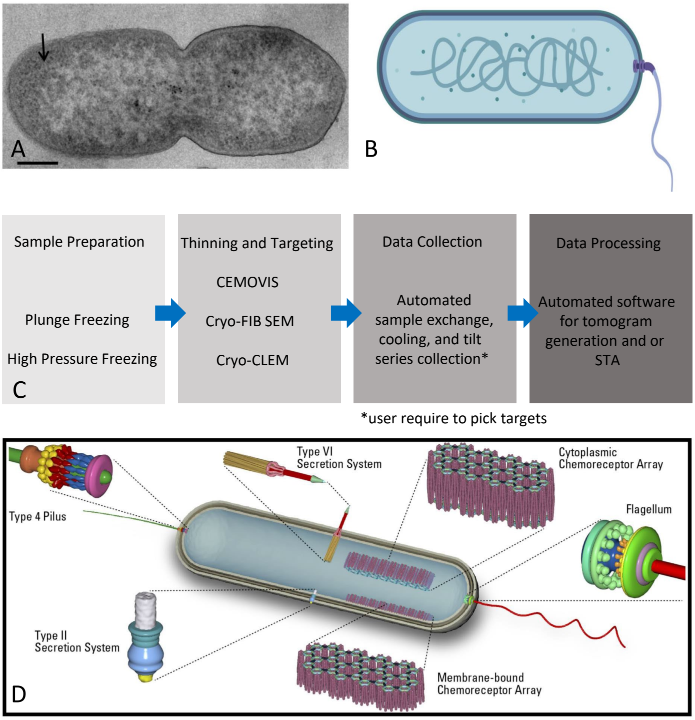

Figure 2.1: Changing view of the bacterial cell structure. (A) Traditional EM image of *Pseudomonas aeruginosa* (arrow indicates tightly packed material). Image reproduced from Latino *et al.* (2019) [20] with permission. (B) Simplified schematic of a bacterial cell, lacking structural detail (made in Biorender.com). (C) Workflow of cryo-electron tomography. (D) Modern interpretation of a bacterium, containing selected structural features (schematic by Robert van Sluis).

cameras/detectors, the ability to section cryo-preserved samples at cryogenic temperatures, the development of correlative techniques with fluorescent light microscopy, and new software packages to analyse the data, aided in raising cryo-ET to a key method in the prokaryotic biology toolbox. In this review, we will highlight some of the important insights gained by the improvements of cryo-ET. However, cryo-ET has so extensively contributed to our current understanding of the structure of bacterial cells that we will only highlight some selected structural examples.

2.2 CRYO-ET AUTOMATION EXEMPLIFIED INSIGHT INTO BACTERIAL CYTOSKELETON

Following its proof of concept, cryo-ET was first practically used to describe novel cell attachment structures [18, 21]. These studies relied on only a handful of tomograms since data collection and processing were time-consuming and mostly manual. Specifically, data collection had to be supervised to ensure proper imaging conditions throughout the tilt series, such as accurate target tracking and maintaining defocus settings of the individual images. The subsequent processing of the 2D images to generate the tomograms was equally taxing. For instance, the early software programs, such as the EM software [22], required the user to manually track gold particles in each image. These gold beads are typically added to the sample before freezing to allow for an accurate alignment of the images of a tilt series, which is necessary for a precise 3D reconstruction.

This highly manual workflow resulted in a low throughput of data acquisition and processing, which in turn greatly limited insights into many aspects of bacterial cell biology. The development of robust cryo-ET data collection software provided the means for a higher sample throughput (for example TOM toolbox, UCSFtomo, FEI software, serialEM) [23–25]. In addition, technical improvements such as maintaining liquid nitrogen cooling of the samples enabled automation of tilt-series collection without supervision. Automation increased the number of tilt-series collected, which necessitated the creation of automated post-processing routines such as IMOD and Warp [26, 27]. These new softwares allowed for an automatic transfer of the images to the processing platform, and subsequent automatic processing using batch routines. A good description of the data processing steps can be found for example in the article of Baldwin *et al.* (2018) [28]. In addition to the technical developments directly related to instrumentation and software, advances in computational processing power with improved CPUs and GPUs, and the advent of direct electron detectors capable of collecting movies with high speed and improved accuracy, have aided in the increasing automation of the workflow as well as greatly improved image quality [28]. Together, these improvements not only result in more reliable data but also increase the amount of higher resolution information available for analysis. These advancements directly led to a better understanding of the components of a complex system such as the bacterial cytoskeleton.

In eukaryotes, it has been long known that the cytoskeleton is an intracellular network system of filaments and tubules which defines the form and structure of a cell and gives them coherence in its spatial-temporal operations [29]. In contrast, bacteria were thought to lack cytoskeletal elements and therefore were devoid of any internal order. Later, it was discovered that bacteria contain homologs of eukaryotic cytoskeletal filaments, but many questions regarding their detailed structure and function remained. Homologs of all three main protein classes of the eukaryotic cytoskeleton were discovered in bacteria, for example, FtsZ (tubulin-like), MreB (actin-like), and CreS (intermediate filament-like). Of these, the first described protein of the bacterial cytoskeleton was FtsZ. This protein was shown to be essential for cell division in most bacteria. Bi & Lutkenhaus (1991) [30] were the first to visualize the FtsZ filaments by immuno-electron microscopy (Figure 2.2 A). In this study, the FtsZ filament localization at the division site was revealed. With this information, the authors proposed an FtsZ assembly model that proposed a complete ring formation of FtsZ filaments. However, the question of if the FtsZ filaments formed such a continuous ring or not remained.

While cryo-ET is very powerful in resolving structures in intact cells, determining their identity remains a challenge. At present, there are no easily applicable tags comparable to the fluorescent markers used in light microscopy. Instead, the identity of a structure of interest can be indirectly determined by imaging a variety of mutant strains, where the protein of interest is altered in some way. This includes overexpression, deletion or depletions, non-hydrolysable variants, or chemicals affecting the protein polymerization. Images collected of these samples are then compared to the wild-type strain to convincingly identify the target structure. This requires a large amount of data to be collected and therefore requires a large degree of automation in the workflow to be feasible. This approach was used in an early cryo-ET study that compared cryo-ET data of several different FtsZ mutants in *Caulobacter crescentus*. This research gained insight into the time of appearance of FtsZ filaments in the cell cycle, their position, orientation, as well as their number and length. The cryo-ET data revealed that FtsZ forms filaments that are relatively short (~100 nm) and overlapping in vivo. The insights led to the proposition of the 'iterative pinching model' [31].

While early studies proposed that FtsZ does not form a complete ring in *C. crescentus*, its presence in other bacteria remained disputed [32, 33]. The reason for this lies in the 'missing wedge' artefact of the cryo-ET process: during tilt series collection, the sample can only be tilted +/- 60, resulting in missing information obtained from greater tilt angles. In reality, it obscures features perpendicular to the electron beam, which is most obvious in the absence of discernable features on the top and bottom of a cell. As a consequence, the FtsZ ring could not be visualized as a complete ring [32].

Newer cryo-ET studies support the idea that a complete FtsZ ring is not needed to drive successful cell constriction and division in several species besides *C. crescentus* (Figure 2.2). Yao *et al.* (2017) [33] visualized various bacterial species in different division stages (pre-, early, mid, and post constriction stage). Additionally, they utilized an open access cryo-ET database [34] and categorized the imaged cells in the mentioned stages, ultimately identifying 159 dividing cells of 47 species. They confirmed that FtsZ filaments can indeed be found in different lengths and forms. Furthermore, they highlighted that the constriction process takes longer than the lifetime of the individual FtsZ filaments [33]. Despite all these insights, many questions remain on the cell division process, especially in the orchestration of the FtsZ ring formation and constriction in the context of the growing number of proteins that are known to be involved in this process, together called the "Divisome". Cryo-ET may also help answer these open questions in the future.

An additional cytoskeletal protein found in bacteria is the actin-like MreB, which is involved in the positioning of peptidoglycan (PG) during lateral cell-wall growth and division. For a long time, it was believed that MreB forms extended and static helical filaments. However, cryo-ET revealed that MreB forms only short filaments [35]. These conclusions were confirmed by two fluorescent light microscopy studies that visualized MreB filaments and their behaviour in vivo [36, 37]. They showed that short MreB filaments move in a helical pattern around the inner membrane in the cytoplasm, guiding the PG synthesis machinery. The question still remained: what was the composition of the extended filament? Cryo-ET later revealed that the extended helical structures are in fact artefacts of the yellow fluorescent protein (yfp) tag [38]. These research results highlight the importance of the visualization of samples by cryo-ET to gain insight into the bacterial cytoskeleton (for a detailed review see Pilhofer *et al.* (2013) [39]).

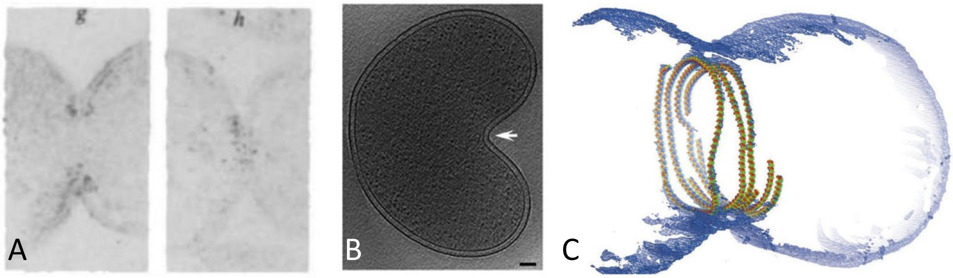

Figure 2.2: FtsZ structure; (A) comparison fro the first EM visualization of the FtsZ structure within *Escherichia coli* cell [30] with (B) the current models of symmetric constriction of a *Belliella baltica* cell (white arrow indicates the asymmetric division site) [33] and (C) a visualization of a semi atomic model of symmetric FtsZ ring constriction in a liposome [32].

2.3 CEMOVIS AS A METHOD TO VISUALIZE CELL ENVELOPE LAYERS

A limitation of EM is the thickness of the prepared samples. When samples are too large, the entire electron dose is absorbed and all structural details are lost. Therefore, various techniques were developed to gain insight into the architecture of samples with a thickness beyond the scope of plunge freezing. Plunge freezing is an ultra-rapid cryofixation, whereby a thin layer of sample on a grid is so rapidly plunge into a liquid cryogen, that no ice crystal formation appears. Several thin-sectioning methods allowed the trimming of samples suitable for EM. Early methods are conducted at room temperature and involved harsh chemical treatments. In contrast to these classical sectioning types, cryogenic electron microscopy of vitreous sections (CEMOVIS) does not require chemical fixation or embedding in resin or plastic. Instead, samples are high pressure frozen, which vitrifies samples with high pressure and liquid nitrogen temperatures. As with plunge freezing, this sample preparation method preserves the delicate structure of the biological material. The frozen sample is subsequently transferred to a cryo-ultramicrotome and sectioned with a diamond knife into cryo-EM suitable sections [40].

The key difference between these techniques lies in the sample preparation, which is either chemical or physical nature. The chemical method is strongly dependent on the chemicals used for fixation, staining, and embedding, all of which can lead to serious artefacts. For example, one of the most famous artefacts is the mesosome which had been believed to be a compartment of the bacterial cell for years [41, 42]. However, with the application of the CEMOVIS technique, it was revealed that mesosomes are artefacts caused by chemical fixation [41, 42]. The obvious advantage of CEMOVIS is that it circumvents the artefacts associated with chemical treatment. The disadvantage of CEMOVIS is that it is not possible to combine it with immunogold labelling methods for structures inside of cells. However, it is predominantly suitable for structural investigation. Another disadvantage that both sectioning methods have in common are physical artefacts caused by the mechanical stress of sectioning, for example, knife marks and compression. Bleck *et al.* (2010) [41] compared the different sectioning methods with each other and concluded that even though CEMOVIS is not an artefact-free method, it is still the preferable method.

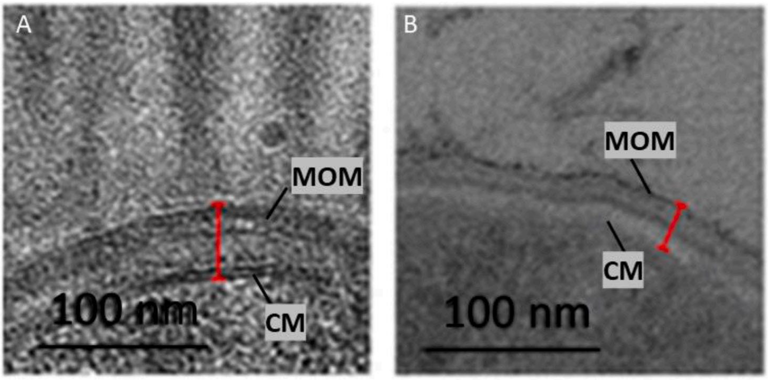

Figure 2.3: Comparative micrographs of *Mycobacteria smegmatis* cell envelope for the different sectioning types; CEMOVIS (A); and classical preparation with chemical fixation and resin embedding (B). Red line indicates the cell wall thickness, whereby the inner and outer membranes are easily detectable in A compared to B. Adapted from Bleck *et al.* (2010) [41]. CM, cytoplasmic membrane; MOM, mycobacterial outer membrane.

It provides a better understanding of biological structure within a cell and even tissue, which are usually too thick for direct imaging. For example, with CEMOVIS it was possible to image the cell envelope of mycobacteria and to confirm the existence of their unique cell envelope. The cell envelope is a multi-component, layered structure that is responsible for maintaining cell shape as well as protection from environmental stressors. Mycobacteria have an unusual outer membrane that consists mainly of mycoloic acid, a lipid that gets easily dissolved by chemical treatment. Thus, due to this characteristic, it was not possible to visualize it with the common sectioning methods and its existence was controversial until 2008 (Figure 2.3). CEMOVIS was crucial in confirming the presence of this structure.

2.4 Advances in sample thinning for cryo-ET

Since the introduction of cryo-ET, sample thickness has been a major limitation. The general rule within the community is that the maximum thickness of the sample is twice the power of the electron beam. Theoretically, this has been predicted to be slightly less, but other factors such as the contents of the sample can also play a role [43]. Thus, if you are working with a 300 keV instrument, the electrons will pass through a sample of up to 600 nm in thickness. However, it is important to consider that the increasing thickness of the sample also diminishes the availability of high-resolution information, thus limiting the questions that can be addressed.

About fifteen years ago, a technique typically used in material sciences called focused ion beam scanning electron microscopy (FIB SEM) was adapted to work at cryogenic temperatures and was shown to be suitable for vitrified biological samples [44]. Now referred to as cryo-FIB SEM, the technique preserves the vitreous nature of the sample while using the focused ion beam to systematically remove material from the sample until it is sufficiently thin. The SEM beam is used during this process to monitor the progress of the thinning process. Cryo- FIB SEM has evolved into a valuable method to thin plunge frozen samples that are otherwise too thick for cryo-ET, and has been used to study a variety of samples and biological questions [45, 46].

The power of this technique was recently demonstrated by the identification of the structural proteins associated with endospore formation. These spores are highly resistant to environmental stresses and can endure for extended periods due to a thick, protective protein coat. For some bacterial species, like *Bacillus subtilis*, this dense coat prohibited direct visualization by cryo-ET. However, Khanna *et al.* (2021) [47] were determined to understand the sporulation processes of *B. subtilis.* Previous research had shown that the process of sporulation was significantly different from the division during vegetative growth, though exactly how was unknown [48, 49]. To solve this problem, Khanna *et al.* (2021) [47] used cryo-FIB SEM to first thin the cells to approximately 200 nm, which were then subsequently imaged (Figure 2.4 A) [47]. Remarkably, they were able to show that the FtsZA division machinery is evenly distributed along the division septum in vegetative cells (Figure 2.4 B). Conversely, in sporulating cell, the FtsZA is not distributed evenly along the septum but rather located only on the mother cell side of the septum (Figure 2.4 C). Using a combination of genetic and imaging techniques, they had further shown that this asymmetry is likely due to SpoIIE localization on the spore side of the septa, which lead to an exclusion of FtsZA and resulted in a thinner division septum. Cryo-FIB SEM, followed by cryo-ET, was essential to gain this important structural insight into spore formation.

Additional advancements in cryo-FIB SEM are currently in development. For instance, most studies using this technique have involved samples that can be prepared by plunge freezing to generate tiny sample fraction, called lamella. 200 nm lamella are easily produced in samples that are less than 5-10 µm in starting thickness. The next revolution in cryo-FIB SEM will be the processing of large-volume samples that require high-pressure freezing, which currently includes thicknesses of around 250 µm. This type of sample includes small multicellular organisms such as *Caenorhabditis elegans* and bacterial biofilms [45, 50]. Two primary methods in development are the ‘lift-out’ technique using a mechanical arm called microgripper and focused ion beam milling with oxygen plasma [51–53]. Combined with the ion beam, the lift-out device allows for the excision of chunks of tissue from a large volume sample. These thinner samples are then transferred to a specialized grid for further thinning to create lamella for imaging. The oxygen plasma beam has been demonstrated to ablate larger volumes of HPF tissue without damage to the tissue and in less time, thus providing an alternative to the cryo-lift-out and current Ga+ FIB beam. These techniques have already been used in large volume samples such as *C. elegans*, however they are not yet readily available to the scientific community [52].

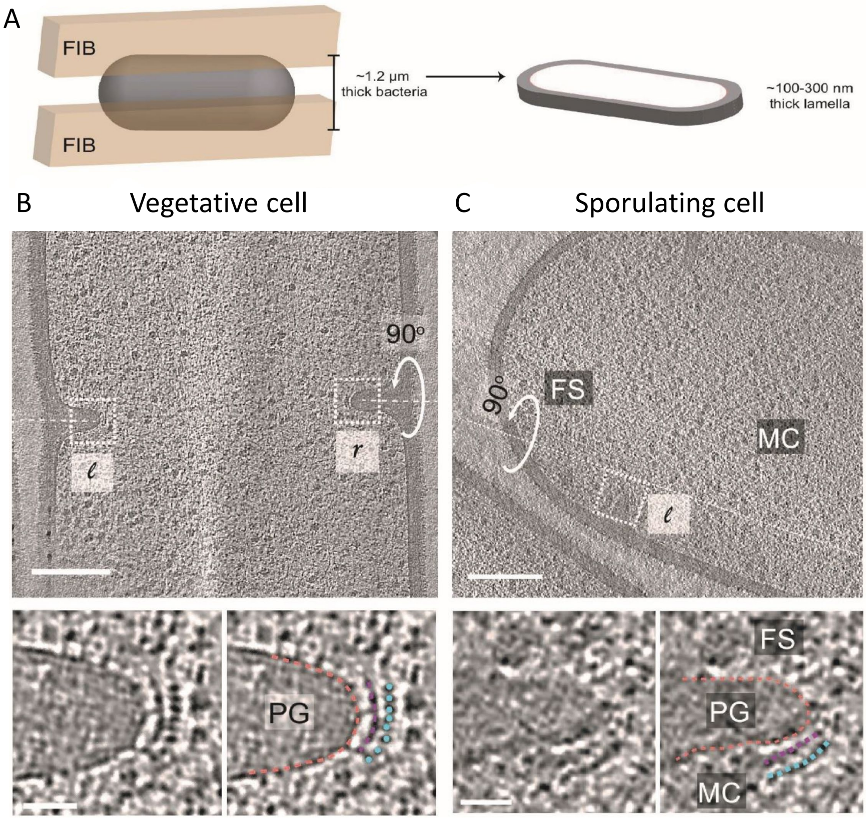

Figure 2.4: Schematic representation of cryo-FIB milling of the bacterial cell (A). (B & C) By thinning of *Bacillus subtilis* using cryo-FIB SEM, Khanna *et al.* [47] were able to identify the location of FtsZ (blue) and FtsA (purple) at the division septum for vegetative (B) and sporulating cells. Adapted from Khanna *et al.* [47].

2.5 Cryo-CLEM is a method that provides the distinction of compartments of a structure

The absence of widely applicable labels for cryo-ET to confidently identify a feature of interest in a tomogram remains a challenge. However, combining cryo-ET with fluorescence light microscopy (FLM) at both room and cryogenic temperatures (referred to as correlated light and electron microscopy, CLEM) can help to alleviate this issue. This combination allows structures of interest to be tagged with a fluorescent probe, imaged using a light microscope, and then prepared for and imaged with cryo-EM. At room temperature, challenges include the need for the sample to remain static during FLM and cryo-fixation; otherwise, the two images cannot be properly correlated. In addition, the resolution limitation of FLM often makes it very difficult to accurately identify the structure of interest. Despite these challenges, this method has been successfully used to determine the location of the chemotaxis arrays, the CTP synthase filaments, and the diffusion barriers in the bacterium *Caulobacter cresecentus* [54–56].

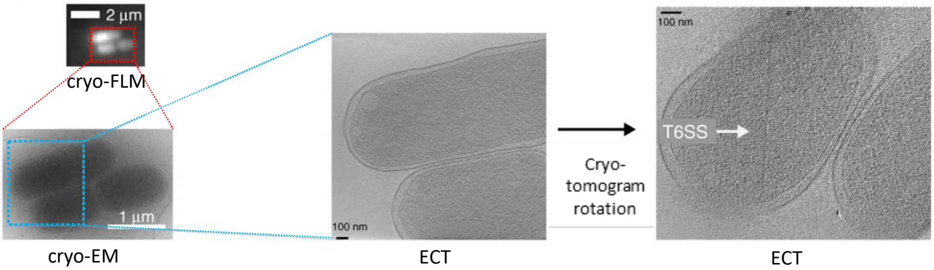

Figure 2.5: Cryo-FLM workflow used in the identification of the extended T6SS in enteroaggregative *E. coli*. The cells were first vitrified and then imaged by cryo-FLM to identify the cells that contained the Hcp1-CouAA labeled T6SS. Subsequent cryo-ET and rotation of the tomogram in the area of interest led to the visualization of the T6SS. Adapted from Szwedziak and Pilhofer (2019) [58].

With the introduction of cryogenic CLEM (cryo-CLEM), the sample is first frozen, immobilizing the structures in place, and then imaged using the typical cryo-FLM and cryo-EM workflow. This technique has been used to identify and describe several prokaryotic structures, including the MreB filaments in *C. crescentus*, and the type 6 secretion system (T6SS) [35]. First observed in Vibrio cholerae, the T6SS is a syringe-like structure found in some gram-negative bacteria [57]. The T6SS acts as a molecular needle that contains effector molecules used to stave off offending bacteria or to occupy new environmental niches. It consists of a membrane-bound inner tube and spike structure surrounded by a sheath assembly that is responsible for the contraction and injection. Bound to the membrane at the proximal end, the process of contraction results in a rearrangement of the sheath proteins causing the effectors located inside the tube to be shot into the neighbouring cell. Disassembly quickly follows, allowing the sheath subunits to be re-used in the formation of a new T6SS.

A recent example of the use of cryo-CLEM in the study of T6SS was shown by Szwedziak and Pilhofer (2019) [58]. In this study, the authors examined T6SS in enteroaggregative *Escherichia coli*, identifying a subset of T6SS structures that were connected to the membrane at both the proximal and distal ends of the sheath/tube complex (Figure 2.5). Cryo-CLEM was integral in the identification of the T6SS in this model, providing adequate data to then model the behaviour of contraction at both ends of the needle.

Advances in the cryo-FLM portion of the workflow will allow for better correlation of the fluorescent signal with the cryo-ET data. For example, the development of cryogenic photoactivated localization microscopy (cryo-PALM) combined with cryo-ET allowed the identification of the T6SS in the bacterium, *Myxococcus xanthus* [59]. Without the cryo-PALM, the T6SS is challenging to distinguish from other tubular structures present in this bacterium. By tagging the sheath protein VipA with a photoactivatable GFP, the authors were able to locate the structure within the cell in multiple states and with increased precision. This is just one example of the potential power that CLEM can have in identifying and understanding the various molecular machines in prokaryotes.

2.6 Subtomogram averaging to gain insight into molecular machines: Chemotaxis and Flagellar Motors

As illustrated above, cryo-ET has proven to be a powerful technique. However, the tomograms are typically not sufficient to determine the structure and function of molecular machines in situ. This is due in part because the signal-to-noise ratio, a ratio between the desired signal and the background, is too low to determine the detailed composition of macromolecular complexes. If the background noise is equal to or higher than the signal noise then the target structure cannot be differentiated from the background [60]. This is the case for typical cryo-ET datasets because the data is acquired using low dose schemes to lessen the electron damage to the sample. This limitation can be partially overcome for certain cellular content that has a consistent, identical structure. In this case, we can apply a method where the identical structures are computationally extracted in so-called sub-volumes. These are then aligned to match in orientation and averaged. The resulting EM map of such an average has a substantially increased signal-to-noise ratio that allows the interpretation of structural details at higher resolution. This technique is referred to as sub-tomogram averaging (STA) [60]. STA also helps to minimize the effect of the missing wedge artefact if the particles within the individual sub-volumes have different orientations. Thus, with more particles, this artefact becomes less severe. Several dedicated specialized software packages allow STA, such for example PEET, TOM toolbox, Dynamo, EM clarity, M-software, EMAN, or Relion [28, 61]. While these all have their specific advantages, they all can extract, align and average sub-volumes that have been extracted from 3D volumes. The packages also conduct missing wedge orientation and compensation by replacing particles with information from other particles containing this specific region [28]. This additional data processing of cryo-ET data has provided some breakthrough insights into the structure and function of two macromolecular machines that enable the cells to sense their environment and actively move toward beneficial environments: the chemoreceptor arrays and flagellar motors.

Chemotaxis is a behaviour that allows the bacteria to sense their chemical surroundings and control their motility apparatus to seek out their preferred environmental niches and evade harmful ones. The bacterial chemotaxis system in the bacterium *E. coli* is arguably the best-studied signal-transduction system in biology. It relies on chemoreceptors called methyl-accepting chemotaxis proteins (MCPs), a histidine kinase CheA and the coupling protein CheW. These functional units cluster together to form extended arrays at the cell poles, which can contain thousands of chemoreceptors. In the presence of repellents or absence of attractants, CheA triggers the response messenger CheY by phosphorylation. CheY-P in turn binds to the flagellar motor and modifies the direction of flagella rotation. Additional proteins (CheR and CheB) modulate the response, enabling the cells to follow chemical gradients. CheZ terminates the cycle by turning off the respond messenger protein CheY. Chemoreceptor arrays are highly cooperative, and the activation of one receptor can spread through the array.

While the individual components of this system have been well-studied in the past, the structure and function of the in vivo arrays were unknown until they were imaged

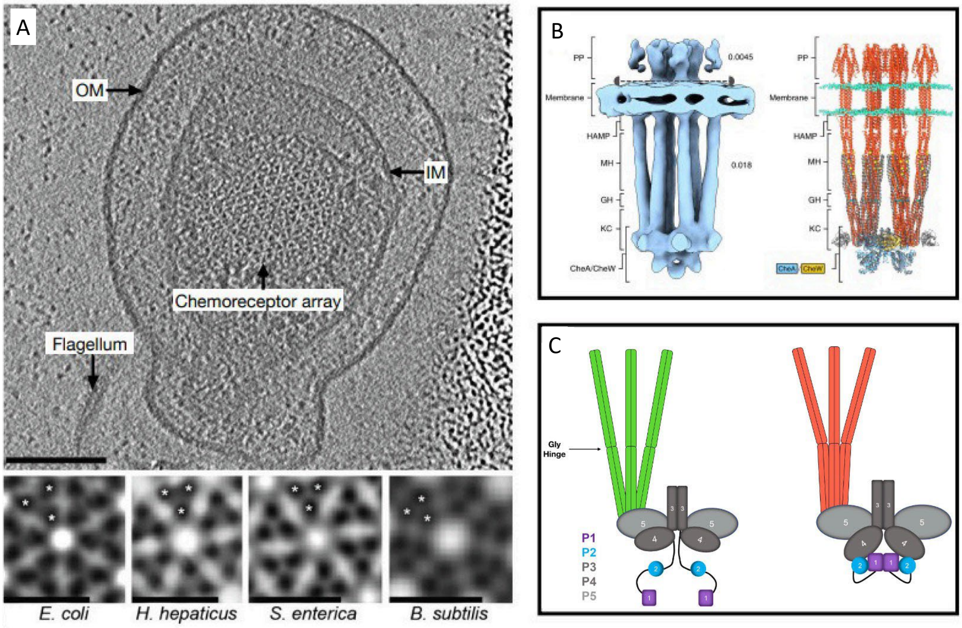

Figure 2.6: (A) Top: Top view of a chemotaxis array in a *Salmonella enterica* minicell. IM: inner membrane, OM: outer membrane. (A) Bottom: Subtomogram averages of chemoreceptor arrays in diverse species, highlighting the universal receptor arrangement. Reproduced with permission from Briegel *et al.* (2012) [62]. (B) Left: STA of the functional unit. PP: periplasmic ligand-binding domains, MH: methylation-helix bundles, GH: flexible regions containing the glycine hinge, KC: kinase control region. Right: Molecular model. Red: receptors, blue: CheA, gold: CheW. Reproduced with permission from Burt *et al.* (2020) [64]. (C) Schematic representation of the structural changes between the kinase-off (left) and kinase-on states (right). Courtesy of Dr. Alise Muok [65].

by cryo-ET. Insights into the more detailed architecture of the arrays and the changes following activation could only be gained using STA. STA revealed the architecture of these arrays, where the hexagonal receptor arrays are networked by rings of alternating CheA and CheW monomers [62, 63].

In addition, STA of in situ arrays in combination with molecular dynamics flexible fitting (MDFF) revealed insights into the structural changes that occur during the activation of CheA. The receptor-trimers adopt a more closed conformation at their baseplate interacting tips in the inactivating state, and a more open, splayed conformation in the activating state [66]. STA further revealed changes in the structure of the kinase between the on- and off states. In the off state, the two CheA domains that contain the phosphoryl group for transfer to the response messenger, as well as the domain responsible for the docking of the CheY protein, are bound to the rest of the protein in an unproductive manner (Figure 2.6 C). Once activated, these two domains are released, allowing for CheY binding and phosphoryl transfer [67]. With ever-increasing resolution of STA, it can be expected that soon further details of the signal-transduction will be unrevealed. This will undoubtedly help to understand still open questions on how the different components of the chemotaxis system interact with each other and how they are controlled.

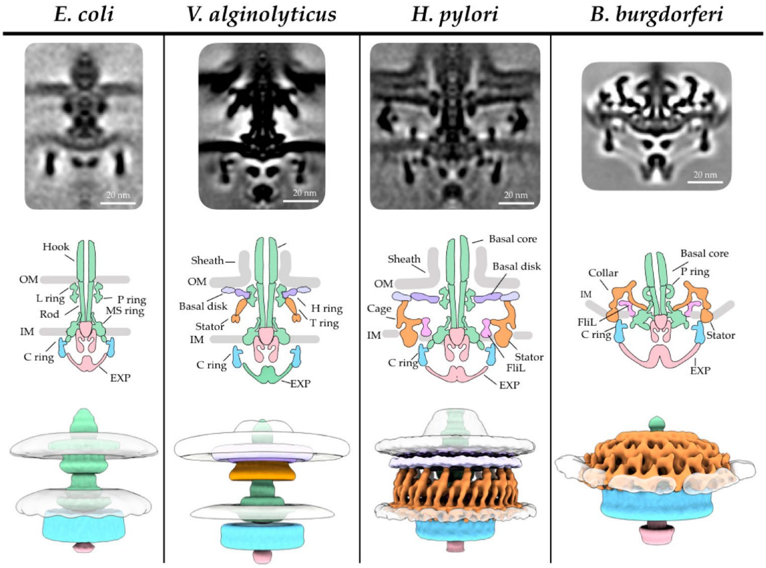

Figure 2.7: Flagellar motor, showing the conserved core elements as well as the species and genera-specific motor adaptations to fulfil their needs in their specific environment. Adapted from Carrol and Liu (2020) [68].

Another well-understood macromolecular complex is the flagella motor which powers flagellar rotation. Flagella are extracellular appendages that provide the cells with the ability to move, either by swimming through a liquid medium or by swarming on surfaces. The flagellum consists of a basal body (motor), a hook (flexible linker), and a propeller (helical filament). It is attached to the flagellar motor, which extends from the cytoplasm, through the inner membrane and the peptidoglycan layer (periplasmic space), to the outer membrane. In general, the core of the flagellar motor is structurally well conserved and shares the same mechanism among species, but the entire motor structure varies greatly (Figure 2.7). Depending on the species, the motor is either powered by a proton-motive force or by ion-motive force. In *E. coli*, depending on the orientation of the filament rotation the cell either swims/runs (counter-clockwise rotation, CCW) or tumbles (clockwise rotation, CW). The motor rotation is biased by the binding of the phosphorylated CheY from the chemotaxis system. A more detailed description of the flagellum and the flagellar motor composition can be found in the review of [68].

In the past years, STA was not just used to reveal species-specific flagellar motor compartments. It also investigated how the components interact with each other. A recently revealed example is the interaction between the messenger protein CheY with the C-ring (FliM, FliN, FliG). CheY binds to FliM and leads to a major conformational change of FliG, while FliN prevents disassociation of the C-ring compounds during the conformational change. In turn, the conformational change of FliG leads to a remodelling of the rotor-stator interaction and a switch from a CCW to a CW tumble rotation of the filament [69]. The rotor and stator complex are known to be highly dynamic and the moment of switching is rather volatile, and therefore difficult to visualize. A described solution to improve the visualization is to increase the density of the small switching proteins by GFP labelling and/or using homologs with a higher molecular mass in combination with STA [70]. In general, with increasing resolution, cryo-ET and STA will likely aid in revealing other aspects of the flagellar motor soon. For example, binding affinity vs. competition, stator assembly, and relative orientation of c-ring components are still not fully understood yet and might be answered in the coming future.

2.7 The future of cryo-ET

As we, and many others, have described, cryo-ET has evolved tremendously over the past twenty years, due in part to the work of Baumeister and his scientific heritage. Advancements in the field will continue in the years to come, significantly enhancing our knowledge of prokaryotic cell biology. Those enhancements include improved sample preparation workflows, advances in hardware and software, and the curation of the vast amount of data into publicly available resources.

Sample preparation is one of the key steps in the cryo-ET workflow. Without a properly prepared sample, no subsequent step is likely to succeed. In the past few years, significant developments in plunge freezing technologies allow the combination of grid preparation, sample application, and freezing into a single device [71, 72]. In addition, the advent of inkjet-like printing technologies and the introduction of self-blotting grids will enable the study of very volume-limited samples, which was previously impossible [73]. As noted in the large volume section, thicker samples are also becoming more and more accessible. With the application of the cryo-FIB SEM, plunge frozen samples can currently be thinned. The development of tools for larger volume samples such as multicellular tissues will greatly increase our understanding of how microbes interact with their environment.

Hardware and software developments will continue to increase the amount of data collected as well as our ability to process this data for valuable information. Hardware developments such as the laser phase plate, which provides increased contrast will minimal defocus, will likely allow a typically challenging technique to be applied to a wider range of samples with increased consistency [74]. Most importantly, the addition of this tool will aid in the analysis of smaller complexes and better interpretation of tomograms to a higher resolution. Software developments include those that enable fast tomography, a collection method that continuously records a movie as the sample is tilted with the electron beam on the sample [28, 75, 76]. Instead of the repetitive process of tilting, tracking, and imaging, these steps are essentially combined to produce one movie per target. Depending on the collection scheme, fast tomography could increase collection time per target by 50-75%, vastly multiplying the amount of data that can be collected per sample. The introduction of new processing programs such as Warp and M provides important information during data collection and a processing pipeline that connects the data collection directly to the tomogram and ultimately structural analysis [27, 77]. Software improvements are also impacting the sample preparation steps. For instance, for cryo-FIB SEM processed samples, the development of scripts has now begun to automate a typically slow and tedious process, which will lead to increased output and improved consistency [78, 79].

Once the data is collected, accessibility by the scientific community becomes important. Research groups typically focus on a single part of the data or are looking to answer specific biological questions. Yet, cellular cryo-ET collects an abundance of information about the cell and much of this information is ripe for examination. Resources such as the Caltech Electron Tomography Database have laid the groundwork for building comprehensive collections of cryo-ET data, at least at the single group level [34]. In turn, some of this information has been translated into the Atlas of Bacterial and Archaeal Cell Structure [80]. This open access, digital resource provides detailed information about the prokaryotic ultrastructure of 85 species, which can be used as a source for comparison of structures in different strains, education, and comparison of sample treatments. Initiatives like this are extremely valuable to the community and should be a goal of the cryo-EM community.

Together, this review highlights the impact and advancements of cryo-ET since its application in 1998. The technique has proved to be a valuable tool that is only now reaching its potential. We look forward to the future where cryo-ET is a standard part of the microbiology toolbox.

Credit authorship contribution statement

Janine Liedtke: Conceptualization, Writing – original draft, Writing – review & editing. Jamie S. Depelteau: Conceptualization, Writing – original draft, Writing – review & editing. Ariane Briegel: Conceptualization, Writing – original draft, Writing – review & editing, Supervision.

Declaration of Competing Interest

The author declare that they have no known competing financial interest or personal relationship that could have appeared to influence the work reported in this paper. This work was supported by the OCENW.GROOT.2019.063 and Building Blocks of Life Grant 737.016.004 grants from the Netherlands Organization for Scientific Research (NWO).

3

MORPHOLOGICAL PLASTICITY OF *CHITINOPHAGA PINENSIS* AND ITS ROLE IN PLANT-MICROBIOME INTERACTIONS

Environmental changes, whether due to climate change or human influences, compromise the resilience of plants to biotic (pathogens) and abiotic factors such as drought and heat. One promising strategy to enhance plant resilience is the use of the plant microbiota, which may be harnessed to promote plant health and growth. This approach requires the identification of key members of the microbiota and their health-promoting properties, including communication and control mechanisms. Recent studies have demonstrated that the bacterium *Chitinophaga pinensis* enhances plant health and increases resistance to fungal infection. Here, we show that *C. pinensis* exhibits an unusually high morphological plasticity, switching between a filamentous and a spherical cell state, each of which is characterized by a distinct transcriptional profile. Despite these transcriptional differences, spherical cells remained metabolically active and replicating, while lacking structural characteristics typically associated with dormant states. Furthermore, the spherical cell morphology of *C. pinensis* facilitates hitchhiking behaviour and motility via surfactin cheating, potentially influencing its dispersal and interactions within the plant microbiome. To investigate the structural dynamics and transcriptional adaptation of this plant endophyte, we applied a combination of microscopy and culture-based techniques. Taken together, our study provides new insights into the morphological flexibility and transcriptional regulation of *C. pinensis*, contributing to our understanding of the beneficial plant microbiome.

This chapter is based on **Liedtke, J.**, Rodenburg, F., Du, C., Zhang, L., van Wezel, G.P., and Briegel, A. (2025): Morphological plasticity of *Chitinophaga pinensis* and its role in plant-microbiome interactions, to be submitted.

3.1 Introduction

Modern agriculture increasingly faces challenges due to climate change and a growing world population. Therefore, new measures and innovative strategies must be developed to conserve resources and minimize losses to ensure a sustainable future.

One of these strategies is to understand and utilize the natural defence and resistance mechanisms of plants. Numerous studies have already shown that the plant microbiota plays a decisive role in this context (reviewed in [4, 8, 81]). Plants and their associated microbiota are often referred to as a holobiont, as they engage in complex symbiotic interactions and have an evolutionary history as a community (reviewed in [82]). Among the most abundant phyla within the plant microbiota, the phylum Bacteroidetes stands out as it contains numerous symbiotic strains associated with various hosts [83, 84]. These microorganisms can enhance host fitness either directly by promoting plant health or indirectly by supporting other members of the microbiota. Those that colonize plant tissue without causing harm or negatively affecting the host are known as endophytes. Recent studies have shown that the endophytic strains *Flavobacterium anhuiense* and *Chitinophaga pinensis* contribute to plant health and improve stress tolerance [85]. The diversity of the plant-associated microbiota reflects a range of strategies that can enhance plant resilience. One such strategy is the "cry-for-help" response, in which plants actively recruit beneficial microbes by releasing root exudates in response to environmental stress. The composition of these exudates varies depending on the stress conditions, which leads to a specific metabolic adaptation of the bacteria already residing in the microbiota and stimulates the production of secondary metabolites[2–4, 86]. However, effectiveness of induced stress tolerance depends on the microbiota composition, and missing key members can decrease the response effect [87]. This effect is even more pronounced during activated defence mechanisms in the presence of plant pathogens [86, 88]. In order to optimize the composition of the microbiota to protect plants naturally, it is important to identify key microbiome members and understand the factors involved in their recruitment.

As mentioned above, plants excrete root exudates to actively recruit and shape their microbiota according to their needs [3]. These exudates contain diverse compounds, including sugars, amino acids, enzymes, fatty acids and polyphenols such as flavonoids [89]. To successfully colonize the rhizo- and endosphere, microbes must be able to detect and respond to those signals. Many motile bacteria achieve this through chemotaxis, allowing them to sense and move along chemical gradients via chemosensory pathways that regulate flagellar motors [90, 91]. Depending on their structural adaptations, bacteria utilize different motility strategies, including flagella-driven swimming and swarming or gliding motility, which relies on surface adhesins [92, 93]. However, some bacteria do not possess chemotaxis arrays or motility mechanisms. This raises the question of how these strains reach the plant and establish themselves within the microbiome. Previous research demonstrated that non-motile spores of endophytic *Streptomyces* can be transported by motile bacteria, a process known as hitchhiking [94]. Hitchhiking allows non-motile bacteria to benefit from chemotactic movements without expending their own energy, potentially providing ecological advantages in host colonization. As proposed by Muok *et al.* (2021) [94] and Seymour (2024) [95], hitchhiking can also yield in long-term benefits for bacterial communities, facilitating movements through barriers and promoting metabolic exchange.

Here, we focus on *Chitinophaga pinensis*, which was recently identified as an important member of the plant microbiota particularly regarding pathogen resistance and stress tolerance [85]. Originally isolated from pine litter, *C. pinensis* is a Gram-negative bacterium found in the endosphere of various plants, including crops [85]. It is known for its ability to degrade complex polysaccharides such as chitin and produce a variety of biologically active molecules, highlighting its potential value for agriculture and industrial applications [96]. Furthermore, previous studies have reported that *C. pinensis* forms so-called myxospores or microcysts, which have been hypothesized to represent a resting stage similar to bacterial spores [97–99]. However, these structures have primarily been characterized based on their spherical morphology under the light microscope, and their metabolic state remained unclear. While most research on *C. pinensis* focused on its metabolic capabilities alone, in this study we investigated the ultrastructural morphology of cells as well as their interactions within the holobiont using a combination of microbiological assays, cryo-electron microscopy and transcriptomics. In particular, we aimed to gain insight into whether the morphology of *C. pinensis* depends on the growth conditions, and see how this correlates to the strain´s ability to interact with plant tissue. Additionally, we aimed to determine whether these interactions are solely based on chemical signals or if physical structures, such as outer membrane vesicles [100], play a role in the communication with the plant. Notably, the *C. pinensis* strain studied by Carrión (2019) [85] is neither motile nor equipped with chemotaxis arrays, which raises questions about its recruitment and ecological role within the holobiont. Finally, we investigated how these characteristics of *C. pinensis* contribute to its ecological function and potential impact on the dynamics of the plant microbiome.

3.2 Material & Methods

3.2.1 Strains and culturing conditions

C. pinensis 94 was obtained from culture collection of Carrion lab [85] and grown overnight from a 40% glycerol stock in 0.1x TSB at 25 °C and with agitation (250 rpm). After 16 h of growth, 100 µl of overnight culture was diluted into 50 ml 0.1x TSB and grown for an additional 20 h under the same conditions for obtaining long filamentous cells, and 40 h for small spherical cells (< 1 µm). Cells were harvested by centrifugation (30 min; 8000g; 4 °C). Subsequently, cell morphology was checked by light-microscopy (Axion Imager M2; Zeiss) before proceeding with any experiments. All *Bacillus subtilis* strains used in this study (undomesticated *Bacillus subtilis* (NCIB3610); *B. subtilis* DK605 (Δ*mind :TnYLB*); DS1677 (Δ*hag*); DS222 (Δ*motAB*); DK1484 (Δ*espH srfAA :mls*)) were cultivated as described before [94]. *B. subtilis* mini-cell strain (DK605; Δ*mind :TnYLB*) was grown and harvested as previously described [94].

Prior to the experiments, the cell morphology of the cultures was assessed microscopically; in the following, the 20 and 40 h growth cultures are referred to as filamentous cells and spherical cells, unless otherwise stated. The experiments described below were carried out in triplicates (N = 3) unless otherwise stated.

3.2.2 QUORUM SENSING ASSAY

Cells of *C. pinensis* after 20 h (OD_{600} = 0.2) and 40 h (OD_{600} = 0.5) growth in 0.1x TSB (25 °C; 250 rpm) were harvested by centrifugation (8000x g; 30 min; 4 °C). Each sample was adjusted to an OD_{600} of 0.2 and 0.5 with fresh medium (0.1x TSB) and aliquoted with 1 ml. All sample aliquots were then centrifuged (8000x g; 30 min; 4 °C), the supernatant discarded, and the cell pellets used for the next step.

Preparation of media and culture supernatant for the identification of quorum-sensing signalling molecules. The supernatant of a 20 and 40 h *C. pinensis* culture was extracted by centrifugation (8000x g; 30 min; 4 °C) and filtration (0.2 µm). These media are referred to below as 'long-filamentous cell media' (LM) and 'small spherical cell media' (SM). Fresh TSB were diluted 1:10 with 40 h media and are referred to as 'SM+T' in the following. In addition, phosphate-buffered saline (PBS; pH 7) and fresh 0.1x TSB medium (FM) were used as reference media for the experiments. The experimental setup is illustrated in figure 3.5. Aliquots of each sample were resuspended in 1 ml of the respective prepared medium and transferred to 96-well plates (MegaBlock®; 2.2 ml; Sarstedt), which were subsequently incubated at 25 °C and 250 rpm. After 3 and 6 h, samples were taken from all wells, treated with Syto9 (1 µM) and fixed with 4% paraformaldehyde. All samples were imaged with an upright fluorescence microscope (Zeiss Axio Imager M2 with AxioCam MRc 5), and the cell length data was determined with ImageJ [101] using the AutoTreshold function. The resulting data were visualized graphically and *p*-values were obtained from a mixed effects regression model, using the logarithm of the cell length to obtain approximate conditional normality and accounting for dependency by including a random effect for "replicate". Mixed models were fit using the lme4 package, and *p*-values were obtained using the lmerTest and emmeans packages lme4 [102], lmerTest [103], emmeans [104].

3.2.3 MOTILITY ASSAY

HITCHHIKING MOTILITY ASSAY

The motility test was performed on 0.1x TSB agar plates (ø 9 cm) with 0.5% agar for swarming plates and 0.27 – 0.3% agar for swimming plate assays. First, a new culture of *B. subtilis* and its mutants was prepared from an overnight LB culture and incubated in LB (37 °C; 200 rpm) until an OD_{600} of 0.5 was reached. Subsequently, *C. pinensis* cells were harvested from plate (0.1x TSA; 25 °C; > 1-week incubation) using a sterile loop and resuspended in 200 µl 0.1x TSB. To determine the hitchhiking behaviour, 3 µl of *B. subtilis* cells were transferred to the plate and 3 µl of *C. pinensis* cell suspension was pipetted directly onto the desired inoculation site (either directly on the *B. subtilis* inoculation site or onto a separate site on the plate). For the hitchhiking assay on swimming plates (0.27–0.3% agar; LP0011; Oxoid), a sterile loop was punctured into each inoculation site after inoculation to promote swimming behaviour inside the agar. The plates were incubated at 25 °C for up to 5 days and imaged on a light box. Experiments were performed in triplicate using Bacto^{TM} Agar (BD) and Agar No. 1 (LP0011; Oxoid). For comparison and control purposes, each condition was also tested on each strain individually.

SURFACTIN CHEATING ASSAY

Surfactin cheating assays were performed on 0.1x TSA (0.5% agar) with surfactin from *B. subtilis* (Sigma-Aldrich; St. Luis; Missouri; USA). For the incorporation of surfactant into the medium, 10 ml medium was liquefied by heating in a microwave and 10 µl surfactin (stock: 10 g/L) added after cooling down to room temperature. For the cheating assay in combination with additional potassium, 70 µl of K2HPO4 (1 M) was added to the liquid medium. The medium was then poured into a petri dish (ø 9 cm) and solidified. The topical treatment of media plates was performed by pipetting 10 µl of surfactin (10 g/L) onto the centre of the plate and left under the hood until the surfactin had completely diffused into the agar. The procedure was repeated with 1 g/L surfactin solution. All plates were inoculated with a single colony of *C. pinensis*, taken with a sterile tooth pick from a starting plate (0.1x TSA; 1.5% agar). The plates were incubated at 25 °C for 3 days and imaged on a light box. The experiments were carried out in triplicate. For comparison, media without surfactin and additional potassium were inoculated and treated in the same way.

3.2.4 FLUORESCENCE MICROSCOPY

Fluorescence microscopy was performed to evaluate and confirm the successful integration of GFP into the genome of *C. pinensis.* For this purpose, a colony was sampled from a plate, suspended in 3–5 µl PBS on a glass slide, and covered with a coverslip. Microscopy and imaging were carried out using a Zeiss Axio Imager M2 equipped with an AxioCam MRc 5 camera. GFP fluorescence was imaged (Ex 488 nm; Em 510 nm) and analysed in Zeiss Zen software.

3.2.5 CRYO-ELECTRON MICROSCOPY

Cell pellet obtained from *B. subtilis* mini-cell strain (DK605; Δ*mind :TnYLB*) as described above was resuspended in 12 µl LB. *C. pinensis* spherical cell morphology were harvested with a sterile loop from a 2-week-old 0.1x TSB plate (1.5% agar) and transferred to 200 µl 0.1x TSB medium. From the *C. pinensis* cell suspension, 2 µl were added to the 12 µl *B. subtilis* mini-cells and a 10-nm colloidal gold solution treated with protein A (Cell Microscopy Core, Utrecht University, Utrecht, The Netherlands) was added in a 1/10 dilution. The mixture was gently mixed by pipetting and incubated for 30 minutes at RT. Subsequently, 3 µl of sample were applied to glow-discharged 200-mesh R2/2 copper grid (Quantifoil Micro tools), pre-blotted for 30 sec. and then blotted for 1 sec. in a chamber with 90% humidity and at 20 °C. The grids were plunge frozen in liquid ethane using an automated Leica EM GP system (Leica Microsystems) and then stored in liquid nitrogen. Imaging of the grids was performed with a 120 kV Talos L120C cryo-electron microscope (Thermo Fisher Scientific) at the Netherlands Centre for Electron Nanoscopy (NECEN).

3.2.6 CRYO-ELECTRON TOMOGRAPHY

The *C. pinensis* cells were prepared as described above and samples were taken after 20 h and 40 h incubation. The samples were then centrifuged at 3000x g for 5 min. and the cell pellet were resuspended in 20 µl. In addition, a 10-nm solution of colloidal gold treated with protein A (Cell Microscopy Core, Utrecht University, Utrecht, Netherlands) was added in a 1/10 dilution and carefully mixed by pipetting. For vitrification, 3 µl of sample was applied to a glow-discharged grid and plunge frozen as described above. Imaging data were acquired using a TITAN Krios microscope (TFS), equipped with a Gatan K3 Summit direct electron detector and a GATN GIF Quantum energy filter with a slit width of 20 eV. Images were acquired at a nominal magnification of 26,000, which corresponds to a pixel size of

3.28 Å. Tilt series were collected using SerialEM with a bidirectional dose-symmetric tilt scheme (-60° to 60°; starting from 0°) with a 2° increment. The defocus was set between -8 and -10 µm, and the cumulative exposure per tilt series was 100 e-/A2. Alignment of the tilt series based on bead tracking and drift correction was performed with IMOD [105] and CTFplotter was used to determine and correct the contrast transfer function [106].

3.3 Results

3.3.1 *Chitinophaga pinensis* shows two distinct cell morphologies

To gain a better understanding of the general morphology of *C. pinensis* over time, we investigated the cell culture at different incubation times by light microscopy. In fresh cultures up to 20 h of growth, the cells are filamentous and can reach lengths of up to 40 µm, as described previously [97]. Intriguingly, between 20 and 40 h of growth, the morphology of *C. pinensis* dramatically transformed from several µm long filamentous cells to small spherical cells with a diameter of 600–700 nm (Fig. 3.1). When transferred to fresh media with a lower cell density, the spherical cells reverted to the filamentous cell state (Fig. 3.4). To gain a more detailed insight into these two cell morphologies, we used cryo-electron tomography (cryo-ET). Both cell types were enclosed by a typical Gram-negative cell envelope, enclosing a typical cytoplasm filled with evenly distributed ribosomes and other cellular content. Neither cell type resembled previously described spores or cysts, such as for example the presence of a thicker protective cell envelope (Fig. 3.1).

3.3.2 Resistance profiles of cell morphologies to environmental and chemical stressors

The small spherical cells observed after prolonged growth were consistent with previous reports, which described them as microcysts or spores. However, our cryo-ET results revealed that the small spherical cells forms do not have a typical spore morphology, such as a thickened cell envelope and tightly packed cytoplasm content. Therefore, we wanted to test whether the two cell morphologies exhibit distinct responses to various physical and chemical stress factors. Both cell morphologies exhibit similar resilience to the following stress factors: UV light irradiation for 10 minutes, heat stress at 60 °C and sonication for up to 5 min. each. Both cell morphologies of *C. pinensis* survived after desiccation and could be revived by plating on fresh medium. Light microscopic examination of the desiccated *C. pinensis* cells revealed small spherical cells, independent of their initial morphology. Further chemical stress tests showed slight differences in resistance behaviour of the two cell morphologies in response to changes in the pH and in the presence of up to 0.2% ethanol (Fig. 3.1). However, in the presence of 2% ethanol both cell morphologies grew slower, with the $OD_{600} \leq 0.25$. Neither cell morphology of *C. pinensis* grew in SDS-containing (0.02–2%) media.

Overall, the spherical cell morphology exhibit a higher carrying capacity and a slightly shorter doubling time compared to the filamentous cell morphology (Fig. 3.1). Nevertheless, the differences in the resistance profiles between the two cell morphologies were marginal.

Next, we investigated whether the decrease in cell size and the formation of small spherical cells represented a stress reaction. For this purpose, growth in the presence of salt (0.5–2%) or chloramphenicol (12.5–100 µg/ml) was analysed. When cells with a filamentous phenotype were exposed to higher salinity and chloramphenicol concentrations, the cell size decreased (Fig. 3.6). With increasing salt and chloramphenicol concentrations, the spherical cells tended to dominate the culture faster compared to the control conditions (Fig. 3.6). Regardless of the salt and chloramphenicol concentration in the medium, spherical cells appeared in all cultures after 2 days of incubation.

3.3.3 DEVELOPMENT OF A TRANSFORMATION PROTOCOL AND EXPRESSION OF GFP

For better visualization of the morphological switching of *C. pinensis* between filamentous to spherical growth, we expressed GFP from the chromosome. The greatest success was achieved with the construct pGSWS1802. Although the construct was successfully introduced into the genome of *C. pinensis*, it did not remain stable and faded with each new bacterial generation. Further challenges arose from the inherent resistance of *C. pinensis* to various antibiotics, including tetracycline. However, experimental tests showed that its resistance towards tetracycline is influenced by the medium and salinity (Fig. 3.7). While *C. pinensis* can tolerate up to 25 µg/ml tetracycline in TSA, this threshold drops to 12.5 µg/ml in the presence of additional salt. In specific media (M9, StrepMM and CYE), *C. pinensis* demonstrated resistance to tetracycline concentration as high as 50 µg/ml. However, at a tetracycline concentration of 100 mg/ml, *C. pinensis* was susceptible in all tested conditions.

3.3.4 TRANSCRIPTOMIC ANALYSIS OF 20 H AND 40 H CULTURES

Spherical cells were previously assumed to be dormant spores. However, the cryo-EM and resistance assays presented here revealed no structural or physiological features typically associated with dormancy. To assess the changes in transcriptional patterns between the two time points and corresponding culture types, we performed transcriptomic analysis on RNA obtained from cultures harvested after 20 h and 40 h of growth, dominated by filamentous and spherical cells, respectively. All cultures were grown under identical conditions (1.0x TSB, 25 °C, 250 rpm) (Fig. 3.4). It is important to note that the growth rate of the cultures was comparable.

Principal component analysis (PCA) showed a clear transcriptional distinction between the two time points (Fig. 3.8). Differentially expressed genes (DEGs) were defined as showing a fold change of ≥ 2 (FC ≥ 2) and an adjusted p-value (padj) of 0.05. Based on these criteria, 691 genes were upregulated and 615 downregulated in the 40-h samples compared to the 20-h samples of a total of 6094 genes (Fig. 3.9). The lists of up-, down-regulated DEGs and all DEGs were subjected to KEGG pathway enrichment analysis (Tab. 3.1). Genes downregulated at 40-h were significantly enriched for ribosomal components (cpi03010), and upregulated genes were depleted for those involved in amino acid biosynthesis (cpi01230). Additionally, genes involved in fructose and mannose metabolism (cpi00051) and fatty acid biosynthesis (cpi00061) were predominantly downregulated. Within the fatty acid biosynthesis pathway, most of the identified genes (19 out of 25) showed reduced expression, including 9 DEGs, indicating a broad transcriptional shift in this pathway.

Despite the observed downregulation of genes involved in translation and biosynthesis processes at 40-h, growth measurements under control conditions showed similar growth rates for both time points (see Supplementary). The doubling time was 1.53 h at 20-h (μ = 0.45 h^{-1}, 95% CI: 1.32 – 1.83), and 1.62 h at 40-h (μ = 0.43 h^{-1}, 95% CI: 1.39 – 1.94). The confidence intervals overlapped.

List	KEGG	Pathway	Total	List	PW total	PW DEGs	$\log_2$EF	FDR
All	cpi01100	Metabolic pathways	6094	1306	647	105	-0.40	5.56e-3
All	cpi03010	Ribosome	6094	1306	57	46	1.91	1.51e-19
Down	cpi00051	Fructose	6094	615	20	9	2.16	3.24e-3
Down	cpi00061	Fatty acid synthesis	6094	615	25	9	1.83	1.55e-2
Down	cpi03010	Ribosome	6094	615	57	46	3.00	2.38e-34
Up	cpi01100	Metabolic pathways	6094	691	647	44	-0.74	8.76e-4
Up	cpi01230	AA biosynthesis	6094	691	124	1	-3.81	5.42e-4

Table 3.1: KEGG pathway enrichment analysis of differentially expressed genes (DEGs). Columns indicate total genes in the genome (Total), DEGs per list (List), KEGG pathway size (PW total), number of DEGs in the pathway (PW DEGs), $\log_2$ enrichment factor ($\log_2$EF), and Benjamini–Hochberg FDR (FDR).

3.3.5 MORPHOLOGICAL VARIATION UNDER DIFFERENT CULTURE CONDITIONS

Next, we sought to determine the factors that trigger morphological changes. For this, we systematically varied (i) cell density (OD_{600} = 0.2 and 0.5), (ii) nutrient content, and (iii) the presence of quorum sensing (QS) signals using five different media (FM, LM, SM, SMT, B). As these factors are interrelated, they were tested by adjusting their concentrations in the media.

The general pattern was a decrease in cell length of approximately 29% for filamentous cells and an increase of about 74% for spherical cells over the measured time (Fig. 3.2).

For both morphologies, measurable changes in cell length were observed after 3 h compared to the initial values, and density-related differences became apparent. After a total of 6 h, these differences decreased, and the cell lengths showed a trend towards convergence within each cell morphology (Fig. 3.2).

The influence of cell density was more pronounced in filamentous cells than in spherical cells. In spherical cells, both densities led to a similar increase in length, differing primarily in the speed of increase. In contrast, filamentous cells showed different patterns depending on the initial density; at high density (0.5), cell length decreased continuously by approx. 32% after 6 h, while at low density of (0.2), the cell length initially decreased by 45% after 3 h, followed by an of approx. 27% after 6 h. Deviations from this general pattern were observed in B and SM media, whereby in medium B at higher cell density (0.5), filamentous cells increased in length by approximately 6% over time (Fig. 3.2B), while in SM media at lower cell density (0.2), filamentous cells continued to decrease in length after 6 h (approx. 48%) (Fig. 3.2C).

During the experiment, we assumed that the nutrient content of the media decreased in the following order, from the highest to the lowest content: SMT > FM > LM > SM > B. Whereby medium B was assumed to contain neither nutrients nor QS signals. We also presumed that LM contained QS signals from filamentous cells, while SM and SMT contained QS signals from spherical cells.

Overall, changes in cell length were observed in both cell morphologies under all conditions tested. Comprehensive details and individual diagrams for each condition are provided in the supplementary materials (Fig. 3.10).

3.3.6 *C. PINENSIS* SPHERICAL CELLS ARE DISPERSED BY *B. SUBTILIS*

Based on our observation that *C. pinensis* is non-motile under the condition tested and exhibits morphological plasticity, we next investigated whether the spherical cells could provide an adaptive advantage, particularly in terms of their potential to hitchhike on motile bacteria.

Here, we repeated the hitchhiking assay according to Muok (*et al.* 2021) [94] in order to determine the hitchhiking ability of the two cell morphologies of *C. pinensis*. For this purpose, filamentous or spherical cells of *C. pinensis* were isolated and placed on semi-solid media plate over *B. subtilis*. The hitchhiking behaviour of *C. pinensis* cells was assessed by observing their spreading indicated by the yellow-orange colonies. As shown in figure 3.2, when spherical cells were added, the yellow colonies spread across the plate. When filamentous cells of *C. pinensis* were plated, the colonies remained in the centre of the plate.

To understand the nature of the hitchhiking behaviour, we tested the ability of *C. pinensis* to hitchhike in the presence of *B. subtilis* mutants that were impeded in their movements either by inhibition of surfactin production (Δ*espH srfAA :mls*), suppression of flagellar motility (Δ*motAB*) or absence of flagella (Δ*hag*). In addition, a laboratory strain of *B. subtilis* (DK605) that had lost its swarming ability [94] was included in this study. The test revealed that the hitchhiking behaviour of *C. pinensis* is independent of flagellar movement and the presence of flagella. While the spherical cells can be dispersed by swarming and sliding motility of *B. subtilis*, they cannot be dispersed by a *B. subtilis* mutant (Δ*espH srfAA :mls*) that is limited to swimming motility and unable to produce surfactin. A surfactin cheating assay demonstrated that the spherical cells of *C. pinensis* follow surfactin dispersal in and on media surface (Fig. 3.3).

Next, we tested whether the spherical cells of *C. pinensis* follow the surfactin spreading in the presence of *B. subtilis* cells, assuming that the surfactin produced by *B. subtilis* cells is distributed over the entire plate due to their movement. Despite the presence of surfactant on the entire plate, *C. pinensis* cells only spread along the movement of *B. subtilis* (Fig. 3.3). When the spherical cells were placed between two *B. subtilis* inoculation sites, the *C. pinensis* colonies remained between them. Although the spherical cells of *C. pinensis* can cheat using *B. subtilis* surfactin, they cannot spread in the opposite direction of *B. subtilis* movement (Fig. 3.3).

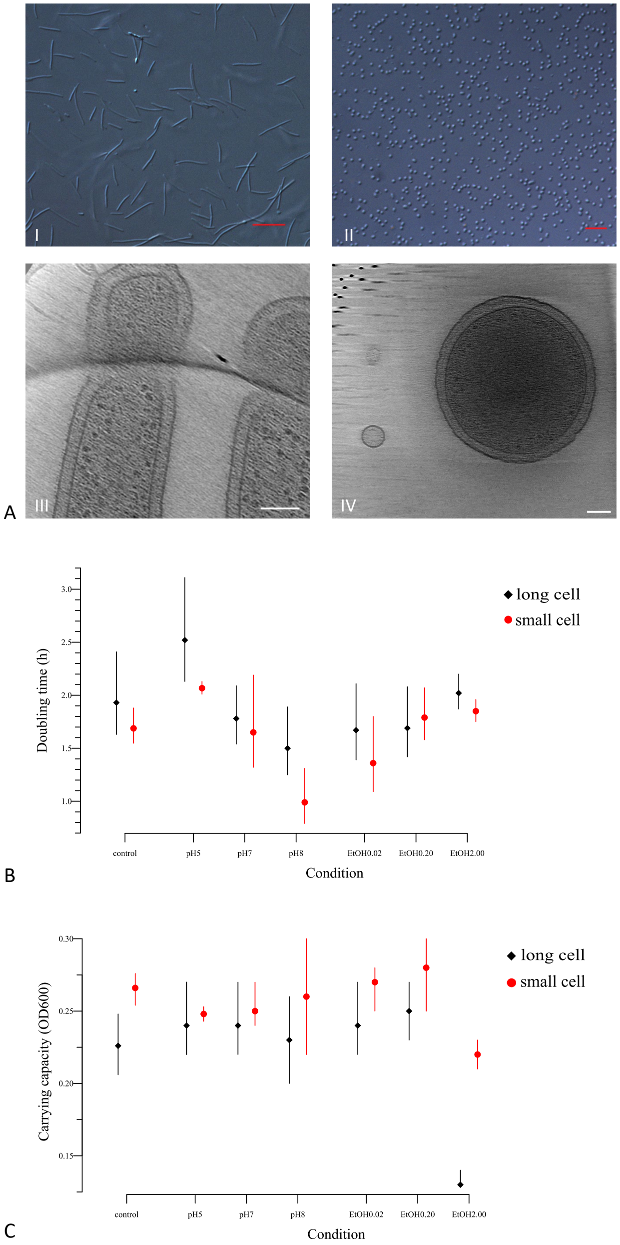

Figure 3.1: Morphological plasticity of and stress resistance behaviour of the two *C. pinensis* cell morphology. Cells were imaged by light microscopy (I – AII) and cryo-electron tomography (AIII – AIV; scale bar 100 nm). (AI) Long filamentous cells after 20 h (scale bar 10 µm) and small spherical cell shape after 40 h of incubation (scale bar 5 µm). Subsequently differences in resistance behaviour were tested in both morphologies in 0.1x TSB medium supplemented with increasing concentration of ethanol or change of media pH. Measured were the change of OD$_{600}$ over 20 h and displayed are the calculated growth parameters – doubling time (B) and carrying capacity (C) based on fitted growth curves with a confidence interval of 95%. (N= 3)

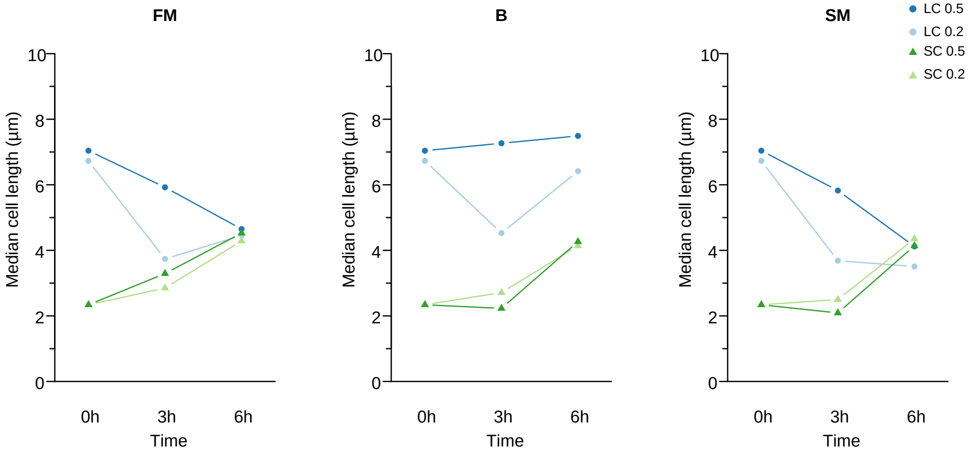

Figure 3.2: Trigger test of morphological change (N= 3). Observed pattern of change in cell morphology under different growth conditions. Shown is the determined median of cell length for each cell morphology at the cell densities of OD_{600} = 0.2 and 0.5 at the measured time points: 0, 3, and 6 h. (A) Illustration of the predominant pattern of cell length change observed in the different media, here using FM as an example. Deviating pattern were observed in the media B and SM for filamentous cells. (B) Illustration of the pattern of filamentous cells with an initial OD_{600} = 0.5 in medium B. (C) Deviating pattern of cell length change from the general pattern of filamentous cells at a cell density of OD_{600} = 0.2 in medium SM. The median cell length is given in µm.

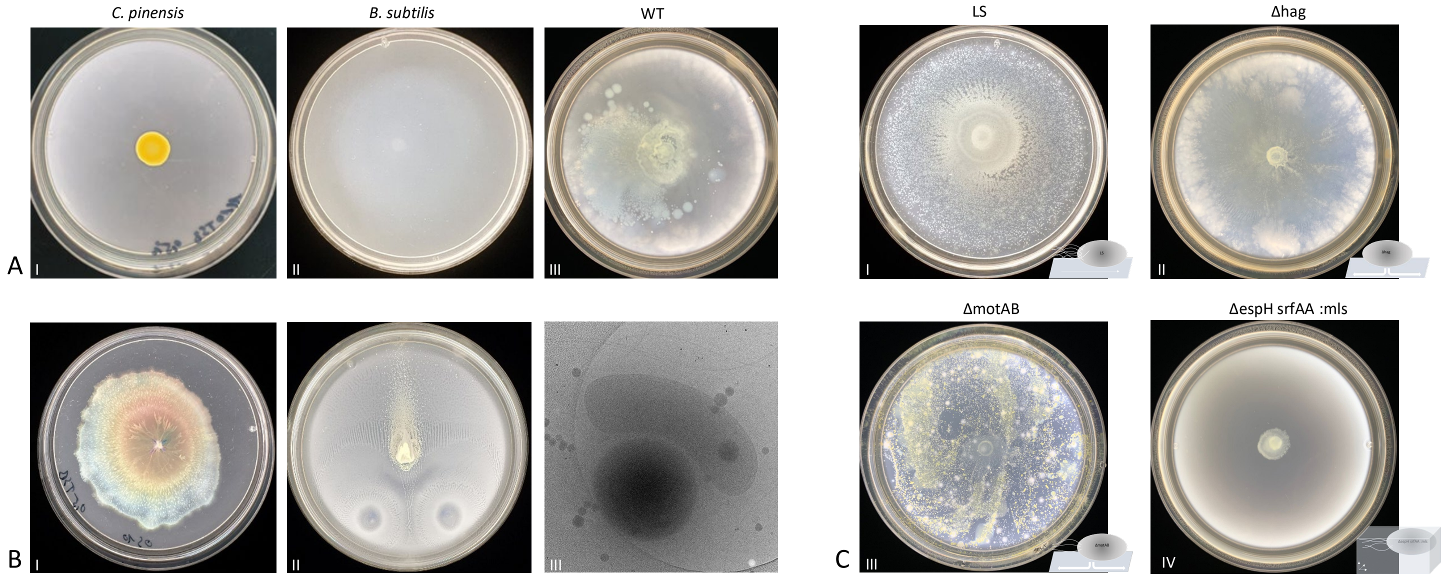

Figure 3.3: Motility assay Hitchhiking behaviour and passive translocation (N= 3), the investigated *C. pinensis* strain (AI) did not display motility under the tested conditions and remained at the point of inoculation. But when combined with a motile bacteria like a wild type (WT) *B. subtilis* (NCIB3610) (AII), a dispersal of *C. pinensis* appeared over the plate (AIII). Further hitchhiking tests were conducted with *B. subtilis* mutants, that were either hindered in their motility by either inhibition of surfactin (*espH srfAA :mls*) (CIV), suppression of flagella motility (*motAB*) (CIII) or absence of flagella (*hag*) (CII). Additionally, a lab strain (LS; DK605) that lost its swarming capability was included (CI). The test revealed flagella-independent hitchhiking behaviour of *C. pinensis*. However, this behaviour could not be observed in combination with a swimming-only strain as carrier (CIV). Subsequently the surfactin-cheating capability of *C. pinensis* was tested (BI) and this demonstrated that it follows the crowd movement of *B. subtilis* (NCIB3610) (BII). Furthermore, the hitchhiking behaviour of *C. pinensis* with *B. subtilis* (DK605) were imaged by cryo-electron microscopy (BIII).

3.4 DISCUSSION

C. PINENSIS HAS TWO MORPHOLOGIES WITH DISTINCT TRANSCRIPTIONAL PROFILES

C. pinensis is described in the literature as a long filamentous bacterium that can produce small spherical bodies, often referred to as myxospores, microcysts or spores, and assumed to represent a dormant stage [97–99]. Although these terms are frequently used, there is neither a clear definition nor a distinction between them [107]. Dormancy is defined as an adaptive state of reduced metabolic activity and arrested growth that enhances survival under unfavourable conditions [108]. It is typically associated with structural and physiological adaptations such as thickened cell walls, condensed DNA, and enhanced resistance to environmental stressors [108]. However, stress resistance assays and structural analysis suggest that morphological changes in *C. pinensis* do not follow the classical characteristics of dormancy-associated differentiation. Our transcriptomic analysis indicates a shift in gene expression patterns in spherical cells, suggesting a metabolic slow down, although cells continue to proliferate and maintain distinct transcriptional activity. Furthermore, there was no major difference in growth rate between 20 h and 40 h cultures, dominated by filamentous and spherical cells, respectively. These results suggest that *C. pinensis* does not really enter a dormant phase, but instead modulates its transcriptional profile at the molecular level as part of an adaptive response to changing nutrient availability and environmental conditions.

Morphological plasticity is a well-documented survival strategy among bacteria, enabling them to respond dynamically to environmental change. Some bacteria undergo sporulation under unfavourable condition, whereas others alter their morphological characteristics to optimize resource acquisition, evade predation, or adapt to fluctuating nutrient availability.*Escherichia coli*, for example, can undergo filamentation under stress to avoid predation or shrink size to minimize metabolic demands [109, 110]. In this context, the ability of *C. pinensis* to transition between morphologies may provide similar ecological advantages, contributing to its persistence in diverse environments. Beyond individual survival, morphological transitions can also play a role in microbial community dynamics and interactions with host organisms. Previous studies have shown that microbial morphology can influence biofilm formation, resource competition, and interspecies interactions within complex microbiomes [111–113]. However, as noted by Shah (2019) [114], the ecological consequences of morphological differentiation in bacteria remain underexplored. In the case of *C. pinensis*, the impact of its morphological states on its functional role within the plant microbiome remains unclear.

RELEVANCE OF MORPHOLOGICAL AND TRANSCRIPTIONAL PLASTICITY FOR HOST–MICROBIOTA INTERACTIONS

Previous studies on morphological plasticity have primarily focused on stress responses, often overlooking concurrent metabolic changes [113–115]. Consequently, the link between morphology and transcriptional changes beyond stress adaptation remains insufficiently explored. The observed morphological and transcriptional plasticity in *C. pinensis* challenges conventional assumptions, as filamentation is typically associated with stationary phase adaptation, where secondary metabolite production is prioritized over cell growth and occurs as a stress response [116]. In this way, bacteria ensure that secondary metabolites are produced at low cost and with high benefit [117]. However, in *C. pinensis*, filamentation and increased transcription of secondary metabolites occurs during early growth when nutrients are abundant, and cell density is low. Filamentation is energetically costly and can reduce fitness and carrying capacity [113, 117], suggesting it must provide compensatory benefits in *C. pinensis.* Filamentation has been associated with several ecological advantages, including improved surface interactions, biofilm formation, competitive polymer degradation, nutrient acquisition in heterogeneous environments, and a possible intracellular spreading mechanism [118–120]. The interplay between morphological and transcriptional plasticity in *C. pinensis* reflects a complex regulatory network within the holobiont, likely contributing to microbial stability and adaptation. However, further research is needed to determine whether these morphological transitions provide ecological advantages in competitive environments and how they influence plant-microbe interactions [116, 121].

HIDDEN TRIGGER OF RECURRENT MORPHOLOGICAL CHANGE

To identify triggers for morphological change beyond stress factors, three commonly described factors — nutrient availability, QS signalling, and cell density — were tested [112, 122]. Since these factors co-occur, they could not be tested in isolation. Instead, their concentrations were varied, and the speed of morphological change was analysed. Despite these efforts, no clear trigger could be identified, suggesting a complex interplay of growth conditions and regulatory mechanisms. Previous studies have shown that triggers are only effective under certain conditions. If these conditions are not met, the cell's regulatory mechanisms intervene and prevent the response [113]. This could explain why the filamentous cells in SMT increased in size after six hours, whereas in SM, they continued to decrease (Fig. 3.10). Both media contain QS signals from spherical cells but differed in nutrient composition. Additionally, this effect was absent in filamentous cells at higher initial cell densities, which is a further indicator for a complex interplay of regulatory mechanisms.

Triggers may also be masked by secondary effects. It was suggested that high phosphate concentrations may trigger filamentation of *Paraburkholderia elongata* [113]. However, further analysis revealed that the actual trigger was magnesium deficiency, resulting from intracellular polyphosphate chelation. Similarly, our findings suggest that morphological changes in *C. pinensis* are linked to cell density. This is supported by observations that filamentous cells exhibited density-dependent differences in cell length dynamics, while spherical cells increased in size under all tested conditions (Fig. 3.10). This may be due to dilution effects, as spherical cells were harvested from a high-density culture, potentially initiating morphological transitions.

Growth rate, rather than cell density alone, likely plays a key role in morphological changes as well [116, 120, 122]. The metabolic sensor UDP-glucose has been shown to link carbon availability to growth rate by controlling FtsZ ring assembly, a key regulator of bacterial cell division [116, 120, 122]. However, *C. pinensis* is genetically not readily tractable and despite extensive attempts we could not express FtsZ-GFP.

SPHERICAL CELLS CAN HITCHHIKE AND POTENTIALLY UTILIZE CHEMOTAXIS OF OTHERS

Although motility via the type IX secretion system (T9SS) is known in other *C. pinensis* strains [123], it could not be induced in the strain used in our experiments. This limitation led us to explore whether morphological plasticity provides alternative advantages beyond metabolic efficiency. Given their small size (600–700 nm), the spherical cells of *C. pinensis* could be transported by vascular pressure within plant tissue. However, their movement in soil remains unclear. Without chemotaxis genes, they may rely on other motile bacteria for translocation. Previous studies have shown that some non-motile bacteria exploit the motility of others for their dispersal. For example, the spores of *Streptomyces* can attach to the flagella of motile bacteria [94], while the coccoid cells of *Staphylococcus* attach directly to the cell body of swimming bacteria and can be passively translocated [124]. In our experiments, spherical cells of *C. pinensis* exhibited hitchhiking behaviour but unlike *Streptomyces* spores, this interaction was independent of carrier mobility and presence of flagella. Notably, hitchhiking was observed on swarming plates but not on swimming plates indicating that surface conditions influence this interaction (Fig. 3.3) [125, 126]. In addition, gliding, sliding, and swarming are classified as crowd movements, whereas swimming is an individual behaviour [93, 127]. Crowd movements are an energy-saving, protective and efficient translocation mechanism that optimizes the search for resources in a nutrient-heterogeneous environment such as soil [119, 126, 128].

Microscopy imaging further supports that hitchhiking in *C. pinensis* is transient rather than a stable attachment, distinguishing if from *Streptomyces* spores. As observed in figure 3.3, spherical cells loosely associated with *B. subtilis* minicells, possibly via hydrophobic interactions. Notably, some spherical cells had already started elongating and losing their spherical morphology (Fig. 3.3), but whether this promotes hitchhiking remains unclear.

In dense bacterial communities, population often align in liquid-crystal-like arrangements, promoting collective movement [129]. Consistent with this, *C. pinensis* spherical cells moved with *B. subtilis* rather than dispersing independently, despite being capable of surfactin cheating. Cheating on public goods, such as surfactin, is a well-known strategy in cooperative communities [121, 130]. However, *B. subtilis* employ regulatory mechanisms to mitigate cheater exploitation [121]. Thus, while hitchhiking behaviour was observed, it remains unclear whether *C. pinensis* actively engages in this process or undergoes passive translocation driven by *B. subtilis* crowd movements. Resolving this distinction is essential for understanding bacterial dispersal mechanisms and plant root colonization.

Each piece of knowledge contributes to unravelling and understanding the dynamic interaction within the host-microbiota. In addition, the question of the critical ratio of mobile and immobile bacteria that still allows community mobility should be answered. Considering that some bacteria are motile at low and others at high cell density, the question arises whether this contributes to the community remaining motile under different conditions. It would be also interesting to investigate the extent to which hitchhiking behaviour influences this movement, especially in the presence of plant roots. Some of these questions could potentially be explored in future studies using transparent soil and light-sheet fluorescence microscopy.

3.4.1 Conclusion

Climate change and pollution from conventional agriculture degrade resource quality and put additional stress on plants, weakening their resilience. Preserving the natural occurring plant-protective microbes in the plant microbiota can improve plant resilience and immunity. To understand the complex interactions between plants and their microbiota and within the microbiota, the key members must first be identified and then their interaction mechanism uncovered.

One such key member is *C. pinensis*, known for its plant-health-promoting characteristics, demonstrated significant morphological plasticity transitioning from a long filamentous to a small spherical cell shape, accompanied by distinct transcriptional changes. Despite this transition, the spherical cells do not exhibit dormancy-like traits such as structural differentiation, increased resistance, or arrested growth but remain reproductive. In addition, the transition into small spherical cells enables flagella-independent translocation by motile bacteria.

Further work is needed to uncover the triggering and control mechanisms of morphological and metabolic plasticity and their role in dynamic and complex interactions. In addition, it is crucial to investigate the extent to which translocation, whether by hitchhiking or crowd movement, contributes to colonization and distribution within plant tissue. Deciphering these mechanisms enables harnessing the power of microbial communities to promote plant health and foster resilient agriculture in an increasingly challenging environment.

ACKNOWLEDGEMENTS

Cryo-EM data were collected at the Netherlands Centre for Electron Nanoscopy (NeCEN) at Leiden University, with technical support from Dr. Wen Yang, Dr. Willem Noteborn, and Dr. Birgit Luef. This work benefited from access to NeCEN, which was funded in part by the Netherlands Electron Microscopy Infrastructure (NEMI), project number 184.034.014 of the National Roadmap for Large-Scale Research Infrastructure of the Dutch Research Council (NWO). J.L. was supported by the OCENW.GROOT.2019.063 and Building Blocks of Life 737.016.00 grants from the Netherlands Organization for Scientific Research (NWO), both awarded to A.B.

AUTHOR CONTRIBUTIONS

J.L. designed and conducted the study, performed most experiments, and wrote the manuscript draft. L.Z. contributed to laboratory work and provided input to the Methods section. D.U. supported the interpretation of transcriptomic data. F.R. assisted with statistical analysis and data processing. A.B. and G.P.v.W. supervised the project and provided critical feedback on the manuscript. All authors reviewed and approved the final version.

AUTHOR INFORMATION

The authors declare no competing financial interests.

3.5 SUPPLEMENTARY FIGURES

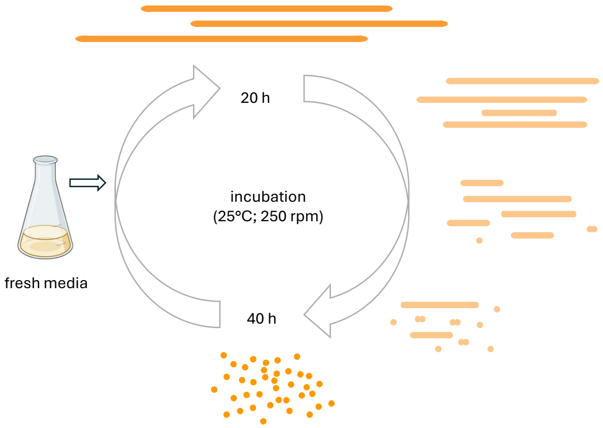

Figure 3.4: Schematic representation of the reversible morphological cycle of *C. pinensis* during growth in liquid culture (25 °C, 250 rpm). The culture transitions from predominantly spherical cells to filamentous forms within 20 h and returns to spherical morphology after 40 h. Intermediate stages are shown in lighter colour to reflect the unresolved timing of the transition. Attempts to synchronize the cell cycle and capture these intermediate forms were unsuccessful, preventing accurate determination of timing and further analysis.

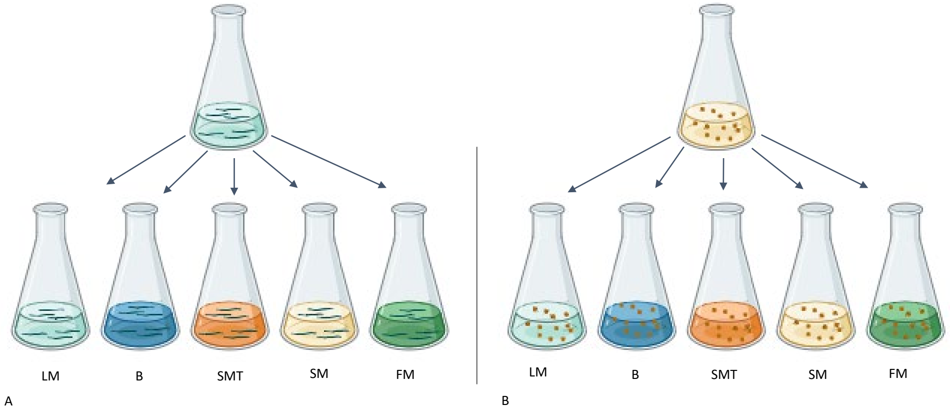

Figure 3.5: Experimental setup of the quorum sensing assay. Long filamentous cells (LC) of a *C. pinensis* culture after 20 h incubation (25 °C; 250 rpm) and small spherical cells (SC) after 40 h of incubation in 0.1x TSB were harvested. Following respective supernatant of the 20 h (LM) and the 40 h (SM) culture was sterile filtrated and used in the setup, whereby one part of the SM supernatant was supplemented with full TSB media in a 1:10 dilution (SMT). Phosphate-buffered saline (B) and fresh 0.1x TSB medium (FM) were included as reference medium. The initial cell density for both cell morphologies were setup to an OD_{600} of 0.2 and at a higher OD_{600} of 0.5. The experiment was conducted in triplicates.

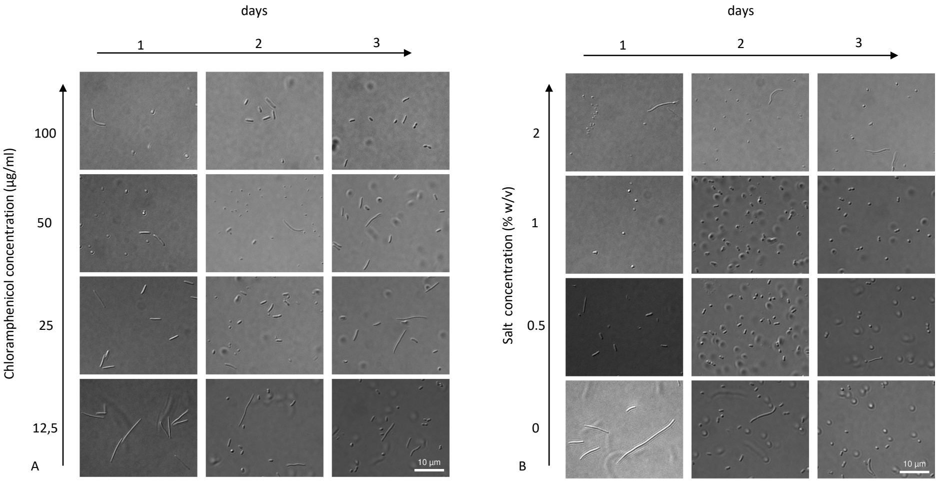

Figure 3.6: Stress reaction test of *C. pinensis* (N= 3) in 0.1x TSB with increasing chloramphenicol (µg/ml) and salt concentration (% w/v). To investigate the extent to which the formation of small spherical cells is a stress response of *C. pinensis*, cells were first harvested at the long filamentous cell stage after 20 hours of incubation and then exposed to chloramphenicol concentrations ranging from 12.5 µg/ml to 100 µg/ml (A). Chloramphenicol is an antibiotic that binds to the 50 ribosomal subunit and thus impairs protein biosynthesis. In addition, the cells were exposed to salt concentrations of 0.5% to 2% (B), which disrupt the integrity of the cell wall. A culture in 0.1x TSB without additional salt was used as a reference sample (B). Cells were imaged every 20 h for 3 days. Scale bar 10 µm.

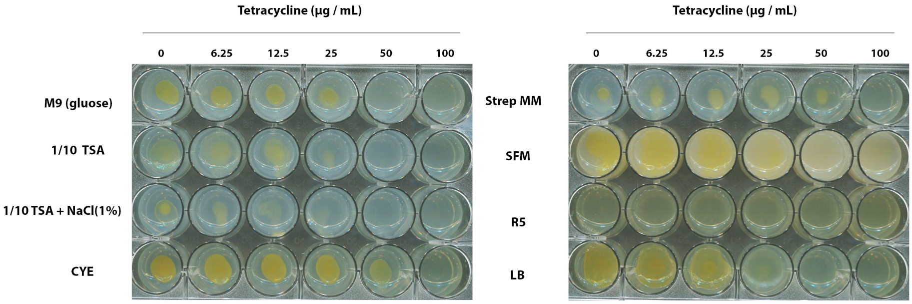

Figure 3.7: Media dependent antibiotic resistance behaviour of *C. pinensis*. Growth of *C. pinensis* colonies on different media with increasing concentration of Tetracycline (µg/ mL) and salt.

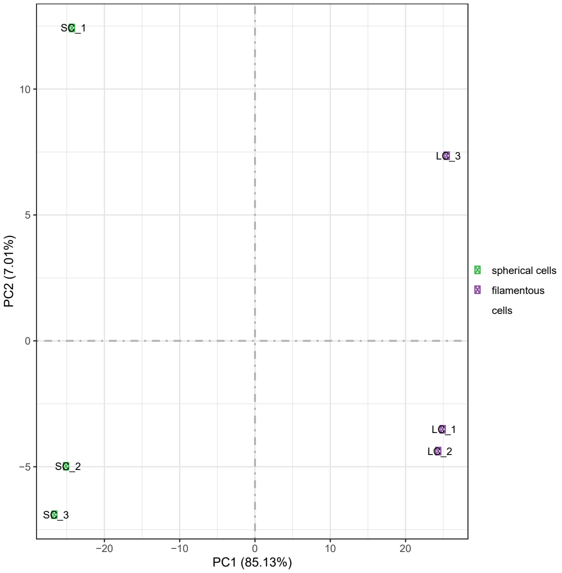

Figure 3.8: Principal component analysis (PCA) of transcriptomic profiles from *C. pinensis* cell morphologies. Samples cluster according to morphology, with PC1 explaining 85.13% of variance, separating spherical cell (SC) from filamentous cells (LC), indicating distinct transcriptional states.

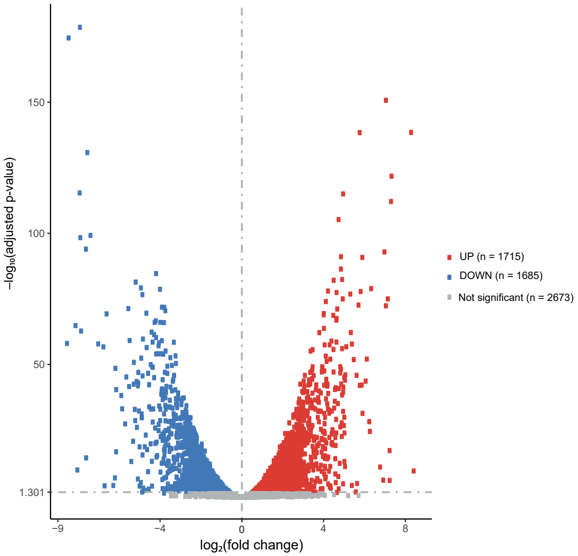

Figure 3.9: Volcano plot of differential gene expression (DEG) between spherical and filamentous *C. pinensis* cells. Genes with a fold change of 2 (FC ≥ 2) and an adjusted p-value (padj) of 0.05 are considered significantly regulated: red = upregulated (n = 1715), green = downregulated (n = 1685), blue = non-significant (n = 2673).

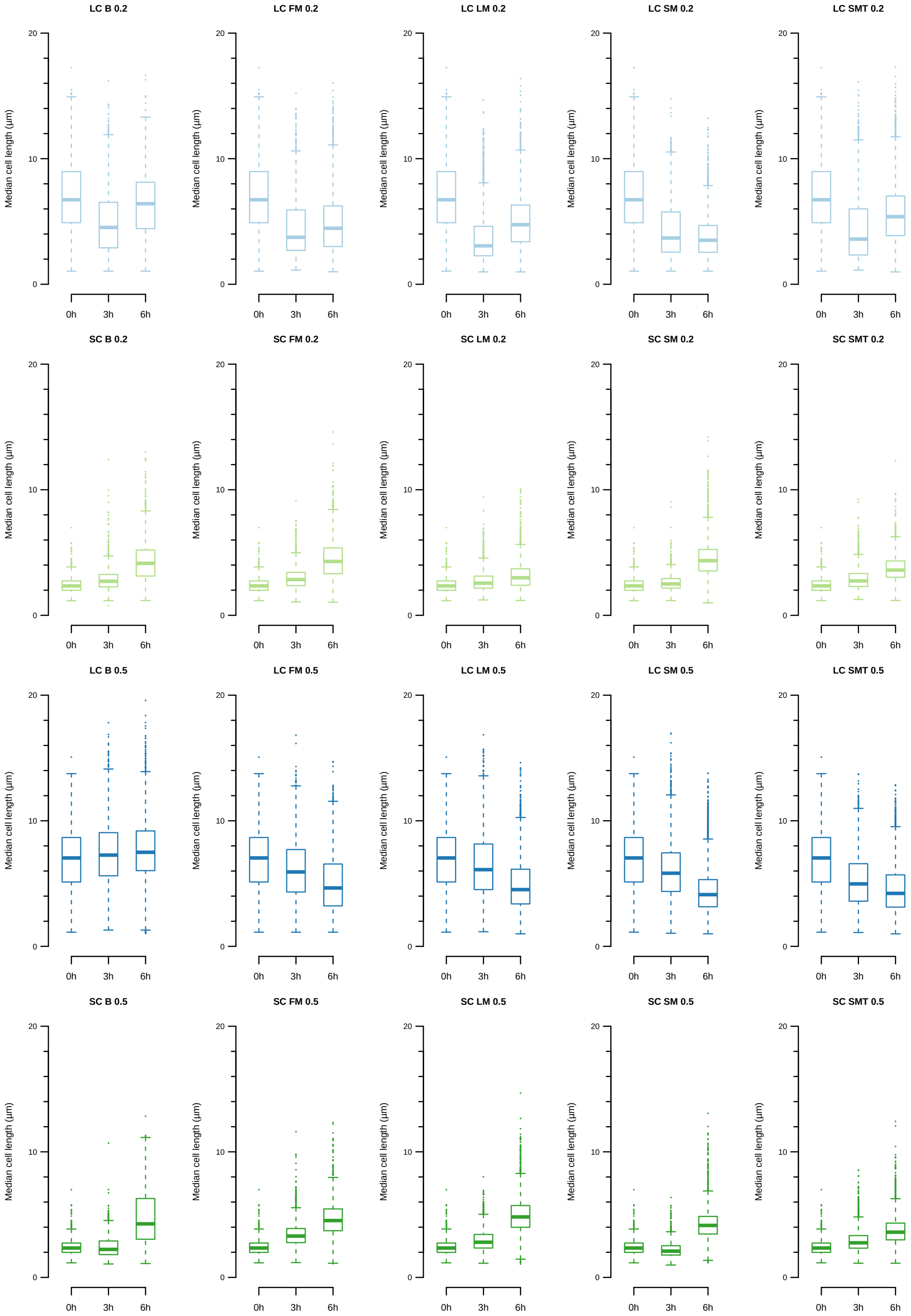

Figure 3.10: Comparison of *C. pinensis* morphological change over time under different growth conditions. (A - E; K - O) Change from an initial long filamentous cell shape (LC) with an initial cell density of OD_{600} = 0.2 (A-E) and 0.5 (K - O). (F – J; P – T) As well the transition from a small spherical cell shape (SC) with an initial cell density of OD_{600} = 0.2 (F – J) and 0.5 (P – T). Following conditions were used: buffer (B); fresh medium (FM); sterile filtrated supernatant of 20 h growth medium (LM); sterile filtrated supernatant of 40 h growth medium (SM) and sterile filtrated supernatant of 40 h growth medium supplemented with full medium (SMT). Cell lengths [µm] were measured after 3 and 6 hours after inoculation. Confidence interval 95% and N=3.

3.6 SUPPLEMENTARY METHODS

3.6.1 PHYSICAL STRESSOR ASSAY

To measure the differences in viability of the filamentous and spherical cell morphologies when exposed to physical and chemical stresses, we first harvested the cells from liquid culture (50 ml) by centrifugation for 10 min. (filamentous cells) and 30 min. (spherical cells) at 8,000x g and at 4 °C. All samples were adjusted to an OD_{600} of 0.2 and stored on ice until the various treatments outlined below. Subsequently, 5 µl of each sample was drop plated in triplicates on 0.1x TSA plates (1.5% agar) and incubated at 25 °C. The plates were imaged on a light box after 2 days.

TREATMENT WITH ULTRASONIC

For this treatment, 1 ml of each sample was transferred to a 15 ml Falcon tube and treated in an ultrasonic bath (ultrasonic cleaner; CDS-100; AC 220 240 V 50/60 HZ; 42,000 hz) for 2 or 5 min. and then placed back on ice.

HEAT TREATMENT (60 °C)

1 ml of each sample was transferred to a Falcon tube (15 ml) and placed in a 60 °C prewarmed water bath (Type: W 200; 220 V; 5.5 A; 50 Hz; 1200 W; Memmert GmbH + Co KG) for 2 or 5 min. and then placed back on ice.

TREATMENT WITH ULTRAVIOLET LIGHT (UV)

UV-light treatment of each sample was performed as described before [131] in a biosafety cabinet (BSC-700II-I; HMC Europe) with a UV-light source (ZW15S19W-Z436; Cnlight; Shelley). From each sample, 5 ml of the culture was transferred to a sterile petri dish (Ø 9 cm) and placed without a lid at a distance of 50 cm from the UV-light source. The exposure time was 5 or 10 min., and after treatment the samples were cooled at room temperature before plating.

DESICCATION TEST

Filamentous and spherical cells were plated on 0.1x TSA and incubated at 25 °C for 8 weeks until the agar had completely dried out. Subsequently, 1 ml of 0.1x TSB and a sterile loop was used to scrape the cells from dried agar plates. From the resulting cell suspension, 100 µl was used to inoculate and spread onto new 0.1x TSA media plates. The plates were incubated at 25 °C and imaged after 2 weeks.

3.6.2 CHEMICAL STRESSOR ASSAY

The experiments to test the resistance behaviour of the two cell morphologies were carried out on 96-well plates and with biological and technical triplicates. The cells were harvested as described above and the OD_{600} of each sample was set to 0.5 − 0.6. Each well was prefilled with 180 µl 0.1x TSB and 20 µl of the cell cultures were added. The measurement was performed in an automated Spark® multimode microplate reader (Tecan, Switzerland) with the following parameters: Temperature 25 °C; measuring time 22 - 24 h; amplitude 2 mm; frequency 810 rpm; duration 10 s; linear duration 5 s; wavelength 600 nm; 10 flashes; settle time 5 ms and an interval of 30 minutes. For the evaluation and quantification of the growth parameters under the different chemical growth conditions, the doubling time, growth rate and carrying capacity were computed in R (version 4.3.2) using the packages growthcurver (version: 0.3.1) and lme4 (version 1.1-35.1) and the RStudio IDE.

Pondus Hydrogenii (pH) test

The pH test was carried out with 0.1x TSB medium (pH 7.2), which was adjusted to pH 5 and pH 8 with HCl and NaOH. Untreated 0.1x TSB (pH 7.2) was used as a positive and growth control.

Sodium dodecyl sulfate (SDS)

Sterile filtrated SDS (dissolved in 0.1x TSB) was added to the medium (0.1x TSB) at a final concentration of 0.02%; 0.2%; and 2% (w/v).

Ethanol test

Ethanol was added to the medium (0.1x TSB) at a final concentration of 0.02%; 0.2%; and 2% (w/v).

3.6.3 Stress-reaction test

Cultures of *C. pinensis* (25 °C; 250 rpm; 20 h; $OD_{600} = 0.1$) were centrifuged (1500x g; 30 min; 4 °C) to obtain cell pellets, which were resuspended in the following media: Liquid media with different chloramphenicol concentrations were prepared with a chloramphenicol stock solution (25 mg/ml) and diluted with 0.1x TSB to final concentration of 100, 50, 25 and 12.5 µg/ml chloramphenicol. Media with different NaCl concentrations (0.5 – 2%) were prepared from a 10% (w/v) stock solution in 0.1x TSB. In addition, 0.1x TSB was used as the medium for the oxygen stress test. Subsequently, 1 ml of each sample was transferred to a 96-DeepWell^{TM} plate and incubated (25 °C; 250 rpm; 3 days). To prevent evaporation of the medium, the plates were sealed with a sealing film, whereby the wells of the oxygen stress test were sealed with 3 layers of sealing film. To prevent additional oxygen from entering the oxygen stress test, the sealing film was only cut open for one row of wells for each examination. Every 20 h, 10 µl was taken from each sample and the cell morphology was examined using a light microscope (Axio Imager M2; Zeiss). All tests were performed in triplicates.

3.6.4 Transcriptomics and data analysis

C. pinensis was cultured in 50 ml 0.1x TSB (25 °C; 250 rpm), and cells were harvested by centrifugation (1500x g; 15 min; 4 °C) after 20 h (filamentous cells; OD_{600}: 0.16 ± 0.01) and 40 h (spherical cells; OD_{600}: 0.9 ± 0.1) of growth. Due to the low density, the cell pellets of 3x 50 ml *C. pinensis* 20 h culture were pooled to obtain a sufficient number of cells for RNA extraction. From the 40 h *C. pinensis* culture, 10 ml were used for cell harvesting. The cell pellets were resuspended in 1 ml RNAprotect®, incubated for 5 minutes at room temperature (RT) and then washed with 0.1x TSB (centrifugation: 5000x g; 10 min; RT). Total RNA was extracted and purified using the RNeasy® Mini Kit (Qiagen; Hilden; Germany) according to the manufacturer's instructions. The removal of rRNA, library preparation, Illumina sequencing and subsequent quality control of the data were performed by Novogene Europe (Cambridge, UK). The RNA-sequence data was analysed using a standardized pipeline. The raw data was processed to remove adapter sequences and low-quality reads. The sequences were then aligned to the reference genome *C. pinensis* (accession no. LR632929 from the study [85]) annotated by Prokka using Bowtie2. Gene expression levels were quantified using FeatureCounts and differential expression analysis was performed using DESeq2 (1.20.0). Genes with an adjusted *p*-value below 0.05, as determined by DESeq2, were considered differentially expressed. Gene Ontology and KEGG pathway enrichment analyses were performed with clusterProfiler (v3.8.1).

3.6.5 Expression of green fluorescent protein (GFP)

Native gap promoter was amplified from genomic DNA of *C. pinensis* using primer pair Pgap_chi_F (5'-AGGGAATTCCGGACCGGTACCCCACAGGTCGCCCATAAATAA-3') and Pgap_chi_R (5'-TTCTTCTCCTTTACTCATTTTACACTGTAGTTTGTAGATGAAAAATTGAG-3'), gene gfpmut3 was amplified from synthesized DNA fragment harbouring gfpmut3 [132] using primers gfpmut3_F (5'-ACAGTGTAAAATGAGTAAAGGAGAAGAACTTTTCACT-3') and Chitin_GFP_R (5'-TGCATGCCTGCAGGTCGACTCTAGATATTTGTCCTACTCAGGAGAGCGTTC-3'), the aforementioned PCR products were purified and cloned into KpnI and XbaI digested pCP23 [133] via Gibson assembly. The generated construct pGWS1802, which expressing GFPmut3 under the control of gap promoter, was further introduced into *C. pinensis* by electroporation as described previously [132]. The successful introduction of pGWS1802 was validated by colony PCR on transformants which were able to grow on CYE agar containing tetracycline (100 μg/mL), using primers pair gfpmut3_F and Chitin_GFP_R. However, subsequent experiment showed the plasmid pGWS1802 could not be maintained in the cells likely due to a replication issue which requires further investigation.

4

Optimizing cryo-EM Sample Preparation for High-Resolution Imaging of the Ultrastructure of AMF Hyphae

Arbuscular mycorrhizal fungi (AMF) form symbiotic relationships with the majority of vascular plants, acting as mediator in a cross-species trading network of nutrients and resources. Despite their ecological and agricultural importance, key questions remain regarding how AMF regulate the speed and direction of transport within their hyphal networks. In this study, we employed advanced cryo-electron microscopy (cryo-EM) and optimized vitrification techniques to investigate the ultrastructure of AMF hyphae and spores. By improving sample preparation procedures, including the use of newly designed snap-button planchettes, we preserved mature hyphae in a near-native state for high-resolution imaging. This approach revealed consistent cell wall morphology, extensive lipid vesicles with interconnected structures, and clustered organelles along the mature hyphae. These findings provide insight into the cellular organization of AMF and lay a foundation for understanding the structural basis of their trading networks. The methodologies demonstrated here also pave the way for further exploration of AMF-host plant interactions, advancing their potential applications in sustainable agriculture and ecosystem management.

This chapter is based on a manuscript by **Liedtke, J.**, Moravcová, J., Křepelka, P., van Son, M., Nováček, J., Kokkoris, V., Shimizu, T. S., Kiers, T., and Briegel, A.: Optimizing cryoEM sample preparation for high-resolution imaging of the ultrastructure of AMF hyphae, in preparation.

4.1 INTRODUCTION

Arbuscular mycorrhizal fungi (AMF) are an ancient group of obligate biotrophic plant symbionts that have been associated with plants for more than 450 million years [13]. AMF are considered key microbionts in the rhizosphere, as they form symbiotic relationships with more than 72% of vascular plant species and even connect various plant species through an extensive hyphal network [134, 135]. This fungal network acts like a biological trading system in which resources and services are exchanged [135]. The fungal partner supplies mineral nutrients, especially phosphorus and nitrogen, and in return receives up to 20% of the plant's photosynthetic products, which is primarily carbon [136].

This mutualistic system enables plants to overcome spatial limitations in nutrient acquisition, and to gain access to resources that would otherwise be too distant to reach. In addition, the fungal network acts as a safety system through which warning signals can be transmitted, allowing plants to respond adaptively to both, biotic and abiotic, stress factors. Furthermore, the hyphal network alters the chemical and physical environment of the surrounding soil through exudates and attracts a diverse community of beneficial microorganisms which, together with the fungal network, form the hyphosphere [136]. These microbial associations enhance the nutrient uptake of the AMF and offer additional protection against competitors and pathogens by forming a biofilm along the hyphal surface. Thus, AMF play a multifaceted role in plant health and ecosystem dynamics that goes beyond nutrient exchange, supporting plant resilience and defence [137].

This complex symbiosis begins when a germinating AMF spore develops an exploratory hypha that branches in response to plant signals, such as root exudates like strigolactones. These signals enable the hypha to move toward the plant by following a gradient of signals in the soil. Upon reaching the root surface, the hypha forms a hyphopodium and awaits the plant's signal to enter its tissue. In response, the plant initiates a process that guides the hypha through its tissue with a penetration apparatus - a membrane that acts as a transcellular tunnel surrounding the penetrating hypha. Once inside, the intercellular hypha spreads along the root axis toward the inner cortical cells. Here, it grows intracellularly and branches into arbuscules. These arbuscules serve as a symbiotic interface for nutrient exchange, with the actual exchange occurring in the perifungal space between the fungal and the periarbuscular membrane.

The arbuscules are temporary structures that can be actively degraded by the plant if nutrient exchange proves insufficient. Additionally, one plant can host multiple AMF strains, including competing strains, simultaneously, allowing it to select the most efficient trading partners. In turn, the AMF can control its cytosolic flux, thus influencing the exchange process, as well. Furthermore, the AMF extends its extracellular hyphal network to seek out other potential trading partners and resources. As part of its life cycle, the AMF also forms new spores, each with strain-specific morphological characteristics. These spores not only facilitate the spread of the fungus to new environments but also provide a basis for AMF taxonomy [138].

The fascinating aspect of this complex symbiosis is how AMF regulate and control resource exchange. In particular, how they transport, divide, and redistribute various goods. Previous studies have attempted to address this question using various microscopic techniques and also in combination with different labelling methods. However, the focus has often been on the localization and organization of arbuscules in plant tissue, with an emphasis on the arbuscule interface [139, 140]. Only a limited number of studies have investigated the structural composition of the AMF hyphal network and the arrangement of cell organelles within hyphae. Nevertheless, research to date has provided valuable insight into the basic structure of hyphae, demonstrating that AMF contain numerous amounts of mitochondria and multiple nuclei that can be genetically distinct (heterokaryosis). The lumen of aseptate hyphae is largely occupied by elongated vesicles, which often contain lipids. Vesicles of unknown content with varying electron densities were also observed, hypothesized to contain condensed minerals, such as polyphosphates [141]. Other organelles commonly found in fungal cells, such as the endoplasmic reticulum, ribosomes, Golgi apparatus, and microtubules, have also been described in the literature [141]. Observations of cell wall morphology and the plasma membrane indicate a multi-layered structure, similar to that of spore cell walls, although the cell wall morphology of hyphae and spores is clearly different [142, 143]. Furthermore, bacterial and virus-like structures have also been observed within the hyphae [141, 144]. Despite extensive investigation, the structural level at which long-distance transport of goods is regulated remains unclear, and no cellular structure corresponding to a control mechanism has been identified.

As mentioned in previous studies, nearly all microscopic techniques and labelling methods used so far require intensive sample preparation steps. These steps, in one way or another, affect the achievable structural resolution and can compromise sample integrity, obscure finer structural details, and lead to artefacts and misleading assumptions [145]. In order to maintain sample integrity during the sample preparation workflow, a High-pressure freezer (HPF) was used – a procedure in which the sample is rapidly immersed in liquid nitrogen under pressure, preventing formation of crystalline ice and instead preserving the sample in its natural near-native state in vitrified ice [139, 141, 146]. This preservation procedure has been successfully applied to various sample types and has been proven to maintain the sample structure in a near-native state [147]. However, the samples were subsequently treated with freeze-substitution, in which the ice is replaced by a mixture of chemical fixatives, still carrying the disadvantages of chemical fixation [140, 141]. In this study, we are aiming for the development of a sample preparation procedure that preserves the near-native state of the sample throughout the entire sample preparation procedure leading to imaging of the AMF hyphae at high resolution by cryo-electron tomography (cryo-ET). The improvement of sample preparation and the use of cryo-EM will provide further insights into the structural organization of the hyphae, allowing for a more detailed examination of cellular organelles and the cytoskeleton, and potentially reveal a control mechanism for long-distance transport of nutrients.

4.2 Material & Methods

4.2.1 Sample and sample preparation

Rhizophagus irregularis (C2) infected (Ri) T-DNA transformed root organs of *Daucus carota* and *Lycopersicon esculentum* grown on standard MSR medium were provided by the group of Kokkoris & Kiers (Vrije Universiteit Amsterdam/ Netherlands) who received the root organs from Goh [148]. Each plate was divided into two compartments: one with the infected root organ and the other with the fungal compartment covered with cellophane which was placed on top of the agar. The infected root organ plates were incubated at 25 °C in the dark until use.

In preparation for the vitrification procedure, different approaches were used to harvest the hyphae network and spores from the fungal compartment of the plate. The first approach involved transferring the agar from the hyphal compartment of the plate into a 50 ml falcon tube and liquefying the agar with 10 ml sodium citrate solution (10 mM; pH 6) and vigorous shaking to release the network from the agar [149]. The second, gentler approach involved using the hyphal network that had grown on the cellophane surface layer above the agar. The network was washed off the cellophane with PBS buffer, allowing for a quick transfer to either an electron microscopy (EM) grid or a 3 mm planchette for the subsequent vitrification procedure.

In the later stages of the experiment, germinated spores were used to allow imaging of intact hyphae. First, the spores were separated from the surrounding network by vigorous shaking in 10 mM sodium citrate buffer (pH 6). The remaining network residues were manually removed under a binocular microscope using fine tweezers. To ensure only viable spores were used, dead spores were identified by their distinct colour change after treatment and removed. The viable spores were then placed individually and at a distance on the cellophane surface of an MSR plate (⌀9 cm) and incubated in the dark at 28 °C until germination. For collection, germinated spores were carefully detached from the cellophane surface with a small amount of PBS. Each germinated spore, along with its hyphae, was carefully collected with a 100 µl pipette tip and a small amount of PBS, keeping the sample near the tip opening to prevent adherence to the plastic interior of the pipette tip. The spores were then pooled in a larger drop of PBS on a petri dish. Once all germinated spores and their hyphae were collected, they were transferred to the planchette for high-pressure freezing (HPF) using the pipette tip.

4.2.2 FLUORESCENCE STAINING OF AMF HYPHAE NETWORK AND SPORES

Fluorescent staining was used to localize the hyphal network after HPF and to assess the integrity of the hyphae, distinguishing between intact hyphae with cellular compartments and those that had been damaged during the sample preparation procedure. A combination of fluorescence dyes, mainly Nile Red (NR) and Calcofluor White (CFW) (BactiDrop^{TM}, Remel^{TM}, Thermo Scientific ^{TM}), was used to distinguish and recognize intracellular lipid droplets (NR) and chitin-polysaccharides (CFW). A NR stock solution (10 mg/ml in DMSO; Nile blue A oxazone, Sigma-Aldrich) was diluted 1:100, and 100 µl of this solution pipetted onto the cellophane surface of the fungal compartment of the plate (diameter 9 cm). After 60 min incubation at room temperature (RT) in the dark, excess dye were removed, and 100 µl of 1:46 diluted CFW solution was added. Following an additional 30 min incubation, the plate was washed again with PBS.

In subsequent experiments, additional staining agents such as DAPI (5 µg/ml in PBS; Roche Diagnostics GmBH; Mannheim, DE) and MitoTracker^{TM} Green (1 mM in DMSO; Invitrogen, Oregon, USA) were included in the staining protocol. The DAPI stock solution was diluted 1:5 in a 50% glycerol solution (diluted with MQ), and 200 µl applied on the cellophane surface of the fungal compartment. After an incubation of 15 min in the dark, the excess dye was removed and the plate washed with PBS. Subsequently, 200 µl of

MitoTracker diluted 1:1000 in PBS was added to the fungal compartment of the plate and incubated in the dark for one hour. Subsequently, the excess staining was removed, and the plate washed twice with PBS.

The cellophane with the hyphal network was then transferred to a new petri dish, where the hyphal network was washed off with PBS for further use in the vitrification procedure. The fluorescence staining of the hyphal network was assessed using a fluorescence microscope (DMi8 M; Leica Microsystems GmbH, Austria) prior to freezing.

4.2.3 VITRIFICATION PROCEDURE

Vitrification was performed by HPF with a Leica EM ICE (Leica Microsystems GmbH, Austria). The samples were high-pressure frozen either on grids by using a modified waffle method [150] or directly in 3 mm planchettes (Leica Microsystems GmbH, Austria) [151].

AMF WAFFLED GRID PREPARATION

For the AMF waffle grid preparation, two approaches were used. The first approach followed the waffle method procedure where the flat side of 3 mm B-planchettes was polished according to the protocol [150]. Additionally, the planchettes were cleaned and coated three times with soy lecithin (1 mM in chloroform). Prior to coating, both sides of the B-planchettes were glow discharged using the H-O UltrAuFoil program (hydrogen 6.4 sccm; oxygen 27.5 sccm; duration 2 min; 40 W; range 5 W) in a plasma cleaner (Solarus II, model 955, Gatan). The grids were also glow-discharged under the same conditions. During the procedure, different grids were tested to improve sample attachment to the grids. The following grid types were used from Quantifoil (Großlöbichau; DE): R2/1-Cu-200; R2/4-Au-200; R1.2/1.3-Au-300 and from Electron microscopy Science (PA; USA): CF100H-Au-50. Later in the experiment, we also tested whether an additional gold layer of 20 nm on the grid would improve sample attachment and recovery after HPF. After preparing the planchettes and grids the waffle sandwich was assembled according to the waffle protocol. The AMF sample was applied to the grid with n-hexadecene before closing the assembly with the flat side the B-planchette. Immediately after, the assembly was HPF and disassembled in liquid nitrogen (LN_2). For further processing, the AMF waffle grid was then clipped into an autogrid.

The second approach for AMF waffle grid preparation were performed using customized snap-button planchettes (unpublished), designed and provided by J. Nováček (CEITEC; Brno; CZ). As in the previous approach, the planchettes were plasma-cleaned and coated three times with soy lecithin on the surface that would face each other during assembly. Additionally, the autogrid rings were also plasma-cleaned and dipped three times in the soy lecithin solution, then air-dried while held with tweezers to prevent damage to the coating from contact with surfaces. Prior to the assembly of the snap-button waffle, plasma-cleaned grids were clipped into the treated autogrid rings. The assembly proceeded as following: first, the stud planchette was placed in a planchette holder resting on tissue, and the clipped grid was positioned on the stud´s dome. The grid was than moistened with a drop of PBS, and AMF samples were applied. Next, the socket planchette was filled with PBS and placed on top of the assembly, allowing excess liquid to be absorbed by the tissue underneath. The assembly was then immediately high-pressure frozen. Following this procedure, the assembly was recovered and disassembled in LN_2. If necessary, the autogrid was detached from the stud planchette by gently using the tip of an injection needle (⌀0.3 - 0.45 mm, length 13 - 23 mm) to lift it off. The recovered autogrids were stored in autogrid boxes in LN_2 until further use.

AMF planchette preparation

The preparation of AMF planchettes was primarily optimized for AMF spores, which can reach a diameter of up to 150 μm. Prior high-pressure freezing, both A- and B-type planchettes were plasma-cleaned on both side under the same conditions described above. The flat side of each B-planchette was then coated three times with 3 μl of soy lecithin (1 mM in chloroform) per application. To ease differentiation in subsequent procedures, A-planchette side with depths of 100 μm and 200 μm were color-marked. For consistency, only one specific side of each A-planchette was marked and used per session, which comprised up to nine samples.

To apply the samples, the A-planchettes were fist filled with PBS, and the AMF spores were added. The assembly was completed by placing the flat side of a B-planchette on top. Excess liquid was carefully removed by briefly placing the assembly on tissue. The assembled planchettes were immediately after high pressure frozen. Subsequently, the assemblies were recovered and disassembled in LN_2. The color-marked side of each A-planchette was used to identify the side containing the sample. The samples were stored in autogrid boxes in LN_2 until further use.

The AMF planchette preparation were mainly used for the AMF spores, which can be up to 150 μm in diameter. Prior HPF, all planchettes (A and B type) were plasma-cleaned from both sides with the same conditions as described above. Following this treatment, the flat side of B-planchettes were coated 3 times with 3 μl soy lecithin (1 mM in chloroform). The A-planchettes sides with 100 and 200 μm depth, were colour marked for better differentiation in the further procedure. To avoid later confusion, per session of up to 9 samples only one A-planchette side were used and marked. The A-planchettes were filled with PBS and samples applied. Subsequently, the flat side of a B-planchette were used to close the assembly and excess liquid removed by gently placing the assembly briefly on a tissue and immediately after high-pressure frozen. After freezing the assembly were recovered and disassembled in LN_2, whereby the marked side helped to differentiate which side of the A-planchette contained the sample.

4.2.4 Milling of AMF waffle grids & lamella preparation

AMF waffle grids were transferred to an autoloader and inserted into the Arctis Dual-Beam cryo-plasma focus ion beam (PFIB)(Thermo Fisher Scientific^{TM}; Oregon; USA) equipped with an integrated fluorescence light microscope module (iFLM) with a quad-band set for imaging samples with simultaneously labelled dyes. Regions of interest were coarsely identified using an electron beam at 25 pA and 2 kV at eucentric height, and fine aligned by fluorescence imaging. The stage was then tilted to -142° for trench milling perpendicular to the ion beam from the back side of the grid. The trenches were milled with a current of 16 nA and had the following dimensions: the side trenches were 1.6 μM wide and 40 μm long; the top trench was 15 μM wide and 10 μm long, and the bottom trench 15 μM wide and 45 μm long. The distance between the trenches for lamella preparation was 15 μM wide and 20 μm long. The trenches were refined by further tilting from 0° to -23° stage tilt to remove underlying material. The grid was then tilted to 0° and a milling pattern was placed to define the area for the undercut at a tilt angle of -10° and -20° with a nitrogen plasma beam at 4 nA and 30 kV.

After trench preparation, the target area and lamella sites were identified on scanning electron microscopy (SEM) images at eucentric height in comparison with the fluorescence images, and redefined if necessary. A conductive platinum layer was then sputtered onto the grid for 120 seconds at 70 nA and 12 kV Xe plasma to minimize charging effects during lamella preparation. Additionally, a platinum layer with a thickness of approximately 700 nm was deposited over a period of 2 min utilizing a gas injection system (GIS). Each lamella was thinned stepwise at a milling angle of 15° (-23° stage tilt angle) with gradually decreasing beam currents (from 1 nA to 30 pA) until the desired final thickness of 200 nm was reached. The process ended with a polishing step of the lamellae with 10 - 30 pA at 30 kV.

4.2.5 MILLING OF AMF PLANCHETTES & CRYO-VOLUME IMAGING

Prior to the milling procedure, a copper block (20 µm x 10 µm x 10 µm) was prepared from a copper grid and attached to the lift-out needle by re-deposition milling according to the protocol of Schiøtz *et al.* (2024) [152]. Subsequently, an HPF type A planchette and a clipped half-moon grid (Pelco; Kirwan, Australia), loaded in an autogrid, were inserted into a HPF-carrier shuttle (3 mm) with a pretilt of 35°. Subsequently, it was transferred to the cryo-stage of a Helios Hydra V Dual-Beam cryo-PFIB (Thermo Fisher Scientific$^{\text{TM}}$) with integrated iFLM (development version) and a cryo-lift-out manipulator. This instrument was used for extraction and transfer of volumes from a bulky HPF samples to a half-moon grid for further processing including lamella preparation.

Prior to imaging, a conductive platinum layer was sputtered onto the planchette using integrated micro-sputter (6 min; 99 nA; xenon plasma). The SEM image of the HPF planchette was acquired (12.5 pA; 2 kV) using MAPS (v.3.25) and aligned with the images acquired with the iFLM (pixel size 110 nm) to identify areas of interest. Subsequently, an approximately 1 µm thick platinum precursor layer was deposited over a period of 1 min using a cryo-deposition with GIS. The protective layer was necessary for subsequent lamella thinning and chunk polishing. The stage was then rotated 180° to proceed with creation of an imaging face. Milling was performed at an angle of 16° (stage tilt 13°) using an ion beam current of 15 nA for rough milling and 4 nA (30 kV) for polishing the imaging face. The trench dimensions were adjusted based on the sample and volume size. Trenches were milled around the volume to be extracted, with overlapping milling patterns. The volume size ranged from 20 µm x 30 µm x 10 µm (L x W x H) to 40 µm x 60 µm x 30 µm (L x W x H).

4.2.6 SERIAL FIB-SEM VOLUME IMAGING & VOLUME LIFT-OUT

The integrity of the sample was verified by volume imaging. Milling was performed at an angle of 16° (tilt angle 13°; ion-beam current 0.6 nA), with SEM imaging at 90° (stage tilt 51°; 25 pA; 1 kV), using AutoSlice&View (version 5; Thermo Fisher Scientific$^{\text{TM}}$) and FIBSEM Maestro software (https://github.com/cemcof/FIBSEM_Maestro). Once the integrity of the hyphae was confirmed, the procedure continued with the cryo-lift-out. An additional platinum layer was applied to the sample surface and the block‘s leading face for 4 min resulting in a thickness of 1 µm to protect the surface from beam damage during subsequent milling. The stage was configured for perpendicular milling (stage tilt: 17°; rotation: 0°). And trenches around the volume to be extended were milled with a minimum width of 10 µm. The lift-out needle with the attached copper block was moved adjacent to the sample to be extracted. Subsequently, the chunk was attached to the copper block by re-deposition using a single-pass pattern of regular cross-sections at the interface between the copper block and the aligned sample surface [152]. The lift-out was performed at a milling angle of 9° (stage tilt: 6°). The chunk was then transferred to a half-moon grid and the volume aligned by matching its edge to the prepared pin edge, then attached by re-deposition using a single-pass pattern of regular cross-sections (stage tilt: 38°; milling angle: 69°; 300 pA; 30 kV). The lit-out needle was released by milling away the connection between the copper block and the volume surface. After the successful lift-out and attachment to the half-moon grid, the volume and hyphae integrity were rechecked with iFLM, and automated volume imaging was repeated as described above, to fine-tune the positioning for lamella preparation [153]. This step helped to evaluate potential beam damage post-lift-out and created a smooth surface, that minimized milling artefacts during subsequent lamella preparation.

4.2.7 Lamellae Preparation from Volume Samples

The preparation of lamellae from volume samples was performed as described above according to the waffle method protocol [150]. A stage tilt of approx. 10° (milling tilt 13°) was used and the lamellae were thinned with gradually decreasing beam currents, starting from 4 nA, decreasing to 0.3 nA at 2 µm thickness and further to 0.1 nA at 1 µm thickness. At a lamella thickness of 500 nm or less, a beam current of 30 pA was used until the desired final thickness of 200 nm was reached. The process ended with a polishing step of the lamellae at 10 - 30 pA and 30 kV.

4.2.8 cryo-EM data aquisition & processing

Imaging of the prepared lamellae was performed using a 300 kV Titan Krios (Thermo Fisher Scientific^{TM}), equipped with a Bioquantum energy filter and a K3 direct electron detector (Gatan). A slit width of 10 eV was used for imaging. The lamellae were aligned perpendicular to the tilt axis of the microscope. Images were acquired at a magnification of 26,000x, corresponding to a pixel size of 3.473 Å. Four tilt series were collected using SerialEM [23] with a dose symmetric tilt-scheme in mode at 2.5° increment. The defocus was set to -6 µm, and the total dose was approximately 80 e-/A^2 with a constant electron dose per tilt image.

4.2.9 cryo-volume SEM data processing

Serial EM images were imported into Fiji and converted into image stacks. The image dimensions were adjusted while maintaining the original width-to-height ratio. Subsequent steps included contrast optimization and alignment using the stack contrast adjustment and template matching plug-ins. Although a stack suitable for 3D reconstruction was generated, a final volume rendering was not performed due to the absence of a consistent structural reference across slices, which impeded reliable spatial correlation.

4.3 RESULTS

4.3.1 SAMPLING TECHNIQUES FOR AMF HYPHAL NETWORK AND SPORES

The AMF samples were taken from the plates using different sampling techniques and transferred to either an EM grid (Fig. 4.1) or a planchette (Fig. 4.2), optimizing the process to ensure that the integrity of the samples was largely maintained. The use of the AMF hyphal network growing on the cellophane surface of the AMF plate resulted in a higher number of intact hyphae after high pressure freezing compared to other techniques. In this approach, the cellophane with the hyphal network was transferred to a new petri dish. Here, the network was gently washed off from the cellophane surface with PBS. This method enabled more efficient sampling and increased the likelihood that some of the hyphae remain intact for subsequent analysis. In contrast, the commonly used sodium citrate buffer method, in which the hyphal network is released by liquefying the agar, leads to loss of the cell content and predominantly empty hyphae. However, the sodium citrate buffer method was still the most effective way for extracting spores from the medium with minimal hyphal residue. The subsequent manual sorting of larger or dead spores, which were identifiable by a change in colour, also improved vitrification outcome.

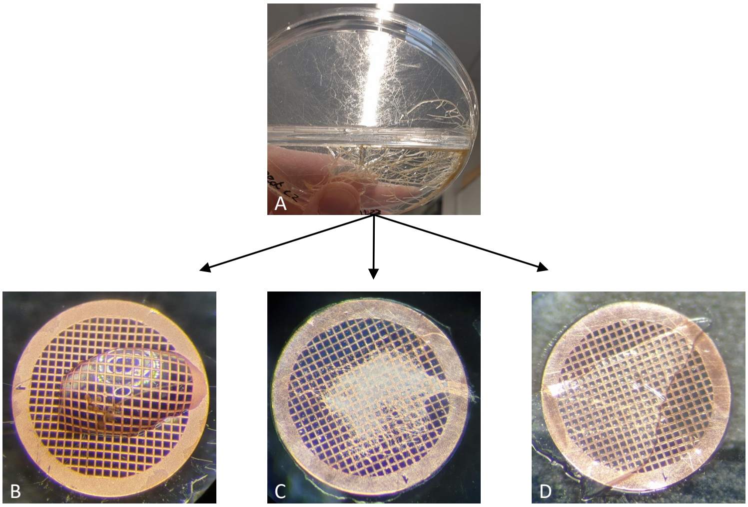

Figure 4.1: Sampling of AMF for cryo-EM sample preparation. The AMF plate consisted of two compartments separated by a membrane: one side contained the AMF with its host roots, while the other contained the hyphal network and spores. In the hyphal compartment, the medium was overlaid with cellophane to prevent desiccation, with the hyphal network and spore growing both within the medium and on top of the cellophane. (A) AMF plate showing the two compartments: AMF with host roots and hyphal compartment. (B) Spores with residues of hyphal network, released using the sodium citrate buffer method. (C) Hyphal network extracted from the medium by vigorous shaking the medium in sodium citrate buffer. (D) Cellophane section with branched hyphae. All samples were transferred either to a 3 mm planchette or to a 3 mm copper grid for further sample processing by high-pressure freezing.

Overall, the cellophane-surface sampling technique proved to be the most effective method for maintaining the integrity of the AMF hyphae and providing a reliable method for cryo-EM sample preparation and analysis.

In the later stages of the experiment, young germinated spores with their fragile germ tubes (young hyphae) were also used. The advantage of this technique is that the hyphae do not need to be cut, so their cell content remain intact. Handling these samples was challenging, as the germ tubes are fragile and can break during harvesting and transfer to the high pressure freezing assembly. To address this issue, the spores with their fragile germ tube were first detached from the cellophane surface with a small amount of PBS. Subsequently, a 100 µl pipette tip was partially filled with PBS and used to transfer the spores and germ tubes. To prevent loss of the sample by adhering to the tip's plastic surface, the filled pipette was depressed to keep a small drop of PBS on the tip, which was used to pick up the sample and transfer it to the high pressure freezing assembly. For efficiency and to increase the amount of sample material on the planchette, spores with their germ tubes were first collected in a larger PBS droplet and then transferred together using the described procedure (Fig. 4.2).

We also attempted to target specific areas of the hyphal network, particularly where hyphae branched, by cutting small pieces of cellophane containing these areas and directly placing them on a waffle grid for high pressure freezing (Fig. 4.1D). Although this approach was time-consuming, it allowed precise selection of specific hyphal regions. Notably, the cellophane proved suitable for PFIB milling, enabling access to the sample. However, this method introduced an additional layer of thickness, which increased the time required for subsequent milling. Additionally, prolonged handling during transfer onto the grid occasionally compromised hyphal integrity. To minimize leakage from the hyphae, one side was initially separated from the network, allowing a plug to form at the cut edges before detaching the other side.

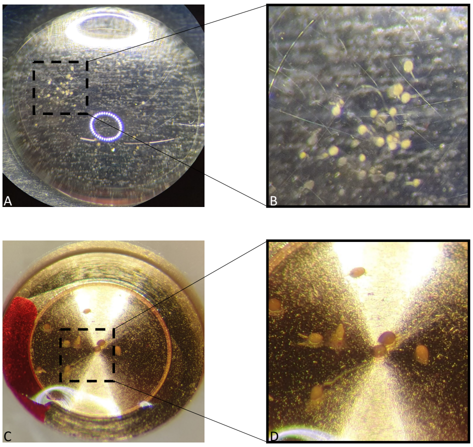

Figure 4.2: Germinated spores with germ tubes. (A, B) Germinated spores with intact germ tubes collected in a small PBS droplet. (C, D) The collected spores were transferred into a planchette to increase sample material, with spores and spores remaining intact.

4.3.2 Improved detectability through fluorescence staining

The use of fluorescent dyes to stain specific cell components significantly improved the detection of intact AMF hyphae suitable for lift-out and lamella preparation. At the beginning of screening of vitrified samples, we found that the detection of hyphae and spores after high-pressure freezing was challenging due to the formation of an almost uniform layer on the sample surface (Fig. 4.3A). In some cases, individual hyphal membrane structures were visible on the ice surface (Fig. 4.3B). However, these structures often exhibit low sample integrity during milling, making them unsuitable for lift-out and lamella preparation, as they would fragment during further processing. Therefore, the sample surface had to be milled blind, which was time-consuming and often led to suboptimal results.

The use of fluorescent dyes significantly enhanced the detectability of the sample material. Additionally, the targeted application of specific fluorescent dyes enabled selective milling of certain cellular components (Fig. 4.3C & D). The combination of these dyes further improved the process, allowing for differentiation between intact and non-intact hyphae prior to milling (Fig. 4.3E & F). This approach increased the likelihood of identifying intact hyphal regions suitable for further processing.

4.3.3 Vitrification methods for AMF samples

The modification of the waffle method using a newly designed snap-button planchette (J. Nováček; CEITEC Masaryk University; Brno; CZ ;unpublished) enabled the vitrification of samples with larger volumes, making it suitable for cryo-EM imaging of AMF hyphae (Fig. 4.4). When applying the waffle method, we encountered several challenges partly due to the characteristics of the sample. AMF spores, for instance, display significant size variability and age-dependent differences in wall thickness, both of which can affect the vitrification process. Additionally, AMF hyphae showed a low affinity to metallic surfaces and even show repulsive behaviour, complicating their application to copper grids despite additional coating with carbon or gold. This repulsion sometimes led to the loss of sample as the material adhered to the edges of the grids or other surfaces.

To overcome these challenges, custom-designed snap-button planchettes were used in subsequent experiments (Fig. 4.4). These planchettes allowed the use of clipped grids, with the clip ring providing an additional 100 µm of space for the sample (Fig. 4.4D & F). This extra space enabled the application of a small drop of buffer or cryoprotectant onto the grid, forming a dome that facilitated the transfer and positioning of AMF hyphae onto the grid. The snap-button planchettes reduced the assembly time needed and increased the recovery rate of intact grids following high-pressure freezing. By pre-clipping the grid, it minimized the risk of sample loss during post-freezing clipping. Moreover, the snap-button method was also suitable for young and small spores, though direct high pressure freezing of AMF spores in planchettes was more suitable for handling a range of spore sizes and was similarly advantageous for high-pressure freezing of germinated spores (Fig. 4.2).

After high-pressure freezing the autogrid (clipped grid) was loaded into a PFIB, the area of interest was identified using fluorescence microscopy and compared with SEM imaging (Fig. 4.5). The milling pattern was then applied using the waffle method, and the milling process was initiated. During lamella preparation, the milling process had to be monitored regularly to ensure that the final lamella contained hyphae and was not over-milled (Fig. 4.5B & C). This was particularly important, as fluorescence and SEM microscopy could only provide a rough estimate of the Z-height of the area of interest. As shown in figure Fig. 4.5B, when it became evident during rough milling that the area of interest (hyphae) had been missed or milled away, the milling position was adjusted and rough milling was repeated. Such adjustments were more manageable during the rough milling stage compared to the fine milling stage, where the risk of damaging or losing the newly prepared lamella increased. Additionally, a change in the gas used for the plasma-focus ion beam was necessary, as the nitrogen-based beam proved to be too rough for fine milling, causing curtaining and even fracturing of the lamella. Therefore, oxygen plasma was used for the fine milling steps, as it minimized the curtaining effect and allowed the successful preparation of a lamella from hyphae with a thickness of approximately 200 nm. Overall, the use of custom-designed snap-button planchettes significantly improved the efficiency and reliability of vitrification for AMF samples.

4.3.4 Challenges during milling and serial-SEM imaging

As mentioned above, different sample extraction procedures let to various complications and artefacts, which often only became evident during PFIB-SEM or even later during cryo-EM analysis. One of the most common issues encountered during PFIB milling was the presence of empty hyphae, which had lost their contents during sample extraction (Fig. 4.6). The use of sodium citrate buffer in the extraction process resulted in loss of cellular content, sometimes causing cavities within the hyphae (figure 4.6B & D). This negatively affected the high-pressure freezing process and led to suboptimal vitrification of the AMF sample.

To address these challenges and improve the preservation of cellular content, we decided to use hyphae material obtained from the cellophane surface. This method, being gentler, allowed for significantly faster processing from hyphae extraction to high-pressure freezing, leading to better sample preservation. While it also contributed to improved vitrification, the primary benefit was in maintaining the sample's integrity. Additionally, the choice of cryoprotectant used during HPF played a crucial role in maintaining sample integrity and reducing PFIB milling time.

Hexadecene, a widely used cryoprotectant, caused the hyphae to react repulsively, making it difficult to apply the sample onto the grid or planchettes, thus increasing the time required to prepare the sample for high-pressure freezing. This prolonged preparation time further complicated the process of obtaining sample with high cell integrity.

Moreover, vitrified hexadecene was found to be a hard material, which prolonged milling times. Another disadvantage of using hexadecene was the frequent occurrence of cracks and fractures in the vitrified sample during milling (Fig. 4.6C & D). These issues were likely due to the increased beam exposure time required by the higher material hardness of hexadecene.

An alternative cryoprotectant, PBS, proved to be more suitable for AMF samples. Hyphae reacted more favourable to PBS, and it also facilitated faster milling. Although cracks and fractures still occurred during milling in samples vitrified with PBS, their frequency was lower compared to samples vitrified with hexadecene.

Apart from the challenges mentioned above, the variability of the hyphae also posed a challenge during milling and serial imaging. Hyphae can contain various types of minerals transported through the hyphal network, which can exhibit different charging effects, leading to artefacts during serial imaging in the slice & view procedure. By optimizing extraction, using PBS as a cryoprotectant and applying oxygen-based plasma for fine milling, challenges such as low sample integrity and artefacts were mitigated, improving serial-SEM imaging and lamella preparation.

In addition to the hyphae, spores of different sizes and maturities were also vitrified. During the course of the experiments, it became apparent that the vitrification of older, more mature spores was often inconsistent and unreliable. Furthermore, mature spores exhibited considerable hardness during milling, requiring a higher beam intensity, which led to beam-induced damage to the more sensitive spore contents (Fig. 4.7A&B). In contrast, small, young spores allowed for the successful production of lamellae, although the spore cell wall remained a challenging material to mill, often requiring several hours or even days to fully mill through (Fig. 4.7C&D). Initial lamella preparations were promising but due to the different material properties of the spore cell wall and its contents, the lamellae frequently disintegrated and were lost during the fine milling procedure. As a result, the focus of the experiments shifted towards lamella preparation and subsequent cryo-EM data collection of mature hyphae.

4.3.5 CHALLENGES IN AMF HYPHAL ULTRASTRUCTURE VISUALIZATION

Cryogenic sample preparation enabled detailed insights into the hyphae and the spatial organization of their cell content, primarily consisting of lipid vesicles (Fig. 4.8). Other cell organelles, as well as the various layers of the cell wall and plasma membrane, were visualized in a near-native state. Further processing of the vitrified AMF hyphae using PFIB-SEM and the slice & view approach enabled serial imaging and provided a dataset suitable for 3D reconstruction (Fig. 4.8). After confirming the integrity of the hypha through serial-PFIB-SEM, lamellae were produced from the sample volume.

Due to the large sample volume, another challenge arose: the increased relocation of ice and milling residues, which preferentially deposited on charged surfaces such as the surrounding area of the milled lamella or directly on the lamella surface (Fig. 4.9). This contamination led to longer milling times and often resulted in the loss of lamellae. The risk of ice crystal contamination increased during the transfer from PFIB-SEM to cryo-EM, leading to a continued reduction in lamellae quality or in many cases, additional lamellae loss. In particular, loading and unloading of the samples into different cryogenic devices was the most critical point where most contamination and lamella loss occurred. Only a few lamellae were suitable for cryo-EM imaging. Despite these challenges, preliminary cryo-EM images obtained from hyphae provided early insight into their ultrastructure at near native state.

As shown in figure 4.9, a network of vesicle-like structures and bundles of filaments were imaged. Although lamellae preparation and contamination presented challenges, the initial cryo-EM imaging revealed high-resolution structural features of mature AMF hyphae in a near-native state.

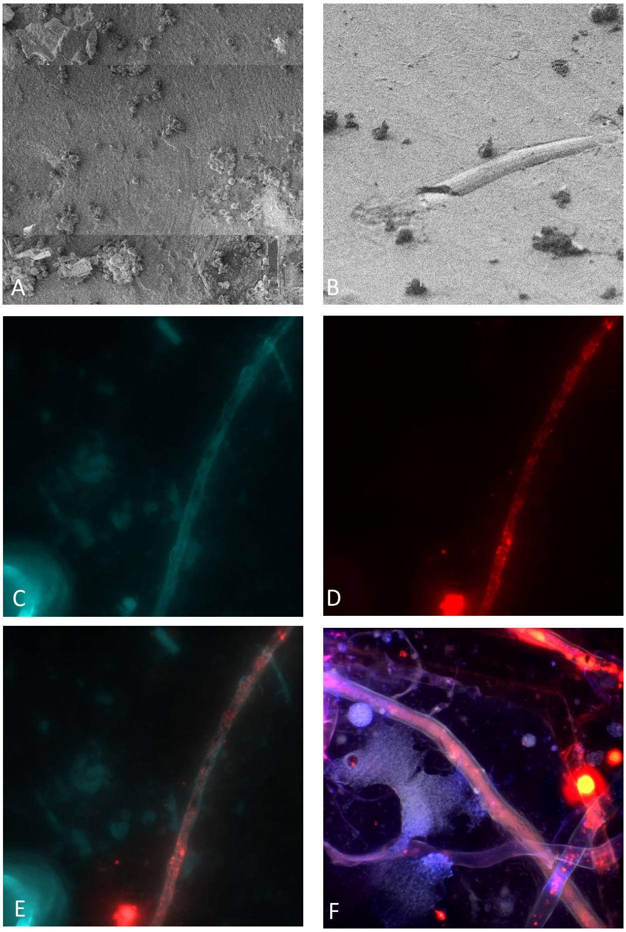

Figure 4.3: Fluorescence labelling of AMF hyphae. Fluorescence labelling facilitated the identification and targeted milling of AMF hyphae within the ice layer. (A) Nearly uniform ice layer on the grid surface after high pressure freezing, which made the detection of AMF hyphae for PFIB milling difficult. (B) AMF hyphae membrane on the surface of the ice layer on grid. (C) AMF hyphae stained with CFW, which labels chitin and cellulose. (D) AMF hyphae stained with NR, which labels membrane lipids and lipid vesicles. (E) Combined CFW and NR staining for identification of intact hyphae areas. (F) Multi-dye fluorescence labelling (DAPI; Mitotracker; CFW; NR) used to target specific cellular compartments, including mitochondria (Mitotracker) and nuclei (DAPI).

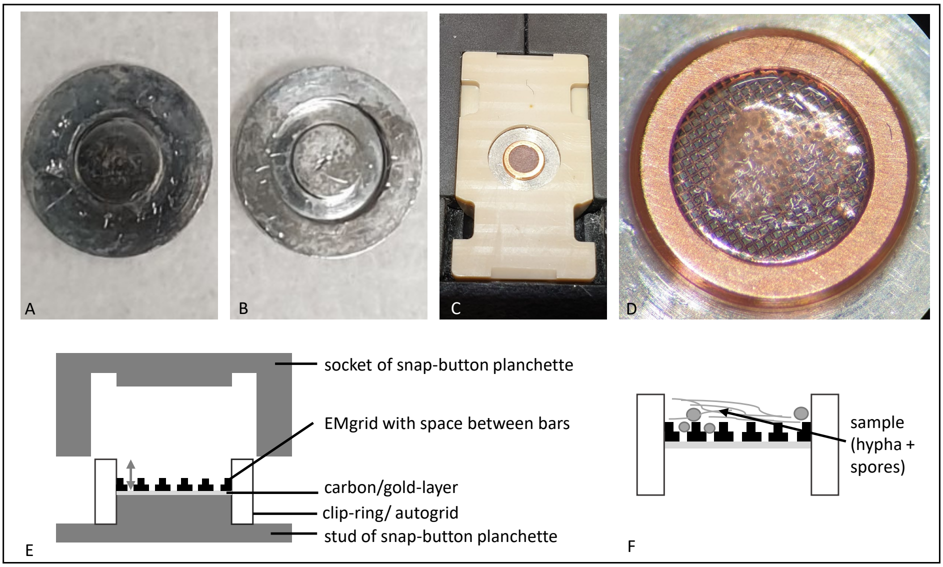

Figure 4.4: Snap-button planchette for high-pressure freezing of larger volume samples. (A) Stud and (B) socket of snap-button planchette (6 mm). (C) Positioning of clipped grid and assembly of snap-button planchette. (D) AMF hyphal network applied to the centre of clipped grid within the assembly, after moistening with a drop of PBS to improve sample adherence and positioning. (E) Schematic representation of snap-button planchette assembly, with the grey arrow indicating sample space. (F) Schematic representation of the sample space on a clipped grid.

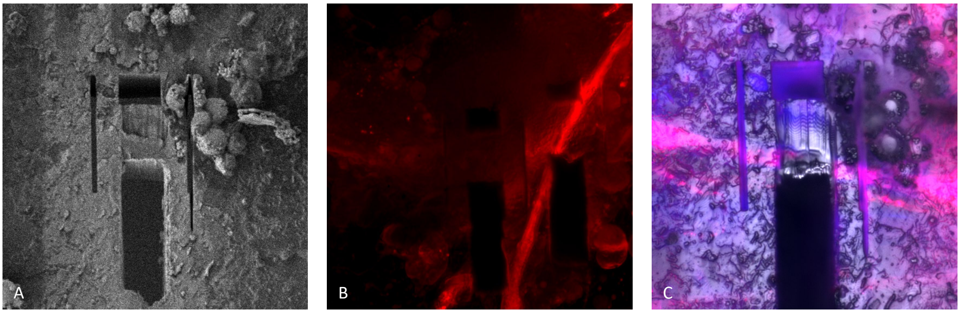

Figure 4.5: Lamella preparation of AMF hyphae sample. (A) Rough milling of trenches using artefacts as orientation points on the nearly uniform ice layer. (B) Placement of milling pattern for rough milling, aligned with fluorescence microscopy, and adjustment of pattern positioning if the area of interest was missed. (C) Alignment of SEM and fluorescence imaging of final lamella, with hyphae material positioned on the lower edge. Despite imprecise Z-height positioning leading to missed half of hyphae material during fine milling, a fine lamella (~200 nm thick) was successfully milled and transferred for cryo-EM imaging.

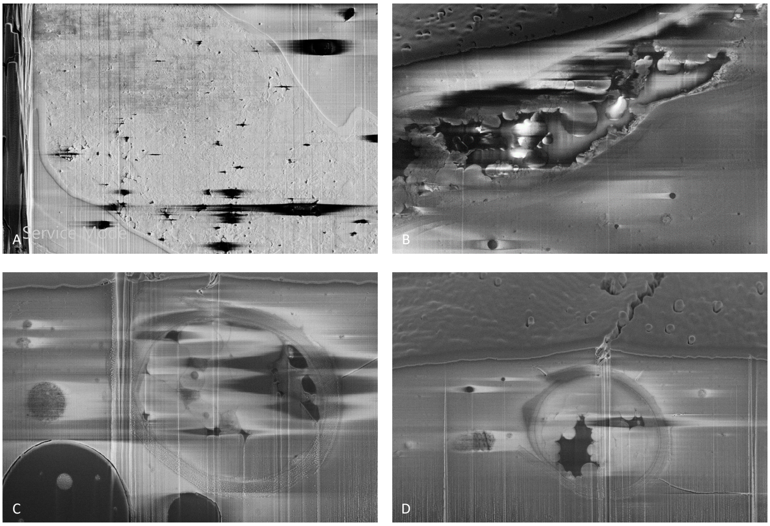

Figure 4.6: SEM images of AMF hyphae during milling using PFIB-SEM, showing various artefacts from sample treatment and HPF procedure. (A) Lateral view of a hyphae that has lost its cellular content, with only the cell wall and collapsed plasma membrane remaining. (B) Lateral view of a partially filled hyphae, showing large gaps due to the loss of cellular content. (C, D) Front view of partially filled hypha, showing artefacts such as cracks and holes in the surrounding ice, which challenged further processing.

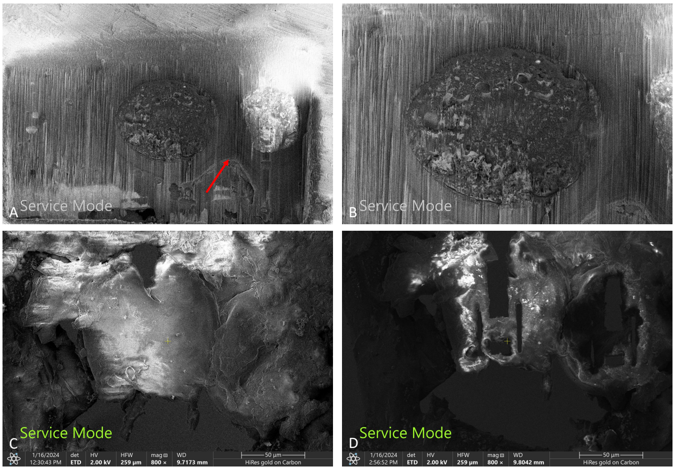

Figure 4.7: SEM images of AMF spores during rough milling, acquired using PFIB-SEM in preparation for lift-out and lamella milling. (A; B) Milling of a mature spore required the use of higher voltage due to the thick, multilayered spore cell wall, resulting in milling artefacts and beam-induced damage to the spore contents. (C) Small spores vitrified on a grid used for (D) lamella preparation. The red arrow points to a hyphal connection between the spore and the hypha.

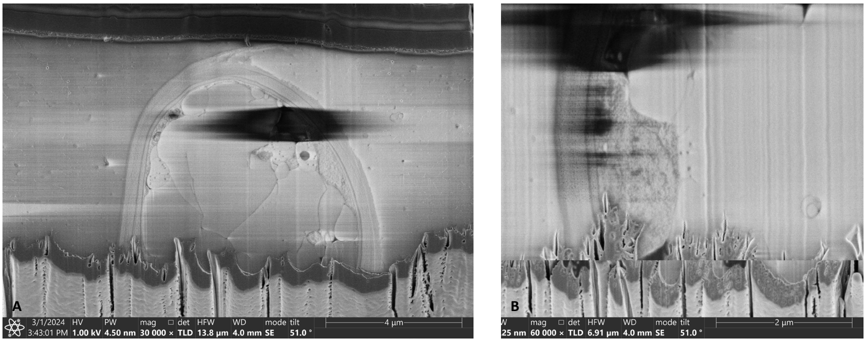

Figure 4.8: SEM images of a nearly intact hyphae obtained using autoslice & view approach at a PFIB-SEM. (A) Front view of a hyphae with nearly intact cellular content. (B) Detailed view of the cell wall layers and cell organelles. Scale bar: (A) 4 µm; (B) 2 µm.

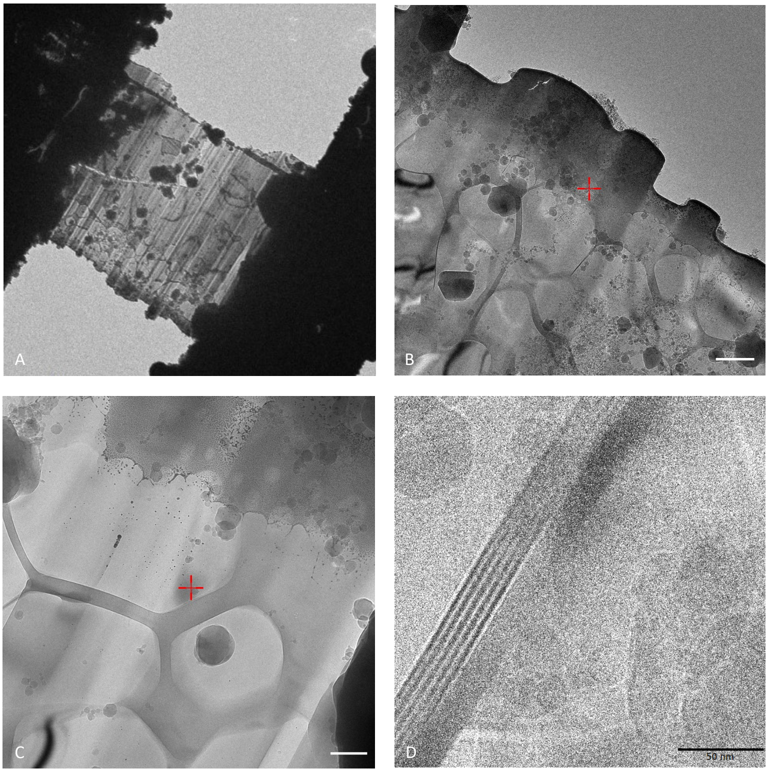

Figure 4.9: Lamella of AMF hyphae and initial cryo-EM images. (A) Lamella containing hyphae, surrounded by ice crystal contamination. (B; C) Detailed view of hyphal content, showing a fine network between vesicles. (D) Cryo-EM image of a filament bundle of AMF hyphae, which could not be further classified due to their unclear positioning. Scale bar: (B) 500 nm; (C) 200 nm; (D) 50 nm.

4.4 DISCUSSION

We know that high-resolution insight into 3D structures is a powerful tool to gain a detailed understanding of cellular components and their interactions. Cryopreservation preserves the cellular ultrastructure in near-native state, while advanced cryo-ET techniques enable high-resolution 3D visualization that allows the spatial distribution of cellular components to be studied in unprecedented detail. In this study, we applied and successfully modified the cryo-EM sample preparation procedure making it suitable for AMF samples, including hyphal network and spores, enabling high-resolution imaging of their ultrastructure. Improvements in sample handling allowed better preservation of the cellular content of mature hyphae while high-pressure freezing and to continue further sample processing in cryo-stage preserved the ultrastructure of the AMF samples. This breakthrough enabled, for the first time, the visualization of mature AMF hyphae and the investigation of distribution patterns of cell organelles, their interaction with the plasma membrane, and potential contributions to bidirectional transport of goods.

In the initial stages, the waffle-method was used for high-pressure freezing [150]. This method involves placing the sample on a grid sandwiched between the flat sides of two B-planchettes. While this approach is described in the literature as effective for samples up to 25 µm (width) x 50 µm (depth) and a length up to 100 µm [150], it presented several difficulties when applied to AMF samples. One major limitation was the restricted sample thickness, determined by the grid bar depth, typically limited to around 50 µm. This depth could be extended by 50 µm using a metal spacer (3 mm), but this introduced additional challenges. During the HPF process, the assembly of grid, spacer, and sample frequently slipped, leading to misalignment of the sample relative to the grid centre. If the sample was positioned too far-off centre, it became difficult and even impossible to process further in the PFIB-SEM or cryo-EM due to the physical limitations of ion beam alignment on the sample. Furthermore, the samples showed a tendency to be repulsive to metal surfaces, making it challenging to apply and to position the sample at the centre of the grid.

After HPF, recovering intact grids became another significant issue. The disassembly process often damaged or deformed the grids, leading to a low recovery rate of usable sample-grids (HPF grid with sample material). The subsequent required clipping of sample-grids for the further sample processing introduced additional complications. This extra handling step increased the risk of ice crystal contamination and frequently caused detachment and complete loss of sample material during clipping.

Given these challenges, the original waffle-method proved unsuitable for preparing AMF samples for vitrification and subsequent lamella preparation procedure.

To overcome the limitations, we modified the existing waffle method to make it more suitable for AMF samples and other larger-volume samples (50 – 150 µm thickness). One key adjustment was the use of pre-clipped grids (autogrids) in the HPF carrier-sample assembly. This change streamlined the process, reduced the risk of sample loss and minimized the risk of ice crystal contamination. The clip ring height also provided approximately 100 µm of extra sample space, enabling better accommodation of thicker samples (up to 150 µm). Additionally, the clip ring protected the sample-grids (HPF grids with sample material) during disassembly, contributing to a higher recovery rate of intact sample-grids. While traditional planchettes with sample spaces of 100 to 300 µm (per side) were typically used for larger volume samples (>10 µm), this often led to excess cryoprotectant surrounding the sample [154]. This in turn, required more extensive milling during the lift-out procedure and lamella preparation. To minimize this, a new planchette design, termed snap-button planchettes, was introduced. This redesign facilitated smoother disassembly, increasing the likelihood of obtaining intact sample grids while ensuring proper sample positioning during high pressure freezing. The reduced surrounding volume also minimized the cryoprotectant usage and subsequent milling efforts.

Although the modifications developed in this study significantly improved the vitrification quality of AMF samples and greatly increased the recovery rate of intact sample grids after high-pressure freezing, challenges remain. A particular low success rate of milling thin lamellae and even fewer successful cryo-EM imaging sessions due to ice crystal contamination still hinder consistent outcomes. Addressing these limitations, a potential solution could involve integrating an ice crystal and milling residue trapping system, similar to the cold finger anticontaminators used in transmission-electron microscopy (TEM). This system could be adapted to not only provide a cold surface to attract particles but also incorporated a charged layer specifically designed to trap ice and milling residues. A charging layer could be created through a surface charging step, where a targeted region of the trap is charged by milling a small surface, creating a charged region that efficiently traps contaminants.

The trap could ideally be applied throughout the entire milling process, with the most significant reduction in contamination risk likely occurring during the fine milling step. At a minimum, it could be applied also only during fine milling of the lamellae. However, further testing and development are needed to validate this approach.

Another important avenue for improvement lies in optimizing fluorescence microscopy at cryogenic temperatures. Testing a range of fluorescence dyes to identify those that are suitable for cryogenic conditions, with low photobleaching during milling and imaging, is crucial. The use of cryo-compatible dyes, especially those that can specifically target cellular organelles such as ER-Tracker or BODIPY-brefeldin A — successfully applied in other fungal system [155] — would significantly enhance the ability to identify and localize organelles within AMF hyphae. This would not only aid in organelle classification but also facilitate deeper insights into their roles in nutrient transport, storage, and the underlying regulatory mechanisms.

Using the advanced vitrification method for AMF samples described above, we were able to image mature hyphae in unprecedented detail, revealing their ultrastructure in a near-native state. The cell wall morphology was consistent across mature hyphae, regardless of their diameter. As previously reported in the literature, hyphae were primarily filled with lipid vesicles. However, in contrast to other studies that mainly investigated germ tubes and young hyphae, the lipid vesicles in the mature hyphae often appeared large and interconnected, with indistinct boundaries. Cell organelles were distributed along the hyphae but frequently clustered together. Some were positioned on the plasma membrane, while others were distributed within the cytoplasm. Initial cryo-EM images suggested a network-like structure among the vesicles, though further investigations are needed to confirm these findings. Notably, no septum or additional layer was identified that could explain the organization of the bidirectional transport system within the hyphae.

While these biological insights shed light on the structural complexity of AMF hyphae, the technical challenges in preserving these delicate features required significant refinement of the high-pressure freezing process.

Looking ahead, as advancements in lamella preparation for large-volume samples continue to evolve, the success rate for imaging such samples at high resolution is expected to improve rapidly. The methodologies developed in this study, including the optimized sample preparation of mature AMF hyphae and the design of snap-button planchettes, are well-positioned to play a pivotal role in advancing research in this field. These methods pave the way for high-resolution cryo-ET data collection, offering unprecedented opportunities to investigate AMF ultrastructure in a near-native state and to address fundamental questions in AMF biology with greater clarity and precision.

ACKNOWLEDGEMENTS

J.L. was supported by the OCENW.GROOT.2019.063 and Building Blocks of Life 737.016.00 grants from the Netherlands Organization for Scientific Research (NWO), both awarded to A.B. This work benefited from access to the Electron Microscopy facility in Brno, Czech Republic, an Instruct-ERIC centre. Financial support was provided by Instruct-ERIC (PID: 27640) as well as through the Instruct-ERIC Internship Call (APPID: 3188). We also gratefully acknowledge the CF CEITEC/Brno – Cryo-electron Microscopy and Tomography facility of CIISB, Instruct-CZ Centre, supported by MEYS CR (LM2023042) and the European Regional Development Fund – Project „Innovation of Czech Infrastructure for Integrative Structural Biology“ (No. CZ.02.01.01/00/23_015/0008175).

AUTHOR CONTRIBUTIONS

J.L. developed the sample preparation and cryo workflow, designed and coordinated the study, performed most experiments including sample preparation, vitrification, fluorescence imaging, and initial cryo-PFIB/SEM sessions, and wrote the manuscript. J.M. and P.K. provided training and technical support at CEITEC, jointly operated the cryo-PFIB/SEM system with J.L., and carried out lamella preparation, lift-out procedures, and cryo-EM data acquisition. They also contributed to the PFIB/SEM Methods section. M.v.S. prepared the AMF(C2) infected (Ri) T-DNA transformed root organ plates, provided additional sample material, and supported the preparation of germinated spores. J.N. designed the snap-button planchette and provided technical advice. V.K. provided scientific input. T.S.S. and T.K. supervised the Amsterdam component and enabled the collaboration. A.B. supervised the project and provided feedback on the manuscript.

5

Large-volume sample preparation of plant-tissue for cryo-electron microscopy

Cryo-electron microscopy (cryo-EM) and tomography (cryo-ET) are increasingly applied to investigate structural interactions in host-microbiota systems at the nanoscale. While initial studies focused on single cells, recent technological advancements have expanded cryo-EM applications to large-volume (LV) samples, including tissue specimens. However, plant tissues pose unique challenges for vitrification due to structural barriers such as rigid cell walls, vacuoles, and intercellular gases, which hinder uniform cryo-fixation and leading to detrimental freezing artefacts. To address these limitations, we optimized the workflow for LV plant tissue vitrification and evaluated different plant tissues. Reproducible vitrification of plant tissue was achieved through the combined use of PFIB/SEM, cryo-lift-out techniques, methodological improvements (e.g., planchette modifications, enhanced sample handling), and root organs as a model system. These root organs are a well-established system for studying plant-microbiota interactions, and their thin diameter and lower risk of the formation of intercellular gas further improved vitrification outcomes. This approach enables cryo-EM studies of plant-microbiota interactions in a near-native hydrated state, allowing high-resolution imaging. The developed workflow provides a foundation for high-resolution imaging of plant tissue ultrastructure, expanding future applications in plant biology and microbiome research.

This chapter is based on a manuscript by **Liedtke, J.**, Křepelka, P., Moravcová, J., van Son, M., Nováček, J., Kokkoris, V., Shimizu, T. S., Kiers, T., and Briegel, A.: Optimizing cryoEM sample preparation for high-resolution imaging of the ultrastructure of AMF hyphae, in preparation.

5.1 INTRODUCTION

In recent studies, cryo-electron microscopy (cryo-EM) has increasingly been used to investigate host-microbiome interactions, as it allows the visualization of ultrastructural features in their native cellular context and enables the characterization of interactions at the nanoscale. While early efforts focused primarily on the cellular level using cell cultures, these techniques have recently been extended to tissue samples, thereby offering insight into more complex biological systems [45, 50]. Meanwhile, the term "large-volume" (LV) samples has appeared more frequently in the literature, often without further explanation or definition. In general, it is used to describe samples that are composed of multiple cell layers (e.g., biofilms) or multicellular specimens that exceed the dimensions of individual eukaryotic cells. However, a precise size threshold for LV samples has not yet been established and remains an open question in the field. Traditionally, samples for cryo-EM analysis with a volume of less than 10 µm were vitrified by plunge freezing, where the sample is applied onto a copper grid (3 mm) and rapidly plunged into liquid ethane, which is cooled by liquid nitrogen. Samples exceeding 10 µm require high-pressure freezing (HPF) for vitrification, where the sample is frozen within milliseconds under high pressure (~2100 bar) in liquid nitrogen [156]. Notably, most studies focus on metazoan tissue, whereas research on phyto-tissue remains limited. This is due to the challenges associated with vitrifying plant tissue. Unlike metazoan cells, plant cells possess a rigid cell wall, large vacuoles, and intercellular gases, which complicate uniform vitrification and contribute to freezing artefacts and structural damage.

The majority of postulated vitrification procedures of plant samples have been developed for single cells like algae [157], leaves, or peelings of the outer epidermal layers, which are thinner than 15 µm and can be vitrified directly on a grid via plunge freezing. Another often described approach is the vitrification of root tips of young Arabidopsis seedlings which were high-pressure frozen and subsequently subjected to freeze substitution. This technique combines cryofixation with sectioning at room temperature, whereby the water within the frozen sample is slowly replaced with organic solvents. The advantage of this method is that it allows the sample to be processed at room temperature, enabling the preparation of sections suitable for cryo-EM using microtomes and ultramicrotomes. However, this extensive sample processing can degrade resolution and image quality, and the potential impact of solvents on ultrastructures remains uncertain [41, 158]. For this reason, previous studies have attempted to cut vitrified samples using cryo-ultramicrotomy. While this approach eliminates solvent-related alterations, it remains highly time-consuming and requires extensive expertise and manual dexterity. Additionally, cryo-ultramicrotomy frequently results in artefacts and tissue damage, limiting its reliability [159]. Due to these drawbacks, as well as the specialized skills required, the method has seen little mention in the literature in recent years. The development of focused ion beam scanning electron microscopy (FIB/SEM) has provided an alternative to microtomy, reducing the complexity of sample preparation. FIB/SEM integrates an electron column for imaging and an ion column for milling, allowing real-time monitoring and fine-tuning of the milling process while precisely ablating material with gallium ions. In this process, a defined rectangular region is milled down to 100–200 nm, creating an electron-transparent area, referred to as a lamella, which is suitable for high-resolution cryo-EM imaging [160].

However, larger sample volumes significantly extend milling times and simultaneously increase the risk of localized partial de-vitrification and subsequent ice crystal formation due to prolonged beam exposure [160]. The advancement of the FIB/SEM led to the development of plasma-FIB/SEM (PFIB/SEM), which allows the use of multiple ion species (xenon, nitrogen, argon, oxygen), each with distinct milling properties. The use of xenon ions, enables significantly higher material sputtering rates at the same ion beam current as gallium, due to their greater ion mass [161]. The advantages of PFIB/SEM over FIB/SEM have already been demonstrated in various studies and can be summarized as follows: PFIB/SEM allows the processing of significantly larger volumes while reducing surface roughness and minimizing beam damage that negatively impacts high-resolution imaging. This not only increases efficiency substantially but also enables further optimization of the milling process for lamellae of LV samples [147, 162].

The simultaneous development of the cryo-lift-out method has provided a breakthrough in large-volume cryo-EM sample preparation. For the first time, this technique allows the extraction of small volumes from LV samples and their transfer to new grids. This minimizes the amount of volume that must be milled around the area of interest to obtain electron transparent lamellae, thereby reducing milling time and mitigating the associated challenges described above [160]. This improves both efficiency and the preservation of vitrified ultrastructures during the milling process. However, initially HPF samples had to be recovered and mounted on a grid, e.g., with cryo-glue, to enable processing via (P)FIB/SEM and cryo-lift-out [163]. This additional step increased complexity and reduced overall efficiency. The ongoing development of other methods, including the waffle method, enabled to HPF samples directly onto a grid. This significantly improved efficiency but remained limited to sample thicknesses of up to 50 µm [150]. Further technological advancements introduced new shuttles, which enabled the direct use of planchettes in (P)FIB/SEM, eliminating the time-consuming and inefficient recovery and mounting steps.

In this study, we aim to develop a workflow that integrates recent technological advancement to obtain lamellae from LV samples of plant tissue. To achieve this, we optimized the vitrification procedure and tested various plant tissues to identify a suitable model organism. This approach enabled the preparation of vitrified plant tissue samples for high-resolution cryo-EM imaging, allowing us to visualize host-microbiota interactions at an unprecedented ultrastructural level.

5.2 Material & Method

5.2.1 Sample types

Root tissue samples were obtained from various plant species: garden cress (*Lepidium sativum*), radish (*Raphanus sativus*), arabidopsis (*Arabidopsis thaliana*), and sugar beet (*Beta vulgaris*). Plants were obtained from a local market or grown on media plates, as described below.

Furthermore, (Ri) T-DNA transformed root organs (here after: root organs) of *Daucus carota* and *Lycopersicon esculentum* grown on standard MSR medium were provided by the group of Kokkoris & Kiers (Vrije Universiteit Amsterdam), who received the root organs from Goh *et al.* (2022) [148].

Plant seed sterilization

Seeds were sterilized with 70% ethanol and a 4% sodium hypochlorite solution (Glorix) and washed at least five times with sterilized water until no foam appeared. The treatment was repeated twice and between each step the treatment agent was discarded and the seeds collected with a fine sieve. The exposure time to each substance varied among seed types. Seeds of *Lepidium sativum* and *Arabidopsis thaliana* were treated in the same way, with an exposure time of 1 min in ethanol (70%) and 15 min in bleach (4%). The seeds of *Beta vulgaris* needed to be soaked and washed in water first to remove the seed coating prior to sterilization. Since the seeds of *Beta vulgaris* and *Raphanus sativus* are lager, the exposure time to each agent was set to 5 min in ethanol (70%) and 15 min in bleach (4%). All sterilized seeds were either directly used or stored at 4 °C for a maximum of 2 days.

Plant growth conditions

Sterilized seeds were germinated and grown on 1/2 Murashige & Skoog plates (MS) with 1% (w/v) agar (Daishin agar; gel strength 700–800 hg/cm^2; Duchefa Biochemie) and 1% (w/v) sucrose. After germination in the dark at 21 °C, the seedlings were further grown in a plant chamber with the following conditions: 21 °C/21 °C day/night temperatures; 180 µmol light m^{-2} s^{-1} at plant level, relative humidity 50%; day-night-cycle 16/8 h. After 5–7 days of growth post-germination, the young root tips were used for the cryo-EM large-volume sample preparation procedure.

Bacterial strain and plant root inoculation

A GFP-labelled strain of *Flavobacterium anhuiense* (unpublished), obtained from the Balazadeh lab (Leiden University, NL), was grown in LB medium with ampicillin (0.1 mg/ml) and erythromycin (0.1 mg/ml) at 25 °C and shaking at 200 rpm. Cultures were assessed for GFP expression prior further use, using a fluorescence light microscope (DMi8 M; Leica Microsystems GmbH, Austria). Overnight cultures of *F. anhuiense* were used for the plant root inoculation procedure without further quantification.

Plant roots grown on 1/2 MS for 5–7 days were inoculated at their root tip with 100 µl of an overnight culture of *F. anhuiense* and incubated in the dark for 30 min. After inoculation, the roots were washed twice with sterile PBS. Subsequently, the inoculated roots were further processed by high-pressure freezing and lamella preparation.

5.2.2 3D printed biopsy needles

To extract intact tissue samples of homogeneous size, a biopsy needle was developed in the Briegel laboratory, enabling precise sampling from different tissue regions, as described in Depelteau (2022) [163]. The needles were made from photoactive resin using a Nanoscribe Photonic Professional GT 3D printer (Nanoscripe GmbH & Co. KG, Karlsruhe, Germany). The biopsy needles were mounted onto the tip of pins that had been previously inserted into 200 µl pipette tips. This assembly was then inserted into a customized injection device. The biopsy needle was either inserted using the spring system of the injection device or manually. The stability of the biopsy needle was assessed on plant roots and stems of different developmental stages. Subsequently, biopsy needles containing the obtained samples were subjected to HPF.

5.2.3 HISTOLOGICAL AND FLUORESCENCE STAINING

Histological staining of plant roots facilitated the retrieval and sample assessment after high-pressure freezing. Histological staining of plant roots was first performed with bromothymol blue (64.1 µM) dissolved in sterile tap water for 4-5 minutes. After staining, the roots were washed twice with sterile tap water to remove excess stain. During workflow development, we replaced bromothymol blue with methylene blue (31.3 µM), due to its fluorescent properties [164], which allowed detection using the Helios 5 Hydra DualBeam (PFIB) with an integrated fluorescence microscope (iFLM). Methylene blue was directly applied to the plant growth media plate and incubated for 20 min at room temperature (RT) in the dark. After incubation, the roots were cut off and washed twice with sterile tap water and high-pressure frozen.

During the workflow development, we discovered that the fluorescence signal of methylene blue was too weak and faded too quickly. To improve visualization and enhance detection of area of interest, a combination of Nile red (NR, for lipid staining) and calcofluor white (CFW, for cellulose, BactiDrop^{TM}, Remel^{TM}, Thermo Scientific^{TM}) was used instead. Nile red (Nile blue A oxazone, Sigma-Aldrich) stock solution (50 mg/ml in DMSO) was diluted (1:100), and 100 µl was pipetted on the surface of a plant growth medium plate (⌀9 cm). After 60 minutes of incubation at RT in the dark the excess stain was removed, and 100 µl of a 1:46 diluted CFW solution was added. After another 45 minutes of incubation (RT, in the dark) the excess stain was removed, and the plate washed twice with PBS. Stained roots were cut off with a surgical spring-loaded scissor and used for the high-pressure freezing procedure.

Assessment of fluorescence stained root tissue and imaging was performed using a fluorescence microscope (DMi8 M; Leica Microsystems GmbH, Austria). Stained and washed root tissue were placed in an ibidi microscopy dish (35 mm, glass bottom, ibidi GmbH, Gräfeling, DE) with a small amount of PBS to prevent dehydration. Imaging was conducted at RT using the Leica microscope software. Images were acquired with 20x and 40x objectives, using the default exposure setting and the built-in filter sets for the respective fluorophores.

5.2.4 HIGH-PRESSURE FREEZING

VITRIFICATION OF BIOPSY NEEDLE

Biopsy needles containing samples were HPF with either 10 % Ficoll PM400 (Cytiva^{TM}) or n-hexadecene (Sigma-Aldrich) as cryoprotectants. As described in Depelteau (2022) [163], the needles were placed in 3 mm A-planchettes, positioned on the 200 µm deep side, filled with cryoprotectant and closed with a pre-filled 100 µm deep A-planchette side. HPF was performed using a Leica EM ICE. To avoid additional handling step post-freezing, a grid was incorporated in the assembly so enable direct freezing of the needle onto the grid. Following HPF, the biopsy needles containing samples were recovered and stored in cryoboxes in LN_2 until further use.

VITRIFICATION OF PLANT ROOTS

For vitrification of plant root tissue, root tips were removed with a scalpel from roots submerged in cryoprotectant, either 10–30% Ficoll PM400 or n-hexadecene (Sigma-Aldrich), and placed in a 3 mm A-planchette (100–200 µm depth, Leica). To ensure proper sample enclosure, the flat side of a 3 mm B-planchette (Leica), coated with a thin layer of soy-lecithin (1 mM in chloroform), was placed on top, resulting in a planchette assembly that was subsequently subjected to HPF using a Leica EM ICE. Subsequently, the samples were recovered and the planchette assembly was disassembled with either fine tweezers or the bevel of an injection needle. The remaining A-carrier with the attached root tip was transferred into a grid box and stored in LN_2 until further use. Prior to milling, the samples were examined under the cryogenic light microscope of an ultramicrotome equipped with a cryochamber (Leica EM UC7/FC7) to verify that the root tips remained attached to the planchettes.

5.2.5 PRELIMINARY SAMPLE PROCESSING: VOLUME TRIMMING

Preliminary sample trimming was performed according to Depelteau (2022) [163]. To reduce the volume of HPF plant roots and biopsy needles containing plant tissue, samples were mounted on a grid using cryoglue (3:2; 2-propanol:100% ethanol) [163], utilizing the the cryogenic light microscope of an ultramicrotome with a cryochamber (Leica EM UC7/FC7). Subsequently, attempts were made to trim the sample volume using a cryo-trim knife (Diatome) at -160 °C. Fine-sectioning was further attempted using the cryo immuno diamond knife (Diatome). For the quality assessment of trimming, the trimmed samples were transferred to the Aquilos cryo-FIB/SEM (Thermo Fisher Scientific^{TM}), and initial milling was conducted.

5.2.6 MILLING OF PLANT PLANCHETTES, VOLUME LIFT-OUT & IMAGING

Milling, SEM imaging and lift-out procedure were performed as described in chapter 5 and according to the protocol of Schiøtz *et al.* (2024) [152]. HPF plant planchettes (type A) and a clipped half-moon grid in an autogrid were inserted into a HPF-carrier shuttle (3 mm; pretilt 35°) and subsequently transferred to the cryo-stage of a Helios Hydra V Dual-Beam cryo-PFIB (Thermo Fisher Scientific^{TM}) equipped with iFLM (development version) and a cryo-lift-out manipulator. Prior to imaging, a conductive platinum layer was sputtered onto the planchette using an integrated micro-sputter (6 min, 99 nA, xenon plasma). Subsequently, SEM images were acquired (12.5 pA; 2 kV) using MAPS (v.3.25) and aligned with the images acquired with the iFLM.

After identification of target regions, an approx. 1 µm thick platinum precursor layer was deposited over a period of 1 min using cryo-deposition with the GIS. The stage was then rotated to 180° to create an imaging face. Rough milling was performed at an angle of 16° (stage tilt 13°) using a 15 nA ion beam current, followed by polishing at 4 nA (30 kV). Trench dimensions were adjusted based on the sample and volume size, with trenches milled around the target volume, using overlapping milling patterns. The extracted volumes ranged from 20 µm x 30 µm x 10 µm (L x W x H) to 40 µm x 60 µm x 30 µm (L x W x H).

Prior to lift-out, sample integrity was assessed by SEM imaging at 90° (stage tilt 51°; 25 pA; 1 kV), followed by manual milling at 16° (tilt angle 13°; ion-beam current 0.6 nA). Subsequently, an additional 1 µm platinum layer was applied to the sample surface and the block's leading face for 4 min to mitigate beam induced damage during further milling.

The stage was configured for perpendicular milling (stage tilt: 17°; rotation: 0°), and trenches surrounding the target volume were extended to a minimum width of 10 µm.

The lift-out needle with the attached copper block, was moved adjacent to the sample to be extracted. Subsequently, the extracted chunk was attached to the copper block by re-deposition using a single-pass pattern of regular cross-sections at the interface between the copper block and the aligned sample surface [152]. The lift-out was performed at a milling angle of 9° (stage tilt: 6°).

The extracted chunk was then transferred to a half-moon grid, and the volume was aligned by matching its edge to the prepared pin edge, then attached by re-deposition using a single-pass pattern of regular cross-sections (stage tilt: 38°; milling angle: 69°; 300 pA; 30 kV). The lift-out needle was released by milling away the interface between the copper block and the volume surface. After successful lift-out and attachment to the half-moon grid, the volume and plant tissue integrity were re-evaluated with iFLM and SEM imaging, as described above.

5.3 Results

5.3.1 Application of biopsy needles

The biopsy needle was designed to obtain samples from different locations within a tissue a tissue, as well as to obtain sample of a consistent size (Fig. 5.1). To facilitate the incision into the tissue, the needle was designed with a three-pronged tip with sharp edges. Furthermore, it contained a tripartite slit located underneath the tip region, allowing for the release of compressed air, as well as providing a predetermined breaking point of the needle. This is necessary ro effectively to release the lower needle segment containing the sample for further processing. The design is described in more detail in Depelteau (2022) [163]. While the needle design provided sufficient stability for obtaining root and stem tissue samples, small air gaps appeared during application and processing, hindering optimal vitrification. To resolve this issue, the biopsy needle needed to be prefilled with a cryoprotectant such as hexadecene prior to use (Fig. 5.1).

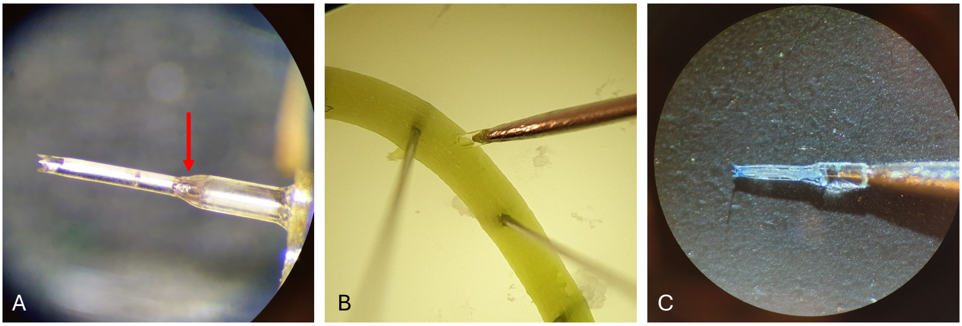

Figure 5.1: 3D-printed biopsy needle filled with cryoprotectant prior to use. The biopsy needle was designed with a three-prong tip and tripartite slits (red arrow) that serve as predetermined breaking point for segment release after sampling (A). Further details on the needle design can be found in Depelteau 2022 [163]. The stability of the biopsy needle was tested on various plant tissue types and developmental stages, including roots and stems (B). A biopsy needle containing root tissue shows small air gabs within the sample segment, which led to insufficient vitrification during high-pressure freezing (C).

During further testing of the needle for cryo-EM sample processing, the Briegel group discovered that the resin used for the 3D printed biopsy needle was not suitable for FIB/SEM or PFIB/SEM milling: the beam caused the plastic resin to melt, rendering this approach unsuitable for "in-needle milling". Consequently, its further application in this project was discontinued.

5.3.2 STAINING ENHANCES TRACEABILITY OF PLANT TISSUE

During the vitrification process of plant tissue and subsequent sample recovery, it became clear that the colourless root tissue was difficult to locate in liquid nitrogen. Additionally, visually assessing the extent to which the tissue remained attached to the planchette or grid after HPF proved challenging as well. To address this, bromothymol blue staining was initially used as tissue stain that provided the necessary contrast (Fig. 5.2). Later, this staining method was replaced with methylene blue due to its fluorescence properties. This also improved tissue traceability during the sample processing in the PFIB/SEM instruments. However, only weak fluorescence was detected with the available emission filters (L3385; L470; L565) in the PFIB/SEM.

Despite its weak fluorescence, the staining nonetheless greatly facilitated sample handling by enabling visualizing the tissue in the planchettes before the loading process into the PFIB/SEM (Fig. 5.2). Furthermore, the staining allowed precise positioning of the sample in the HPF-carrier shuttle for subsequent milling and cryo-lift-out procedures (Fig. 5.2).

The use of fluorescent staining further improved the traceability and localization of vitrified plant tissue during milling and lift-out procedures in the PFIB/SEM. Additionally, it enabled assessment of sample integrity after HPF and volume lift-out. Moreover, the iFLM in the PFIB/SEM facilitated detection of GFP-labelled endophytes within plant tissue, allowing precise section of the milling site for lamella preparation (Fig. 5.3).

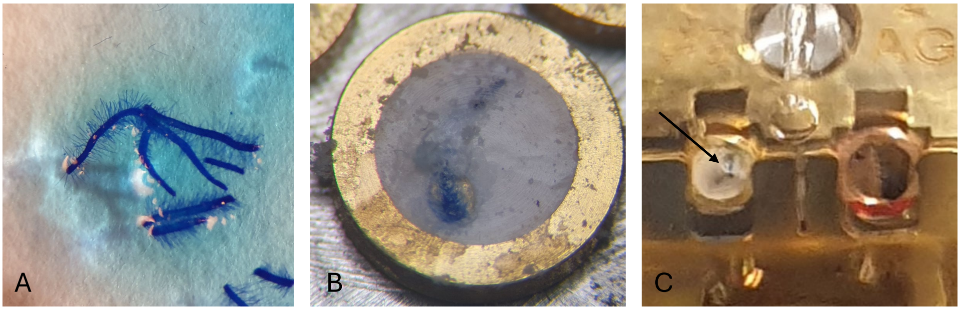

Figure 5.2: Plant roots stained with bromothymol blue (A) and methylene blue improved traceability of root samples and facilitated the assessment of root tissue presence in the planchettes after high-pressure freezing (B). Furthermore, staining assisted in the precise positioning of the root samples in the HPF-carrier shuttle, ensuring correct alignment perpendicular to the ion beam in the PFIB/SEM (C). Black arrow indicating the position of a root tissue sample within a HPF-carrier shuttle (Thermo Scientific^{TM}).

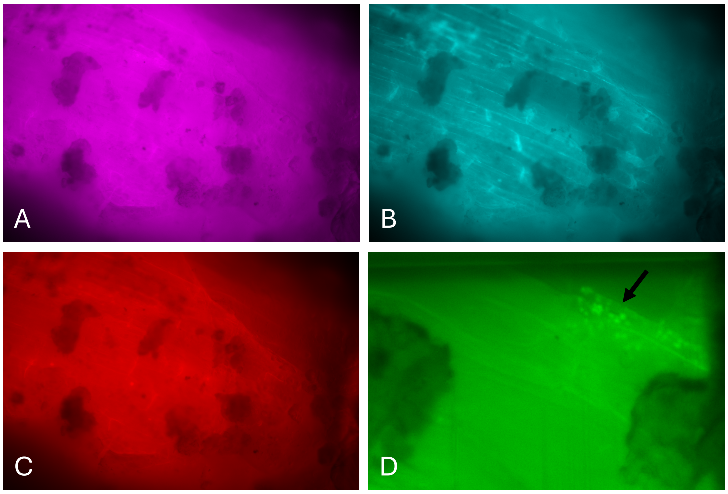

Figure 5.3: Fluorescence staining of root organ tissue using (A) methylene blue, (B) calcofluor white, and (C) Nile red. (D) GFP-labelled endophytes within root organ tissue facilitated precise milling positioning to obtain volume-samples and, later, lamellae from host-microbiota interaction areas. Images were acquired using the Helios 5 Hydra DualBeam (PFIB) with an integrated fluorescence microscope and the following emission filters: L385, L470, and L565 (Thermo Scientific$^{\text{TM}}$). The available emission filters enabled only weak detection of methylene blue fluorescence, which would yield a stronger signal with an excitation wavelength of 630 nm. However, despite the weak signal, staining still aided in the localization of the root tissue within the planchette in the PFIB/SEM. To enhance visualization, images were colour-edited in ImageJ [101].

5.3.3 INITIAL VOLUME REDUCTION

The initial plant tissue often exceeded 100 µm, significantly prolonging the milling process and increasing the risk of sample re-deposition and contamination. To mitigate this, cryo-ultramicrotomy was explored for preliminary volume reduction [163]. For this, the sample was first attached to a grid with cryo-glue [163]. Once attached, trimming was initiated. Initially, a flat surface was created as a starting point for further volume reduction. However, this process proved to be very time-intensive, and also increased the risk of de-vitrification and ice crystal contamination. After several trials, a radish root tip was successfully transferred to the Aquilos FIB/SEM, allowing for initial assessment of both volume reduction efficiency and sample integrity. In the FIB/SEM, the sample volume was only sightly reduce and exhibited numerous deep cracks. Further milling An attempts were highly time-intensive and reinforced the observation that larger sample volumes amplify re-deposition. These limitation prevented further sample processing, highlighting the need for alternative volume reduction strategies.

5.3.4 VOLUME SAMPLE PREPARATION

Achieving successful vitrification of plant tissue proved challenging due to multiple influencing factors, including vitrification conditions (e.g., choice of cryoprotectant) and the developmental stage of the root tissue. Root tissue from older seedlings (≥ 5 days) was either unsuitable or yielded poor results with existing methods. Therefore, root tissue and root tips from younger seedlings were used in further experiments. However, even in these cases, the success rate of vitrified samples remained low. This issue was further complicated

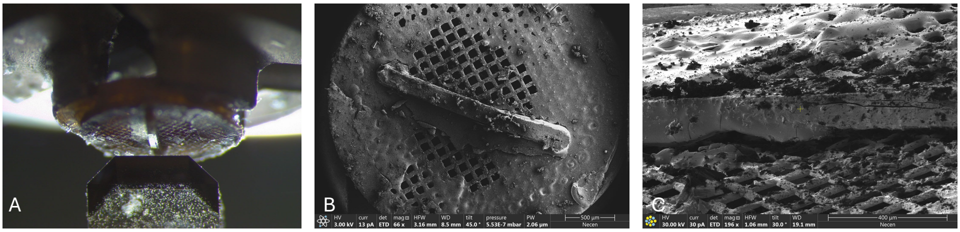

Figure 5.4: Initial trimming attempts of HPF root tissue to reduce sample volume for subsequent milling with a FIB/SEM ion-beam. (A) A HPF radish root tip was successfully attached to a grid using cryo-glue, and trimming was initiated with a diamond trim-knife in a cryo-ultramicrotome. (B) After initial trimming, the sample was transferred to a FIB/SEM (Aquilos, Thermo Scientific^{TM}) for assessment of vitrification quality and the trimming procedure. (C) During further milling with an ion-beam, significant contamination from redeposited excess material on the milled surface became apparent. Images were created in collaboration with Depelteau (2022) [163] as part of a joint study. These images were first published in Depelteau (2022) [163] and are included here with permission.

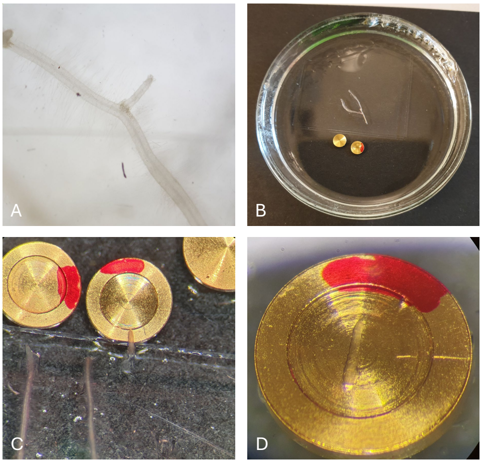

Figure 5.5: Optimized workflow for cryo-EM large-volume sample preparation using root organ tissue. (A) Root organs grow on media plates without requiring light or soil, offering the advantage that multiple root tips and lateral roots can be harvested a single plate. Additionally, root organs are thinner than young seedling roots, reducing the need for extensive volume-reduction steps such as sectioning prior to HPF. (B, C) Preparation of root organs for HPF, including planchette sandwich assembly while submerged in cryoprotectant (hexadecene). (C) Small root samples were cut while submerged in cryoprotectant at the edge of a glass slide, ensuring direct transfer into the prepared A-planchette. (D) Positioning of the root sample prior to planchette assembly and HPF. A red mark on the planchette edge facilitated sample-side identification after HPF and during downstream processing.

by the fact that poor vitrification quality only became evident during (P)FIB/SEM analysis, when tissue damage caused by HPF was observed. Partially vitrified tissue was used for initial milling trials in the PFIB/SEM. Despite the presence of numerous artefacts in the tissue, imaging provided the first structural insights into vitrified plant cells within the epidermis of the root.

The use of root organ tissue and root tips led to a notable improvement in vitrification success. Compared to younger seedling roots; root organs thinner, easier to maintain on plates without requiring light or soil and allow for the collection of multiple root tips from a single plate. Additional improvements in vitrification success were achieved by cutting the root tissue and assembling the HPF planchette sandwich while submerged in cryoprotectant, ensuring better preservation during freezing (Fig. 5.5). Furthermore, the HPF-carrier shuttle enabled the direct use of samples frozen onto planchettes, eliminating the need for sample transfer onto a grid or cryoglue. This reduction in manual handling minimized the risk of de-vitrification and ice crystal contamination. Additionally, the integration of the PFIB/SEM with a cryo-lift-out manipulator eliminated the need for volume trimming via cryo-ultramicrotomy, significantly reducing manual handling time and the associated risks.

The cryo-lift-out procedure was successfully performed on root tissue, allowing volume samples to be extracted extracted from different regions of the vitrified root, including deeper layers such as the root canal system. While most methods primarily enable sampling from outer root layers, this approach facilitated the extraction of vitrified volume samples from both the epidermis and the inner root tissue, demonstrating successful vitrification deep within the root structure. Furthermore, initial SEM images were obtained of HPF root tissue during the milling process, providing insight into both, vitrification quality and sample integrity. Samples processed using the optimized workflow demonstrated promising vitrification quality and high sample integrity. As a result, following successful cryo-lift-out and integrity confirmation, lamella preparation for cryo-EM imaging was initiated. Although only a small number of lamellae were successfully obtained, most were unsuitable for cryo-EM imaging due to ice crystal contamination during transfer. However, intensive milling induced partial de-vitrification in some samples, highlighting the need for refinements to minimize de-vitrification and re-deposition during the milling process. This study provides the first high-resolution structural insights into vitrified root tissue, revealing successful vitrification from the outer epidermis to the root canal system in unprecedented detail. These findings pave the way for more advanced investigations of plant tissue vitrification and cryo-EM sample preparation.

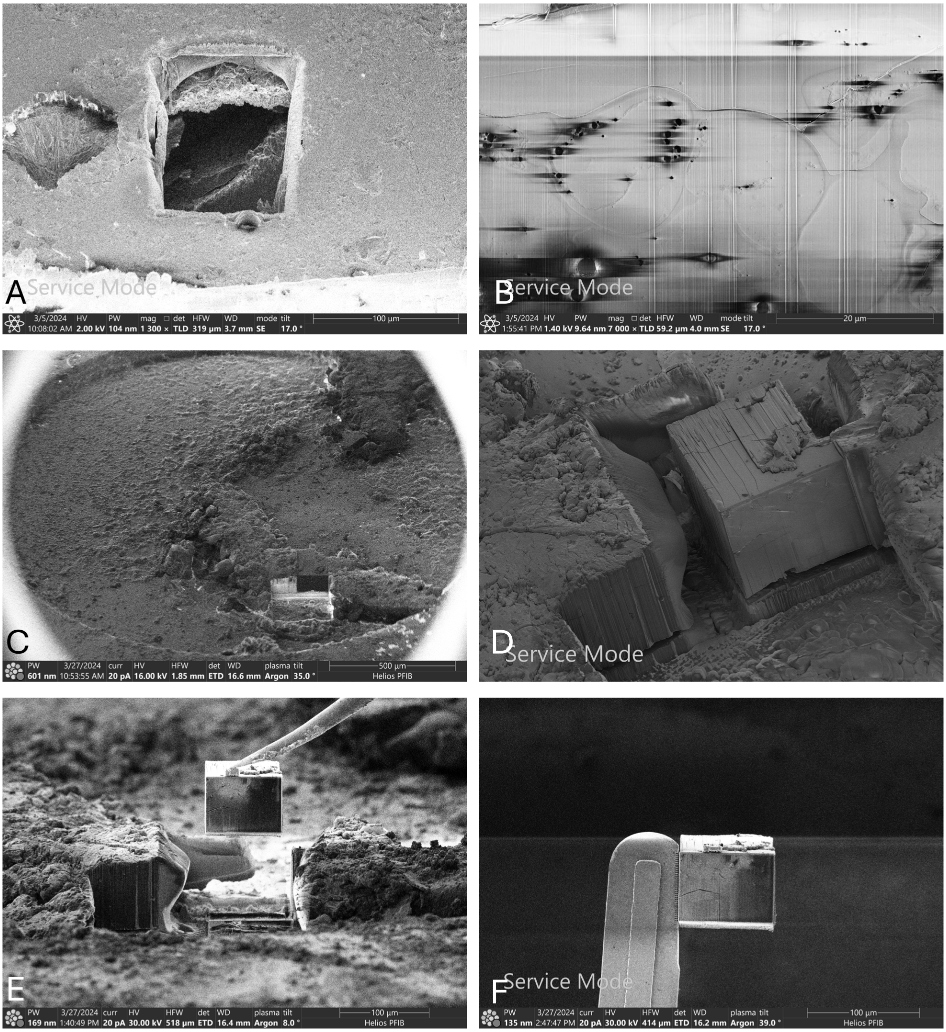

Figure 5.6: Evaluation of sample vitrification quality and cryo-lift-out workflow in PFIB/SEM. (A, B) Assessment of vitrification quality in seedling root samples. (A) Vitrification quality of seedling root samples was often poor, showing extensive structural damage, including imploded tissue. (B) Only the outermost cell layers (epidermis) of the root tissue achieved vitrification, exhibit better structural integrity. However, HPF artefacts persisted, preventing further processing. (C–F) Cryo-lift-out workflow using an improved sample preparation approach on tissue of root organs. (C) Localization of HPF root tissue without staining was difficult and surface features served as key orientation markers. (D) Once a potential target area of interest was identified, trench milling around the target region was initiated. (E) Following trench milling, the volume sample was attached to the lift-out needle, with a copper block as an intermediary for improved attachment. (F) The volume sample was then transferred to a half-moon grid and mounted to a pin for downstream processing, including volume imaging and lamella preparation for cryo-EM analysis.

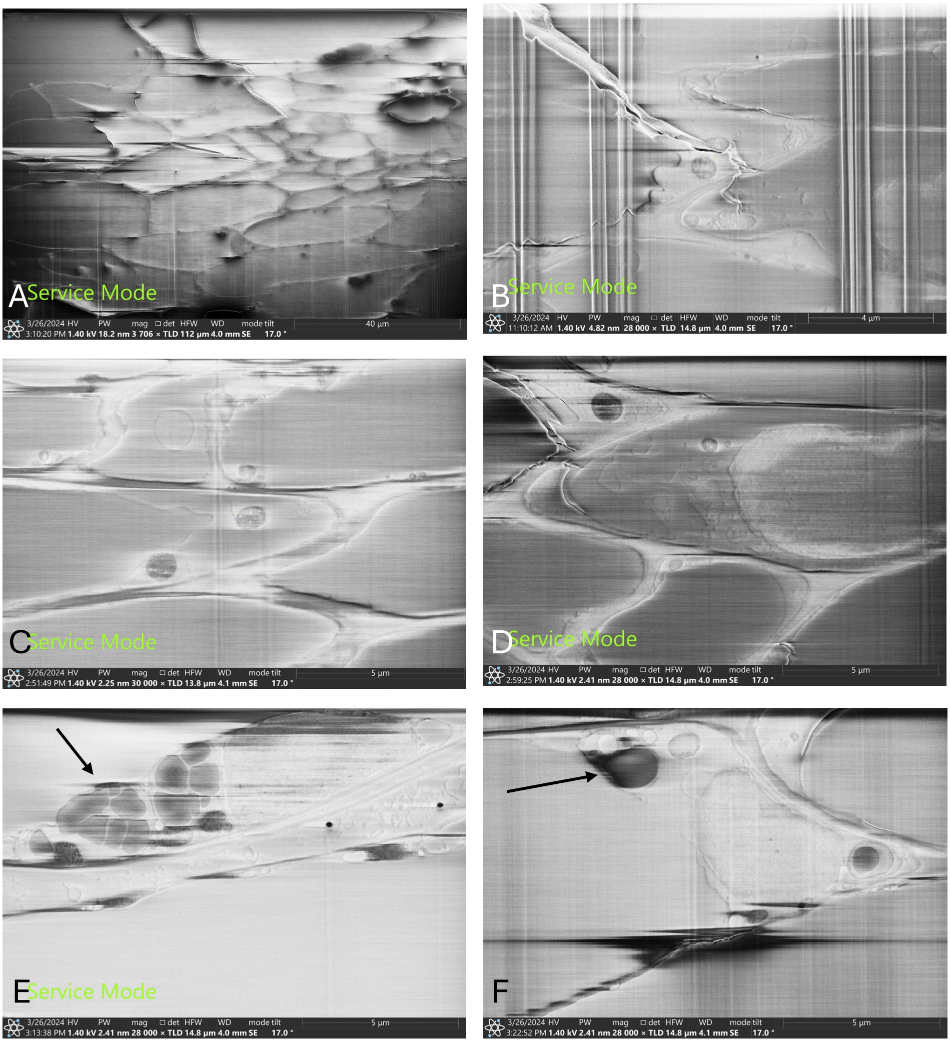

Figure 5.7: PFIB/SEM images of root organs with promising vitrification quality and high structural integrity. (A) Promising vitrification quality was achieved throughout the root tissue, ranging from the outer epidermal layer to the root canal system at the centre of the root. (B–F) The improved sample preparation procedure led to enhance vitrification, preserving structural integrity and providing the first high-resolution insight of vitrified plant cells and their ultrastructure. (E–F) Arbuscular mycorrhizal fungi within root organ tissue (black arrow) were successfully visualized, demonstrating the potential of the vitrification workflow for studying plant-microbe interactions at the ultrastructural level.

5.4 Discussion

To understand the interactions between plants and their microbiome, we need to investigate plant tissue samples at the nanoscale. To accomplish this, cryo-ET is the method of choice, as it allows imaging of near-native samples, in three dimensions and at macromolecular resolution. However, the workflows that enable the processing of such large-volume samples are still in its infancy and have only been successfully applied to a small set of biological samples. Here we aim to develop a robust workflow allowing to produce lamellae for cryo-EM imaging and cryo-ET data collection from native plant tissue samples. In our initial attempts, we employed 3D-printed biopsy needles, which enabled to consistently retrieved tissue of uniform size from various locations and tissue types. However, the resin used in the 3D-printed needles proved incompatible with further processing by FIB/SEM or PFIB/SEM. Nonetheless, the concept and design of these biopsy needles remain promising for future LV sample preparation. In future work, alternative resin types or novel materials should be explored for compatibility with (P)FIB/SEM processing.

Previous studies have demonstrated that one of the biggest hurdles and bottlenecks in analysing the ultrastructure of plants using cryo-EM is the vitrification of plant tissue. Vitrification by plunge freezing is limited to samples of ≥10 µm and has been successfully applied to algae and epidermal layers that can be directly applied onto a grid [157, 165, 166]. In contrast, the literature and protocols for vitrification of higher plant tissue are limited to the root tips of young Arabidopsis seedlings, which are less than ≥100 µm thick [165]. Samples exceeding 10 µm in thickness require HPF during which the sample is rapidly subjected under pressure (approximately 2100 bar) to liquid nitrogen. The application of high pressure during the cooling prevents sample expansion, an therefore, the nucleation of crystalline ice, and ideally, the sample is fixed in vitreous ice. Notably, the postulated limit for sample thickness at which vitrification can still be achieved by HPF is approximately 500 nm [158]. Yet to date only samples with a maximum thickness of 200 µm have been successfully vitrified by HPF [16, 50, 165]. This success is often dependent on the use and type of cryo-protectants, which significantly influence vitrification efficiency. Thus, the discrepancy between the postulated maximum sample thickness and the thickness actually achieved during vitrification can be attributed both to the inherent properties of the samples tissue and to the sample handling as well as freezing conditions. To improve vitrification outcomes, we applied modifications to the planchettes suggested in the literature [150].Prior to this modification, the planchette sandwich disassembly and recovery of vitrified sample were challenging, tedious, and occasionally lead to sample loss. By polishing and coating the flat side of B-planchettes with soy-lecithin, we improved the success of disassembly after HPF, which significantly enhanced sample recovery. Using this approach, we successfully vitrified root tips and root tissues with a sample thickness between 100–200 µm.

In parallel, cryoprotectants are used during planchette assembly to suppress ice formation. While agents such as sucrose and trehalose are common, their viscosity and electron density can introduce imaging artefacts. Alternatives like yeast paste, Ficoll, 2-methylpentane, proline, and hexadecene have been described [50, 166]. Among these, hexadecene proved particularly effective for plant tissue, likely due to improved tissue penetration. However, it increases stiffness after vitrification and complicates disassembly when combined with PBS (phosphate-buffered saline).

Furthermore, recent advancements in cryo-lift out now enable the use of planchettes for PFIB/SEM, thereby simplifying cryo-EM sample preparation. With this advancement, samples vitrified in planchettes can be directly transferred into the PFIB/SEM for milling, circumventing the tedious, low-yield process of recovering the vitrified sample for grid mounting via cryoglue [163]. This innovation also eliminates the need for sample trimming by the ultramicrotome, a demanding procedure prone to cutting artefacts and requiring substantial expertise [157]. In our study, we observed that as the sample volume increases, both the milling time and the risk of re-deposition of milled particles onto the milling area increases, too. In addition, prolonged milling time further increases the likelihood of beam damage, which necessitates the application of a conductive layer to create a smooth milling surface. The success rate improved significantly by switching from FIB/SEM to a PFIB/SEM system with an integrated lift-out manipulator. Not only did the PFIB/SEM system reduce the necessary milling time, but it also enabled the extraction of volumes from the LV sample that could be transferred to a new grid for further lamella preparation. Consequently, this approach minimized the volume of surrounding material and reduced the risk of re-deposition onto the milled area. However, re-deposition induced contamination could not be entirely avoided, leading to loss of lamellae. Additionally, the beam sensitivity also varies within sample such as the presence of fibres (e.g. lignin), which necessitates beam intensity adjustments during milling procedures [157].

Besides the common challenges of processing LV biological samples, plant tissue presents its own inherent obstacles for cryo-EM sample preparation. The variable tissue stiffness resulting from differing degrees of lignification depending on the developmental stage complicates pre-sectioning and the obtaining of samples with consistent size and volume. Moreover, unlike metazoan cells, plant cells possess an additional cell wall. This cell wall is a rigid structure, primarily determined by its cellulose content. It is composed mainly of chemical diverse polysaccharides, including cellulose, hemicellulose, and pectins. The cell wall serves as the first line of defence against intruders, and regulates molecular movement through a wide range of receptors, pores, and channels [167]. Despite its rigidity, the cell wall allows adaptation to different environmental conditions. In addition, intracellular compartments such as vacuoles, as well as tissue compartments like the xylem sap, exhibit chemical diversity that varies with environmental conditions and the developmental stage of the plant. This diversity combined with the barrier imposed by the cell wall, complicates the uniform diffusion of fixatives and cryoprotectants, leading to extended incubation times. Ideally, incubation times are kept short to avoid the adverse effects of cryoprotectants, which can exhibit toxicity or induce osmotic pressure, thereby causing artefacts.

The chemical diversity of plant tissue also affects the thermodynamic freezing point, which can differ between the cell contents and the surrounding intercellular matrix. Moreover, variations in turgor pressure within different cell compartments, particularly in the vacuole, which can constitute up to 90 % of the cell volume – present additional challenges during HPF. As a result, younger root tissue with less developed and less chemical diverse vacuoles, or plant cells with minimal vacuole development, are preferred for optimal vitrification. A significant issue in making plant tissue accessible for cryo-EM imaging is the presence of gases within the tissue matrix, both between cells and within the xylem sap. The presence of gases during vitrification result in incomplete vitrification and tissue rupture due to implosion. Therefore, minimizing or avoiding the formation of gas bubbles and the presence of gases within the tissue is essential. This can be achieved by using cryoprotectants and reducing air exposure during plant root cultivation.

Root organs a suitable model system for LV cryo-EM of plant tissue

Root organs are well-established model systems for the investigation of host–microbiota interactions, in particular with arbuscular mycorrhizal fungi. Further root organs can be sourced from other agricultural important plants, broadening the scope for studying various microbiota members. The use of root organs, cultivated in media plates with the roots submerged, and without the need of light, helps preventing photosynthesis and potentially reducing the presence of gases within the tissue. When combined with HPF sample preparation under hexadecene — with both sample handling and planchette assembly conducted in a hexadecene-filled dish — these adjustments increased the likelihood of obtaining vitrified root tissue. Moreover, controlled and reproducible growth conditions enable the harvesting of root tissue with consistent chemical and physical properties, facilitating the development of standardized sample preparation protocols. In addition, the roots are thin and multiple root tips can be harvested from a single plate. Furthermore, using root organs permits rapid handling during pre-sectioning to obtain HPF suitable sample sizes while minimizing the risk of drying out prior to HPF.

The initial cryo-SEM imaging of vitrified plant tissue achieved in this study is a promising advancement, enhancing the potential for ultrastructural investigations of host-microbiota interactions. Nevertheless, the workflow is currently limited by low sample throughput and requires significant expertise, underscoring the need for further improvements to streamline the process. Furthermore, the presence of either single strains or a complex microbiota can alter the chemical and physical composition of the sample, potentially necessitating additional protocol adjustments.

Overall, the improvements in sample preparation, including modification in planchette assembly combined with recent advancements such as PFIB/SEM with iFLM and a cryo-lift out manipulator demonstrated in this study not only the success rate of root tissue vitrification but also enhanced the likelihood of obtaining lamellae suitable for cryo-EM. Furthermore, the use of root organs led to a significant improvement in both vitrification quality and sample throughput. These promising advancements indicate that current challenges will soon be overcome opening a new window into the ultrastructure of plant tissue and the structural interactions between plants and their microbiota.

Acknowledgements

J.L. was supported by the OCENW.GROOT.2019.063 and Building Blocks of Life 737.016.00 grants from the Netherlands Organization for Scientific Research (NWO), both awarded to A.B. This work benefited from access to the Electron Microscopy facility in Brno, Czech Republic, an Instruct-ERIC centre. Financial support was provided by Instruct-ERIC (PID: 27640) as well as through the Instruct-ERIC Internship Call (APPID: 3188). We also gratefully acknowledge the CF CEITEC/Brno – Cryo-electron Microscopy and Tomography facility of CIISB, Instruct-CZ Centre, supported by MEYS CR (LM2023042) and the European Regional Development Fund – Project „Innovation of Czech Infrastructure for Integrative Structural Biology“ (No. CZ.02.01.01/00/23_015/0008175). We thank Jamie Depelteau (Leiden University) for initiating the development of the 3D-printed biopsy needle and for the opportunity to contribute to its design and implementation. Sandra Richter (University of Tübingen) provided early advice on vitrification of plant tissue using high-pressure freezing. The GFP-labelled *F. anhuiense* strain was provided by Salma Balazadeh and Arezoo Rahimi (Leiden University), and cultures were prepared and shipped by Sofia Stiegert (Leiden University).

Author Contributions

J.L. developed the large-volume cryo-EM workflow for plant root samples. J.L. prepared all samples, performed vitrification, operated the cryo-PFIB/SEM system with J.M. and P.K., and wrote the manuscript. J.M. and P.K. provided training and technical support at CEITEC, performed lamella preparation, lift-out procedures and cryo-EM data acquisition, and contributed to the PFIB/SEM methods. After J.L.'s research visit, J.M. and P.K. continued working on the samples to obtain cryo-EM data. M.v.S. prepared and shipped the (Ri) T-DNA transformed root organ plates and provided additional material. J.N. provided technical advice. T.K. supervised the Amsterdam component and enabled access to the root organ system. A.B. supervised the project and provided feedback on the manuscript.

6

Distribution of temperate bacteriophages among endophytic Bacteroidota and their relevance

Members of the phylum Bacteroidota play a key role in diverse microbiota and influence the health and resilience of their hosts and their associated microbial communities. Due to their often-unique metabolic capabilities and mutualistic behaviour, they are being investigated as alternative treatments to improve plant resistance in agriculture and soil remediation. Recent studies suggest that some of these beneficial traits may be linked to the presence of phage-derived genetic elements within the bacterial genome. Understanding how prophages influence their behaviour, competitiveness and interactions within the plant-associated microbiota is essential for their effective and sustainable application.

In this study, we explored the distribution and inducibility of prophages in selected endophytic members of the phylum Bacteroidota. The resulting extracts were tested for lytic activity, and their host spectrum was assessed. In several cases, phage-like particles were visualised using transmission electron microscopy. The observed lytic activity and visualisation of phage-like particles indicate the presence of inducible prophages in endophytic Bacteroidota. These findings support the need for further investigation into prophage activity in endophytic Bacteroidota and may contribute to a better understanding of their role in the plant-associated microbiota.

This chapter is based on **Liedtke, J.**, Martina, I.N., Posthuma, K., and Briegel, A.: Distribution of temperate bacteriophages among endophytic Bacteroidota and their relevance, in preparation.

6.1 INTRODUCTION

The phylum Bacteroidota is one of the dominant phyla in various microbial communities, known as microbiota, including soil and plant microbiota [8]. This dominance is largely due to their ability to degrade complex organic compounds. With a few exceptions, they exhibit predominantly mutualistic behaviour, contributing to both the health of their host (plant) and the surrounding microbiota [8]. In addition, previous studies have shown that the endophytic members *Flavobacterium anhuiense* and *Chitinophaga pinensis*, which can colonize and reside in plant tissue, significantly improve the plant's resilience [85]. These properties make them promising candidates for the development of sustainable and environmentally friendly treatments in agriculture as alternatives to pesticides and antibiotics.

In addition to their beneficial traits, these bacteria display intriguing adaptive responses under certain conditions that remain poorly understood. One such response is the pronounced morphological plasticity observed in *C. pinensis* (Chapter 3) and *F. anhuiense* (unpublished). In both cases, cells transition from several micrometer long filamentous cells to markedly smaller morphotypes of less than 1 µm. The underlying triggers of these repeated transitions remain to be elucidated (Chapter 3). These phenotypic changes may influence bacterial interactions within the microbiota. To fully harness their potential for sustainable agricultural applications, it is crucial to understand how these bacteria interact with the plant microbiota in response to such changes.

Microbiota are multi-species associations where interactions occur at different levels (species, population, individuals) with competitive, supportive, facilitative, or suppressive dynamics. These interactions can change over time or in response to environmental conditions. Microbiota also include viruses that target bacteria, known as phages (bacteriophages), which play a key role in microbiota diversity. According to the 'kill the winner'theory [9], phages target bacteria that thrive under certain conditions. As a consequence they prevent the overgrowth of a single species, thereby shaping the microbiota composition, maintaining its diversity, and ensuring its long-term persistence. Although phages can exert strong selective pressure on bacterial populations, bacteria have developed adaptive strategies to evade infection. Among these, morphological changes that reduce or eliminate phage-binding proteins on the cell surface have been proposed as a potential escape mechanism [168, 169].

This theory applies to phages in the lytic replication cycle, which hijack the host's replication system to predominantly produce phage particles, released after assembly through cell lysis. In contrast, some phages integrate their genome into that of their host, entering the lysogenic replication cycle. Their sequence remains dormant as a prophage and is replicated together with the host until a trigger induces the switch to the lytic cycle. Prophages are not necessarily disadvantageous to the host. Under certain conditions they can benefit the host by conferring additional metabolic capabilities [10, 170], resistance traits [11] or morphological changes [12] that provide a competitive advantage within the community. Nonetheless, prophage induction has also been associated with host stress responses. For instance, host cell filamentation has been identified as part of an SOS response triggered by prophage induction [171]. Notably, filamentous cells are more susceptible to phage infection compared to smaller cell sizes [12].

Prophages are widespread among bacterial genomes and may contribute to enhanced microbiota resilience and the stabilisation of microbial community dynamics under stressful environmental conditions. Whether such elements are also present in endophytic Bacteroidota and potentially contribute to traits relevant for their lifestyle has not been systematically investigated.

In this study, we explored prophage distribution in endophytic members of the Bacteroidota, including representatives of the classes: Chitinophagia, Sphingobacteriia, Cytophagia and Flavobacteriia. We also examined whether the observed morphological changes in *C. pinensis* and *F. anhuiense* may be linked to the presence or inducibility of prophages.

6.2 MATERIAL & METHODS

6.2.1 BACTERIAL STRAINS AND CULTURE CONDITIONS

The following bacterial strains of the phylum Bacteroidota were used for prophage induction and isolation, selected on the basis of prophage prediction: *Flavobacterium anhuiense* (98) [85], *Chitinophaga pinensis* (94) wild-type [85], *Chitinophaga pinensis* lab-strain (DSM 2588), and *Runella defluvii* (DSM 17976). These strains were grown in 0.1x TSB at 25 °C. The following strains *Chitinophaga jiangningensis* (DSM 27406), *Chitinophaga niabensis* (DSM 24787), *Dyadobacter endophyticus* (DSM 100786), *Flavobacterium johnsoniae subsp. johnsoniae* (DSM 2064), *Mucilaginibacter auburnensis* (DSM 28175), *Niabella soli* (DSM 19437), and *Solitalea koreensis* (DSM 21342) were grown in LB at 28 °C. Strains were cultured overnight in liquid media at their respective temperatures and 200 rpm. Additionally, a *Flavobacterium* sp. strain, obtained from a collaborator's strain collection (B. Ford; Utrecht University), was included. The strain was not further characterized but is known to belong to the genus *Flavobacterium.* Although its genome sequence was unavailable for prophage prediction, it was included in the induction assays and lytic activity screening to assess potential susceptibility. This strain was cultured in 0.1x TSB at 25 °C, under the same conditions as for *F. anhuiense.*

6.2.2 PREDICTION OF PROPHAGE ELEMENTS

The web-based tools Prophage-Hunter [172] and PHASTER [173–175] were used to identify prophage regions and assess their predicted completeness (classified as active, ambiguous, or inactive). Genome sequences were obtained from NCBI GenBank, except for *Chitinophaga pinensis* (94) and *Flavobacterium anhuiense* (98), which were obtained from Carrión (2019) [85].

6.2.3 PROHAGE INDUCTION ASSAYS

INDUCTION WITH MITOMYCIN C

Prophage induction using mitomycin C (final concentrations: 1.5 and 2.5 mM) was performed in overnight cultures incubated at strain specific temperature and 250 rpm. Optical density at 600 nm (OD_{600}) was monitored, and samples were collected every 2 h during the first 6 h, and at 24 h and 48 h. All samples were filtered through 0.22 μm filters and stored at 4 °C.

INDUCTION WITH UV-LIGHT

Overnight cultures (5 ml) were transferred to sterile petri dishes (Ø 9 cm) and placed without a lid at a distance of 15 cm from the UV-light source (6W Germicidal light T5 Tube UVC sterilizer, Lcamaw via Aliexpress.nl). Samples were collected after 1, 4, 10, and 20 min of exposure and briefly cooled on ice. Each sample was divided equally. One part was filtered (0.22 µm) and stored as described above. The other part was added to inoculate an equal volume of media and incubated under strain specific conditions to obtain potentially phage-free strains.

Unless stated otherwise, all filtered samples obtained from these assays are hereafter referred to as extracts.

6.2.4 SCREENING FOR LYTIC PHAGE ACTIVITY

All extracts obtained from induction assays were screened for lytic activity using plaque assay techniques, which were also used for isolation and purification.

PREPARATION OF DOUBLE-OVERLAY PLATES

For double-overlay plates (21 cm x 21 cm), the basal agar layers were prepared with 1.5% (w/v) agar using strain-specific growth medium. The strain suspensions for the top agar layer were obtained from overnight cultures, centrifuged (3,000x g; 5 min) and the cell pellet resuspended in phage buffer to an OD_{600} of 0.1. Subsequently, 1 ml of each strain suspension was combined with 11 ml of liquefied medium containing 0.5% (w/v) low-melting-point agar, stored at 45 °C. Shortly before pouring over the basal agar layer, 12 µl of 5 M $CaCl_2$ was added. Once the top agar was solidified, the plates were ready for the plaque assays.

LYTIC ACTIVITY SCREENING AND HOST RANGE DETERMINATION

Extract from induction assays were screened for lytic activity using spot assays in which 3 µl extract was spotted in triplicates onto double-overlay plates. This approach avoids dilution of the potential phage concentration and increases the probability of observing plaques. After diffusion, the plates were incubated at the respective optimal temperature for each strain and observed daily for two weeks.

Plates displaying visible plaques were subsequently used for phage isolation and purification. Individual plaques were sampled using sterile toothpicks or sterile cotton swabs, which were moistened with phage buffer prior use. These were streaked onto double-overlay plates prepared with the respective host strain. The plates were incubated and observed daily for up to two weeks, with smaller plaques used for further rounds of purification. Furthermore, a dilution series (10^0 to 10^{-5}) of the extracts showing lytic activity was prepared in phage buffer, and each dilution step was tested in triplicate, resulting in countable small plaques [176].

In addition, extracts and concentrates were tested for lytic activity against the aforementioned strains using the double-overlay assay. This method was used to determine the host range of the extracts, based on the formation of plaques and changes in colony morphology.

Concentrate potential phage particles and size segregation

To concentrate potential phage particles and facilitate imaging by TEM, the extracts were subjected to filtration using different pore sizes and precipitation. For filtration, 400 µl of the extract was transferred to microcentrifuge filters (AmiconUltra; - 100 K; 100,000 NMWL; Ultracel ®; Merck Milipore Ltd; Cork; IE) and centrifuged (1,500x g; 30 min). The remaining volume in the filter, assumed to contain concentrated phage particles, was transferred to a new tube (1.5 ml) and stored at 4 °C. The filtrates were further treated with smaller pore size filters (AmiconUltra; Ultra -15; Ultracel ® - 10K; 10,000 NMWL; Merck Milipore Ltd; Cork; IE) and centrifuged (5,000x g; 10 min; 4 °C), resulting in further concentration of potential smaller phages and removal of cell debris. The final concentrates were tested for lytic activity as previously described. The plaque forming concentrates were used for phage isolation, purification and TEM analysis. As a concentration method, PEG-based precipitation was applied using a modified protocol from Ambros *et al.* (2023). In this procedure, 900 µl of extract was supplemented with 300 µl of 20% (w/v) PEG8,000 (final concentration: 4%; Sigma-Aldrich) and 300 µl of 2.5 M NaCl (final concentration: ~3%), followed by incubation on ice for at least 1 h. Subsequently, the samples were centrifuged (13,000x g; 10 min; 4 °C) and the resulting pellet was resuspended in phage buffer at 10% of the originally used sample volume. Tests were repeated without NaCl and with PEG6,000 (Sigma-Aldrich) to account for potential sensitivity of phage particles to high salt concentration or PEG type. Concentrates were screened for lytic phage activity, with plaque-forming samples subjected to further isolation, purification, and TEM imaging.

6.2.5 Transmission electron microscopy

All extracts and concentrates were screened for the presence of phage particles and imaged using TEM (Talos L120c; 120 kV; Thermo Ficher Scientific). For this purpose, 3 µl of each sample were incubated for 30 sec. on a glow-discharged carbon coated grid (CF200-CU-50; Electron microscopy science). Excess liquid was removed and the remaining sample on the grid negatively stained with 4% (w/v) uranyl acetate for 30 sec. Initially, imaging was performed without gold beads. However, to facilitate focusing and ease imaging, a 1/25 dilution of 10-nm colloidal gold solution treated with protein A (Cell Microscopy Core, Utrecht University, Utrecht, The Netherlands) was added to the sample prior to negative staining.

6.3 Results

6.3.1 Detection of active prophages regions among Bacteroidota strains

To investigate the presence of prophages within the phylum Bacteroidota, a selection of strains relevant to plant-associated habitats, were analysed. Genomic sequences of these strains were retrieved from the NCBI database and screened for the presence of prophage sequences within the bacterial genome using the web-based tools Prophage-hunter and PHASTER. The results were categorized based on sequence completeness scores, with classifications into active, ambiguous, and inactive prophages. The outcome of the prophage prediction is summarized in table 6.1.

Table 6.1: Summary of prophage predictions for 13 Bacteroidota strains, using the Prophage-hunter tool [172]. Genomic data were retrieved from the NCBI database and screened for the presence of prophage regions, which were categorized as active, ambiguous or inactive based on completeness scores. Sequences of the wild-type strains *Chitinophaga pinensis* (94) and *Flavobacterium anhuiense* (98) were obtained from Carrión (2019) [85].

Class	**Name**	**Strain no.**	**Predicted**	**Inactive**	**Ambiguous**	**Active**
Chitinophagia	*C. niabensis*	DSM24787	126	120	3	3
	C. pinensis	DSM2588	131	128	4	3
	C. jiangningensis	DSM27406	171	162	6	3
	N. soli	DSM19437	79	70	8	1
	C. pinensis (94)*	–	110	99	7	4
Sphingobacteriia	*S. koreensis*	DSM21342	111	108	2	1
	M. auburnensis	DSM28175	79	78	1	0
Cytophagia	*R. defluvii*	DSM17976	238	217	9	10
	D. endophyticus	DSM100786	170	155	12	3
Flavobacteriia	*F. johnsoniae*	DSM2064	178	148	25	5
	F. anhuiense (98)*	–	101	87	12	2
Bacteroidia	*A. hydrogenigenes*	DSM24657	115	110	3	2

* wild-type strains; internal identifiers (94) and (98) as used by Carrión et al. [85]

While PHASTER detected a single, previously described prophage (FpV-21) in *Flavobacterium johnsoniae* [177], Prophage-hunter idetified identified substantially more prophage sequences across a broader range of strains (Tab. 6.1). Among the selected strains, *Runella defluvii* had the highest number of predicted prophages sequences, with a total of 238, of which 10 were classified as active (Tab. 6.1). Whereas in *Mucilaginibacter auburnensis*, a total of 79 sequences were found, of which only one was ambiguous and none were classified as active (Tab. 6.1). Despite these predictions, *M. auburnensis* was nevertheless included in the further investigation, as a potentially susceptible strain that could support phage proliferation and enrichment.

Following induction, all 12 selected strains produced extracts with detectable lytic activity. Differences were observed in the timing at which these extracts led to plaque formation. In some cases, lytic activity was detectable as early as 2 h post-induction, while in others, plaque formation appeared 6 h after induction. In all cases, lytic activity was detectable within 24 h post-induction. In addition, induction with UV-light resulted in larger plaques compared to the mitomycin C induced samples.

To quantify the potential phage concentration in the extracts with lytic activity, a dilution series was performed. With each dilution step, lytic activity gradually decreased with plaque signals fading below the threshold of reliable detection (Fig. 6.1B). Therefore, extracts were subsequently concentrated, which led to more distinct plaque formation. Nevertheless, the concentration of lytic particles remained below the quantification limit under standard assay conditions. During the experiment, we also observed the formation of "white plaques" (Fig. 6.1C). These were not considered to be indicators of lytic infection, as they lacked complete cell lysis and distinct plaque formation. In four of the 12 extracts, plaque formation was observed on the respective strain of origin. *Chitinophaga pinensis* (DSM 2588), *M. auburnensis*, *R. defluvii*, and *Flavobacterium anhuiense* indicating that these strains were susceptible to reinfection.

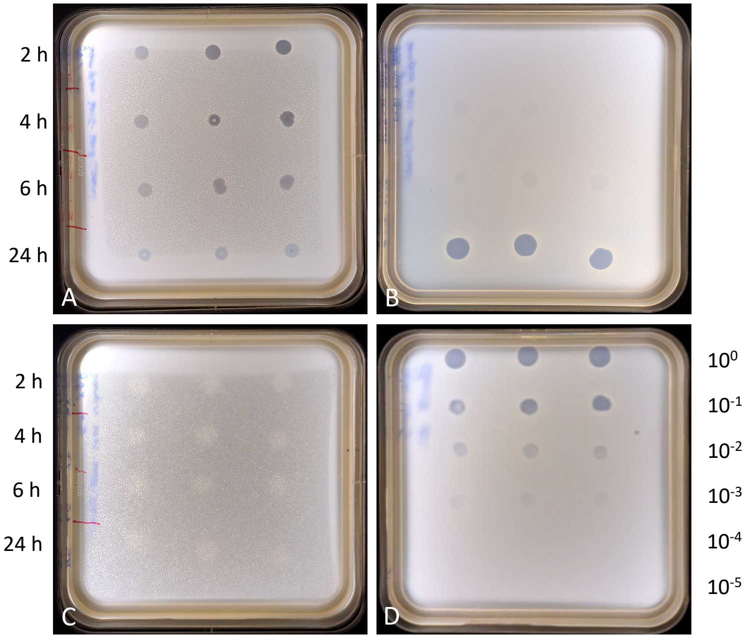

Figure 6.1: Plaque assays: Plaque formation after 2, 4, 6 and 24 h (A–C) with the appearance of bull's eye colonies (A), an increase of lytic activity over time after induction with mitomycin C (B), and the appearance of "white plaques" (C). The latter were considered as negative for plaque formation, as they did not lead to full cell lysis and formation of clear plaques. A dilution series (10^0 to 10^{-5}) of extract was performed to determine potential phage concentration. However, plaques gradually faded without forming smaller, countable plaques (D). (A) *Flavobacterium anhuiense* (98) infected with P10 derived from *Flavobacterium johnsoniae*. (B + D) *Chitinophaga pinensis* (94) infected with P3 derived from *Chitinophaga jiangningensis*. (C) *F. anhuiense* (98) infected with P12 derived from *Flavobacterium* sp.

6.3.2 Host range of extracts with lytic activity

In the following, the extracts derived from the 12 different host strains are referred to as "the 12 extracts (P1–P12)" for better understanding (Tab. 6.2). The host-range assay revealed that all extracts (P1–P12) led to plaque formation when tested with susceptible strains (Tab. 6.2). The most susceptible strain was the lab strain *C. pinensis* (DSM 2588), which was susceptible to 11 extracts, followed by *M. auburnensis*, with susceptibility to 9, and *R. defluvii*, with susceptibility to 8 of the 12 extracts (Tab. 6.2). Of the 12 tested strains, 5 were susceptible to only one extract, which was derived either from *Chitinophaga niabensis* (P1) or *C. jiangningensis* (P3). The extract (P12) from *Flavobacterium* sp. showed lytic activity exclusively against *F. johnsoniae*. The remaining extracts (P1–P11) displayed lytic activity against 3 to 5 different strains.

6.3.3 TEM-based identification of phage-like structures

To confirm the presence of phages in the extracts and to determine their morphology, all extracts were analysed by negative staining and TEM. In three out of 12 extracts, assembled phages and phage like components such as capsids, tail fibres, and sheaths were observed. Phage-particle concentration appeared low, across the analysed samples,

Table 6.2: Host range of extracts. Summary of lytic activity screening performed against the strains used in the prophage induction assays. The extracts (P1–P12) were obtained from the strains listed in the left column by prophage induction assays, where P1 correspond to the first strain (*Chitinophaga niabensis*), P2 to the second (*Chitinophaga pinensis*), and so on. Each extract was first tested against its strain of origin and then against all other strains to determine host specificity.

Class	**Strain**	P1	P2	P3	P4	P5	P6	P7	P8	P9	P10	P11	P12
Chitinophagia	*C. niabensis*	−	−	+	−	−	−	−	−	−	−	−	−
	C. pinensis	+	+	+	+	+	+	+	+	+	+	+	−
	C. jiangningensis	+	−	−	−	−	−	−	+	+	−	−	−
	N. soli	−	−	+	−	−	−	−	−	−	−	−	−
	*C. pinensis**	−	−	+	−	−	−	−	−	−	−	−	−
Sphingobacteriia	*S. koreensis*	−	−	+	−	−	−	−	−	−	−	−	−
	M. auburnensis	+	+	−	+	+	+	+	+	+	−	+	−
Cytophagia	*R. defluvii*	+	+	−	+	+	−	+	+	+	+	−	−
	D. endophyticus	+	−	−	−	−	−	−	−	−	−	−	−
Flavobacteriia	*F. johnsoniae*	−	−	−	−	−	+	−	−	−	−	+	+
	*F. anhuiense**	−	−	−	−	+	+	−	+	−	+	+	−
	Flavobacterium sp.	−	−	−	−	+	+	−	−	−	−	−	−

* Wild-type strains [85]

including concentrates with only a few fully assembled phages detectable by TEM (Fig. 6.2). In some cases, structures resembling partial phage components were observed but could not be unambiguously identified. For example, extract (P12) of *F. johnsoniae* contained particles resembling capsids, along with numerous thin, needle like structures. Some of these structures appeared to be connected to capsid-like particles and were interpreted as potential phage tails (Fig. 6.2C). The capsid-like particles in this extract (P12) measured approx. 65–75 nm in diameter, while the associated tail-like structure ranged from 85–105 nm in length. Based on these dimensions and overall appearance, the morphology was tentatively assigned to the siphovirus morphotype. The tail-like structure appeared non-contractile under the observed conditions, but further analysis would be required to confirm its structural properties.

In contrast, extract P7 *M. auburnensis* revealed two morphologically distinct siphovirus-like phages. These two phages differed primarily in capsid sizes: one had a capsid with a diameter of approx. 65 nm(Fig. 6.2A), the other with a diameter of approx. 34 nm (Fig. 6.2B). The tail of the larger phage appeared flexible and measured 170–180 nm (Fig. 6.2A), whereas the smaller phage had a shorter and visually more rigid tail of approx. 160–165 nm (Fig. 6.2B). Neither phage displayed retracted sheaths. Occasionally, tangled tail tips were observed in the larger phage (Fig. 6.2A), while the smaller phage appeared to lack a defined tail tip (Fig. 6.2B). Notably, the smaller phage was considerably less abundant, with only a few observed particles observed.

Extract P3 *C. jiangningensis* contained numerous phage-like structures, predominantly sheath-like structures, many of which were loosely arranged (Fig. 6.2D-F). A few complete myovirus-like phages were identified showing typical morphology with capsids, inner tail tubes, sheaths, and base-plates (Fig. 6.2D-F). The capsid diameter was approx. 80–90 nm, and tail length ranged from 105–135 nm. T he remaining extracts did not show intact phage particles under the conditions used.

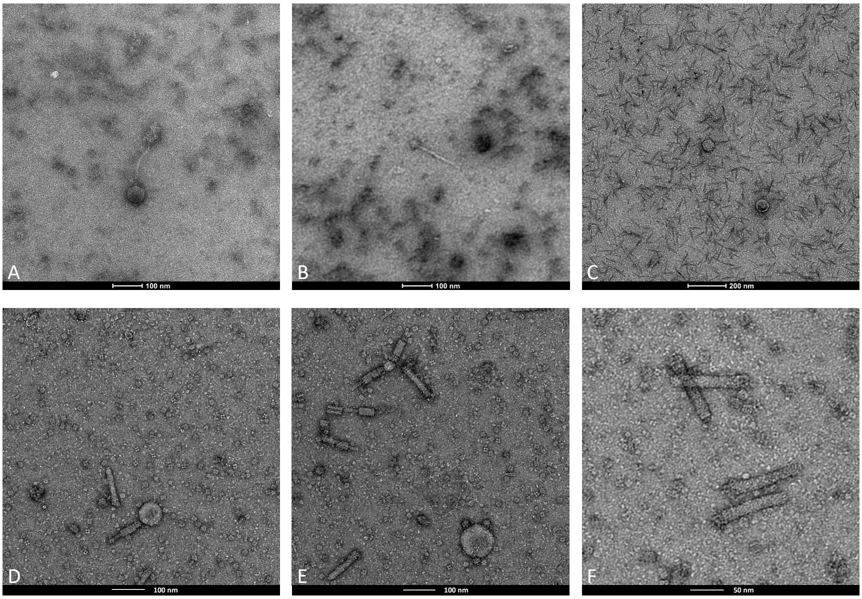

Figure 6.2: TEM images of phage particles in extracts. (A-B) Phages particles observed in P7 derived from *M. auburnensis*, displaying two morphologically distinct phage particles consistent with siphovirus morphology, (A) one with a capsid size of approx. 65 nm and (B) one with a capsid size of approx. 34 nm. (C) Phage-like particle from extract P12 (*F. johnsoniae*) showing morphology consistent with siphovirus. Capsid diameter measured approx. 65–75 nm. The extract P12 also contained numerous needle-like structures (85–105 nm in length), which were considered potential tail fibres. (D-F) Phage-like particles observed in extract P3 (*C. jiangningensis*), showing myovirus morphology. Predominant structures include partially and fully assembled sheath-like particles. (F) At higher magnification assembled base-plates can be observed on assembled sheaths. The capsid size of the P3 phage is about 80–90 nm in diameter, and the tail length ranged from 105–135 nm.

6.4 Discussion

Phages are known to significantly influence the diversity and composition of the microbial communities. They affect their hosts in various ways, including metabolic modulation and morphological alteration. Through these host-directed effects, phages may indirectly shape interspecies interactions within the microbiota, including its relationship with the superhost (plant). This raises the question of how much the observed morphological changes in *C. pinensis* (chapter 3) can be attributed to the presence or activity of phages.

To explore the distribution of prophages within the phylum Bacteroidota, especially in endophytic strains, computational prediction tools were used. These tools enable the identification of phage regions within bacterial genomes, regardless of whether they are transcriptionally active or dormant [178]. The analysis revealed prophage regions in all investigated Bacteroidota classes, with most strains carrying multiple sequences.

Their inducibility and lytic activity were then investigated, both towards the strain of origin and across the set of tested strains. As a result, all extracts exhibited lytic activity with a broad host range. Interestingly, phage activity was observed in the induced prophage extract from *M. auburnensis* (P7), despite the absence of a predicted active prophage in its genome based on current tools (Tab. 6.1). The presence of phage-particles in *M. auburnensis* extract (P7) was confirmed by TEM analysis and two distinct phage morphologies were observed (Figure 6.2). The acquired images revealed two distinct phage morphologies.

In recent years, various computational tools and pipelines have been developed to predict and identify prophage regions within bacterial genomes. These tools are now widely accessible to a broader scientific community. However, they rely on databases and statistical methods that are often based on homology. As a result, these tools tend to detect only known or closely related prophage sequences, leaving divergent or novel sequences unrecognized. Recent improvements, such as the use of genomic features like dinucleotide relative abundance, aim to reduce false negatives. Nevertheless, no single tool currently available can capture the full diversity of prophages [179], and despite recent advancements, inaccuracies still occur. This underlines the importance of culture-based validation methods.

The inducibility of prophages can vary depending on factors like growth medium, temperature, and the type of induction applied. Standard triggers such as UV light and mitomycin C, do not induce all prophages, as their specific induction requirements are unknown. Furthermore, the presence of multiple prophages within the same host genome, also known as polylysogeny, may influence inducibility [180, 181].

In addition to active prophage sequences, inactive and cryptic phage sequences may also respond to induction. Their response could involve enzymatic activity with potential bactericidal effects. Such effects might explain the appearance of "white plaques" observed during the host range plaque assays (Fig. 6.1). Similar phenomena have been described for phage-derived structure as tailocins, which can be used by host bacteria to suppress competitors [182].

The presence of diverse prophage elements across strains suggests that such traits may support community resilience, particularly under fluctuating conditions [183]. However, prophage and phage sequence elements within the host genome come with certain costs and impact the host fitness by increasing energy demand and slowing host growth. Thus, the benefits must outweigh the costs, enabling the host to survive within the competition of the microbiota. The regulatory effect of the ’kill-the-winner’principle could potentially outweigh the negative fitness impact and support the persistence of slower growing strains.

This idea may be reflected in our observations comparing *C. pinensis* (94) and *F. anhuiense* (98), both of which originated from the same endophytic microbiota. While *C. pinensis* exhibited slower growth, it showed the lowest susceptibility in the plaque assays. Conversely, *F. anhuiense* was susceptible to the extract derived from *C. pinensis* (94), but not vice versa.

Compared to the wild type strain (94), the lab strain *C. pinensis* (DSM 2588), which exhibited similar growth rates showed the highest susceptibility in the assays and was also susceptible to extracts from *F. anhuiense*. While the lab strain carried a higher total number of predicted prophage regions (131 vs. 110), the wild-type strain had more regions classified ambiguous or active. These differences may reflect functional variation in prophage content and could help explain both the variation in susceptibility and the slightly earlier onset of morphological transition observed in the wild-type strain. In addition, no plaque formation was observed in 75% of the strains when exposed to their own extract (Tab. 6.2), suggesting possible resistance mechanisms, potentially mediated by resident prophages.

This observation is consistent with previous studies suggesting that phage-associated factors can influence host cell morphology and modulate susceptibility [168, 169].

Through polylysogeny, multiple prophage-encoded resistance mechanisms can accumulate within the host genome. These coexisting prophage regions may modulate each other's inducibility. However, the hierarchical order of their inducibility and their regulatory effects on one another are not yet well understood.

In addition to their intro-host effects, phage elements, both free and integrated, can indirectly influence the superhost (plant) by modulating bacterial metabolism. These changes may alter the turnover of secondary metabolites and availability of nutrients and trace elements. Under stress conditions, phages may serve as a regulatory mechanisms that limits the overgrowth of individual strains. This in turn, may protect the superhost from both potential exploitation and destabilization of its microbiota.

Overall, this study provides first insights into the distribution and inducibility of prophages, as well as the potential host spectrum of their inducible lytic counterparts in endophytic Bacteroidota. These findings lay the groundwork for future investigations into the ecological roles and functional impacts of phages in plant-associated microbiota. In particular, the characterization of inducible prophages and cryptic phage elements may help clarify their contribution to the endophytic lifestyle and to the morphological plasticity observed in certain strains. Furthermore, exploring whether plant-derived compounds, such as root exudates, can trigger prophage induction would deepen our understanding of the regulatory dynamics between the plant as superhost and its microbiota.

ACKNOWLEDGEMENTS

TEM images were collected at the Netherlands Centre for Electron Nanoscopy (NeCEN) at Leiden University. This work benefited from access to NeCEN, which was funded in part by the Netherlands Electron Microscopy Infrastructure (NEMI), project number 184.034.014 of the National Roadmap for Large-Scale Research Infrastructure of the Dutch Research Council (NWO). J.L. was supported by the OCENW.GROOT.2019.063 and Building Blocks of Life 737.016.00 grants from the Netherlands Organization for Scientific Research (NWO), both awarded to A.B.

AUTHOR CONTRIBUTION

J.L. conceived and designed the study, supervised the project, advised both students, and wrote the manuscript. I.N.M. and K.P. conducted the experimental work as part of their respective Bachelor theses, under the supervision of J.L. A.B. supervised the overall study and provided conceptual guidance and feedback on the manuscript.

7

SUMMARY & GENERAL DISCUSSION

Brief background

Plant-microbiota are communities of microorganisms that live together in a complex system of dynamic interactions [1]. They exert a significant influence on their environment and on the host plant with which they are associated. This close relationship has evolved to such an extent that the absence of specific host organisms or key microbiota members impacts the resilience of the community. It can even affect the viability of the plant host and its associated microbiota under environmental stress conditions [4]. To explore this close relationship and decipher plant–microbiota interactions, various approaches have been used, including culture-, molecular, and omics-based methods. However, these approaches provide limited insight into interactions occurring at the cellular and topological structural level. Understanding these structural aspects is crucial for interpreting dynamic interactions in their biological context.

To address these structural aspects, microscopy-based approaches have been applied. These techniques enabled the identification of distinct colonization patterns and plant morphological changes during colonization [5, 184]. These observations suggest that the plant host actively shapes tissue-specific niche conditions to guide and regulate microbial colonization. However, both fluorescence and light microscopy are fundamentally limited by optical diffraction (~200 nm), which restricts their resolution. As a result, cellular interactions and structural changes occurring on a much smaller scale cannot be captured by light microscopy alone. Thus, an approach is required that overcomes this limit, as offered by cryo-electron microscopy (cryo-EM). In addition, cryo-EM enables the observation of cellular structures in their native hydrated state.

Research aim

The aim of this thesis is to contribute to the understanding of nanoscale interactions between endophytic microbiota and their host plant in a near-native state, using cryo-EM. To achieve this, it was necessary to develop a workflow for the preparation of large-volume samples to make plant tissue accessible for cryo-EM.

In addition, the study investigated whether endophytic microbes also undergo morphological changes during colonization, as cellular structural changes had already been observed in plant tissue [184]. For this purpose, the potential key microbiota members *C. pinensis* and arbuscular mycorrhizal fungi (AMF) were included in the structural analysis. As the study progressed, phages emerged as an integral part of plant-associated microbiota and were therefore included in the investigation.

Methodology – Endophytic morphological structure

First, structural reference data had to be obtained from axenic culture of endophytes to assess possible morphological changes during plant tissue colonisation. For this purpose, *C. pinensis* was analysed by cryo-ET, and two different cell morphologies were detected: long filamentous and small spherical cell morphologies (**Chapter 3**). In this context, it was found that the small spherical cells did not correspond to the typical characteristics of dormant cells, such as the presence of condensed DNA or structural differentiation of the outer layer from the filamentous cells [108]. These spherical cells had previously been referred to as spores or cysts in the literature, based solely on their appearance in light microscopy [97–99]. However, the observation by cryo-ET raised the question of whether these spherical cells truly correspond to the characteristics of a dormant cell stage.

In order to distinguish the small spherical cells from dormant cell stages, both cell forms were examined comparatively to assess their resistance and growth behaviour as well as their transcriptomic activity.

To further investigate potential functional differences between the two cell morphologies, hitchhiking assays were conducted using *B. subtilis.* These experiments revealed that only the small spherical cells were able to co-migrate with *B. subtilis.* To identify potential key factors mediating the observed interaction, a series of *B. subtilis* motility mutants was used, following the approach of Muok *et al.* (2020) [65]. In that study, *Streptomyces* spores were shown to hitchhike via flagellar attachment to a specialized surface layer. In contrast, cryo-EM observations in this study revealed no comparable mechanisms in *C. pinensis.* In particular, no co-migration occurred on swimming plates, suggesting that hitchhiking requires surface spreading and may involve surfactin-dependent mechanisms.

This led to the hypothesis of surfactin cheating behaviour, which was subsequently tested and confirmed. However, *C. pinensis* colonies were consistently found only along the movement direction of *B. subtilis.*

To further examine this phenomenon, a crowd-movement assay was conducted. The results showed that *C. pinensis* was unable to spread against the movement front, even in the presence of surfactin, indicating that passive co-migration is directionally constrained.

Attempts, were also made to visualise the interaction using fluorescence light microscopy (FLM) and cryo-EM. However, no clear attachment could be observed by FLM, and only two cryo-EM images showed loosely associated *C. pinensis* cells that had already begun to transition from spherical to slightly rod-shaped morphology. This observation highlighted the need to better understand the timing and progression of the morphological switch.

To determine the time of transformation and better track its progression, an attempt was made to synchronise the cell cycle and to fuse *gfp* into the chromosomal *fts*Z. This would have enabled real-time monitoring of colonisation and helped to determine which cell form occurs *in planta.* However, the methods used proved to be unsuitable and did not lead to a stable integration of *gfp* into the chromosome of *C. pinensis.*

Simultaneously, an attempt was also made to identify a possible trigger for transformation using the quorum sensing assay. The following conditions were considered potential triggers: nutrient concentration, cell density, cell form-specific quorum sensing signals, and the morphological state of the cells. As these are difficult to test individually, an attempt was made to vary their concentrations. However, the experiment turned out to be too complex, and a trigger could not be determined.

Methodology – Prophage among endophytic Bacteroidota

As previous studies have linked morphological changes in bacteria to the presence of phages [12, 168, 169], we investigated whether such a mechanism could play a role in the morphological transition of *C. pinensis* (**Chapter 6**). Since morphological plasticity was observed in the absence of externally added phages, we focused our investigation on the potential role of prophages encoded within the bacterial genome. Considering the possibility that prophages may have a broad host range, other endophytic Bacteroidota strains were included in the screening. Prophage prediction revealed that all tested endophytic Bacteroidota strains contain prophage sequences of varying predicted activity. In particular, 11 out of the 12 tested strains were predicted to harbour active prophages. Further culture based analyses confirmed the presence of inducible and active prophages in all strains tested, including both the wild-type and laboratory strains of *C. pinensis*.

To identify suitable strains for further phage enrichment and isolation, host-range assays were performed. The assay revealed that all extracts showed lytic activity against more than one bacterial strain. In some cases, strains from different Bacteroidota groups were susceptible to the same phage extract. However, attempts to isolate and purify individual phages were unsuccessful, as the phage concentration in the extracts remained too low. Neither enrichment using different host strains nor standard purification methods proved effective.

To confirm the presence of phage particles, extracts were analysed by TEM, which revealed fully assembled phages and phage-like particles in some extracts. Still, the limited yield and technical constraints prevented a more detailed investigation into their role in the morphological transformation of *C. pinensis*.

Methodology – large-volume sample preparation for cryo-EM

Alongside the structural characterisation of endophytic Bacteroidota and their phages, dedicated workflows were established to enable cryo-EM imaging of AMF (**Chapter 4**) and plant tissue (**Chapter 5**). For both sample types, the core workflow combined high-pressure freezing (HPF), fluorescence-guided targeting, cryo-lift-out and volume reduction as well as lamella preparation using cryo-plasma focussed ion beam scanning electron microscopy (PFIB/SEM).

Sample preparation was tailored to the specific requirements of each sample type, including the use of a novel planchette design and an assembly procedure adapted to the respective biological context. Due to the specific characteristics of AMF and plant root samples, the preparation procedure prior to HPF had to be adapted accordingly. For AMF, this involved further improvements of the waffle method [150] and the introduction of a new planchettes design, the so-called snap-button planchettes (**Chapter 4**). For plant tissue, a modified planchette assembly procedure – carried out while immersed in n-hexadecene –and the selection of a suitable model organism proved essential. Further details of these adaptations are provided in **Chapter 4 & 5**.

In addition to these adaptations, further refinements were made to improve the localisation of HPF samples during downstream processing. For plant tissue, histological stains allowed early visual evaluation of sample presence and positioning within the planchette, improving selection efficiency prior to PFIB/SEM processing. Fluorescent dyes, applied to both plant and AMF samples, subsequently enabled more precise localisation via integrated FLM. Details of the staining strategies and their implementation are described the respective chapters (**Chapter 4 & 5**).

Key findings

These methodological developments enabled the morphological and structural analysis of previously inaccessible volumes of intact AMF and root tissue and laid the foundation for future investigations. Given the limited time frame and the technical complexity of cryo-EM for large-volume samples, the focus of **Chapter 4 & 5** was on the development and validation of a robust and reproducible sample preparation procedure.

Beyond the technical development, the structural investigation of *C. pinensis* in **Chapter 3** revealed unexpected morphological plasticity. While the transcriptomic activity of the spherical cells indicated a slow-down, they did not exhibit the typical characteristics of dormant cells and were shown to engage in hitchhiking behaviour.

In **Chapter 6**, this investigation was extended to explore whether phages could act as regulatory trigger of the observed morphological change, and it was shown that active prophages are widespread among endophytic Bacteroidota and have a broad host range.

Synthesis of the results

Taken together, the results of this thesis reveal structural and functional characteristics of endophytic microbiota and raise new questions about their dynamic adaptive behaviour in plant-associated environments. Although no clear regulatory mechanisms could be identified, the results suggest a broader regulatory network. Morphological plasticity, prophage activity, and microbial interactions could contribute to maintaining the dynamic stability and balance of the endophytic microbiota.

This is particularly relevant as plants have been shown to actively modulate their microbiota through creating spatially and chemically distinct niches. In addition, plants have been shown to selectively shape their microbial communities and actively suppress certain members when they are no longer beneficial [185, 186].

Endophytic microorganisms must be able to adapt to changing conditions. This requires functional integration into the host environment while maintaining their ecological role within the endophytic microbiota. In this context, the morphological plasticity of *C. pinensis*, together with the associated transcriptomic shift, may represent an adaptive strategy. It could also help reduce competition among the endophytic microbiota and support persistence under resource-limited conditions.

In addition, the small spherical cells of *C. pinensis* offer distinct advantages for dissemination. Their ability to hitchhike and exploit surfactin-mediated motility allows them to passively follow microbial community movements. In this way, they could also exploit the chemotactic behaviour of motile members to reach favourable environments with minimal energy costs.

Moreover, their small size could permit passive transport through the plant's vascular system, potentially allowing relocation to sites of pathogenic attack. However, this remains hypothetical, since *in planta* tracking was not possible within the time-frame of this study.

A further hypothesis related to the role of AMF as potential mediators of microbiota dissemination. AMF networks are known to connect the roots of different plants and facilitate the exchange of nutrients and chemical signals, including warning cues when under pathogenic attack. It is conceivable that small spherical cells of *C. pinensis* could be recruited and disseminated via the AMF hyphal network. This would allow for the targeted delivery of beneficial microbes to sites of pathogen invasion, even across different host plants.

Such mechanisms could represent an efficient strategy for pre-emptive defence, limiting further pathogen spread. Whether this process is actively mediated by the plant, the AMF itself, or through cooperative signalling between both, remains an open question. It is also possible that AMF may exert selective control over which microbial partners are shared (or withheld) depending on the host's compatibility and cooperation. This raises broader ecological implications on how microbial resources might be differentially distributed in multi-partner networks.

The extent to which free phages are spread via AMF networks is still unclear. It is also conceivable that the prophages use their bacterial hosts as microbial 'Trojan horse' to further spread themself. This mechanism could have positive effects by spreading metabolic traits that enhance endophytic behaviour and promote mutualistic interaction with the plant. However, when triggered, prophages may alter microbial composition and activity, potentially affecting host–microbiota interactions.

These findings highlight the structural and ecological complexity of plant-associated microbiota, while also reflecting methodological and time limitations that shaped the scope and depth of this study. Limited access to key equipment further constrained certain experimental approaches, particularly in the cryo-EM workflow.

Challenges, limitations and future perspective

Each chapter was characterised by its own set of methodological and experimental constraints, which in turn shaped the scope of the data and the available avenues for interpretation.

In **Chapter 3**, one such challenge was the inability to synchronise the cell cycle of *C. pinensis*, despite repeated attempts using standard protocols and time-controlled reinoculation. As a result, transitional stages between the two morphologies could not be temporally resolved, which limited the interpretation of comparative transcriptional activity. The observed changes in growth and morphology occurred inconsistently across replicates, which limited the reproducibility of experiments involving the wild-type strain.

One possible solution could be to test alternatives such as nalidixic acid, which have been shown to reversible arrest the cell cycle in *Escherichia coli* [187, 188]. The effect may be further enhanced by combining it with chloramphenicol [188]. Whether this approach would yield similar effects in *C. pinensis* is currently unknown, but its potential merit further investigation. Since nalidixic acid primarily affects metabolically active cells, its effect could be tested first on the spherical cells. Given their reduced transcriptional activity observed in this study, synchronisation might be more reliable in this state. Establishing a more consistent synchronisation protocol for *C. pinensis* would also enable phase-specific comparative analyses at the transcriptomic, proteomic, and metabolic levels. This could help clarify whether the observed slow-down in transcription is merely size-related or reflects a functional differentiation between the two cell morphologies. It may also contribute to identifying intrinsic regulatory factors that trigger the morphological switch.

A major experimental limitation in **Chapter 3** was the transformation of *C. pinensis* with a green fluorescence protein (GFP) fusion construct. This was the objective of a collaboration with Le Zhang (van Wezel group, LU, NL) however, its aim was unsuccessful. This prevented live tracking of the morphological states and *in planta* visualisation of bacterial localisation. Although the plasmid had previously been successfully applied in *Flavobacterium*, its instability in *C. pinensis* may have been caused by promoter incompatibility or active defence mechanisms against foreign DNA.

To overcome the challenges in transformation in the wild-type strain, future experiments could explore the use of the laboratory strain of *C. pinensis* (DSM 2588). Preliminary observations indicate that this strain also undergoes morphological switching, although the characteristics of the transition differ slightly from those in the wild type. These differences were not examined, as this was outside the scope of the present study. However, based on the comparative prophage analysis in **Chapter 6**, the laboratory strain may exhibit a reduced defensive response to foreign DNA, which could make it more amenable to genetic manipulation. Alternatively, *Flavobacterium anhuiense*, which exhibits similar morphological shifts as *C. pinensis*, could be used as a tractable model organism. It could be used to further investigate the underlying mechanisms of the morphological shifts and the potential influence of prophages on this process.

Another challenge was the difficulty in reliable quantifying cell numbers and colony-forming units (CFUs) at specific growth stages of *C. pinensis*. Early colonies were extremely small, colourless, and only detectable under a stereomicroscope. Attempts to count cells directly using counting chambers were unsuccessful, as the small cells were difficult to focus within a single optical plane but also hard to distinguish from debris. A more efficient strategy could involve spot-plating of dilution series and fluorescence staining, combined with automated imaging using a stereo-fluorescence microscope. CFUs could then be quantified using image analysis software such as ImageJ [101].

In **Chapter 6**, the main limitation was the inability to isolate and purify individual phages in sufficient quantity for sequencing and further characterisation. Although fully assembled phage particles were detected and confirmed by TEM in some extracts, the overall phage yield was too low to enable downstream analysis. Standard concentration methods, including salt precipitation, and ultracentrifugation, proved too harsh and led to substantial loss of phage particles. Similarly, the use of filtration systems did not yield sufficient phage concentrations. Future efforts should focus on development of purification and concentration strategies with higher yield, as well as using host strains that are more susceptible to propagation of the target phages.

If sufficient quantities of phages can be recovered, this would open the door to functional studies exploring their potential contribution to morphological plasticity in *C. pinensis* and potentially other endophytic Bacteroidota. Moreover, it would allow investigation of specific traits they may carry and confer to their bacterial hosts. This may provide insights into how these bacteria evolved an endophytic lifestyle.

In **Chapter 4 & 5**, the central objective was to develop a workflow for cryo-EM analysis of large-volume biological samples, that include AMF and plant root tissue. While both AMF and plant tissue required sample specific adaptations, the overall development was shaped by similar technical constraints. Early experiments were hindered by limited access to cryo-EM equipment, in particular cryo-shuttles suitable for planchette-based sample transfer. As a result, vitrified samples had to be manually recovered from the planchette after HPF and mounted onto EM grids, which led to substantial sample loss and reduced vitrification quality.

These limitations could only be overcome through a collaboration with J. Nováček and his team at CEITEC (Brno, CZ), who provided access to PFIB/SEM systems with integrated manipulator for cryo-lift-out procedures and florescence guided targeting via integrated FLM. The use of cryo-shuttles compatible with planchettes enabled bypassing the manual mounting steps and allowed direct transfer of vitrified samples into the PFIB/SEM for downstream processing. Furthermore, the snap-button planchette system developed by J. Nováček (**Chapter 4, section 4.3.3**) significantly improved sample integrity, recovery rates after HPF, and overall workflow efficiency, while minimising sample loss.

Additional support came from the team of Toby Kiers and Vasilis Kokkoris (VU, Amsterdam, NL), who provided pre-inoculated root organs with AMF for cryo-preservation. Based on these samples, a suitable model organism could be identified for large-volume cryo-EM sample preparation. Its use enabled more consistent vitrification, better sample integrity after HPF, and increased procedural efficiency. In particular, the root organs facilitated easier handling and allowed the collection of multiple root tips from a single plate.

However, due to time constraints, it was not possible to complete downstream processing and cryo-EM data acquisition for all vitrified samples. Several AMF preparations, including early developmental stages, remain cryogenically stored at CEITEC and may be processed in future studies.

Despite these advances, sample preservation during transfer and storage remained a challenge. In particular, ice crystal contamination frequently occurred during transfer from the PFIB/SEM to the cryo-EM. This issue was further exacerbated by long waiting times prior to cryo-EM imaging. These limitations highlight the need for improved transfer procedures, and faster cryo-EM processing capabilities in future applications.

The workflows developed in this study form the basis for future investigations of the nanoscale structure of interaction between plants and their endophytic microbiota. This includes the analysis of hyphal development and intracellular organisation of AMF. It also enables the precise localisation of endophytic bacteria in plant tissue, including *C. pinensis*, provided that stable GFP integration can be achieved. This could help clarify which of the two cell morphologies of *C. pinensis* occurs in which part of the plant tissue and contribute to a better understanding of their respective functional roles. In addition, the method enables investigation of potential interaction interfaces *in planta* between endophytic bacteria and AMF at the nanoscale.

Concluding remarks

This thesis provides both biological insight and methodological progress in the structural analysis of plant–microbiota interactions. Despite significant experimental limitations, key results were achieved that lay the foundation for further nanoscale investigations. These outcomes underscore the importance of collaboration and methodological innovation in overcoming technical barriers.

The developed cryo-EM workflows now allow high-resolution studies of endophytes and AMF directly in vitrified plant tissue. By linking microbial structures to ecological function, this work contributes to a deeper understanding of host–microbiota systems and their regulatory complexity.

As automation in cryo-lift-out and lamella preparation continues to advance, the processing of large-volume samples will become more standardised and allow for higher throughput. Altogether, the findings and workflows presented here offer a solid basis for future research into the structural dynamics of plant–microbiota interactions.

SAMENVATTING

Microbiota zijn gemeenschappen van micro-organismen die samen een leefgebied bevolken. Ze komen overal in het milieu voor, ook in mensen, dieren en planten. En net zo divers als hun leefgebieden zijn, zo divers is ook hun samenstelling. Ze bestaan niet alleen uit verschillende bacteriesoorten, maar kunnen ook archaea, schimmels, virussen, bacteriofagen (fagen) en soms zelfs hogere organismen zoals protisten bevatten. De soorten van de microbiota leven niet gewoon naast elkaar, maar staan veel meer in voortdurende uitwisseling met elkaar. Ze vormen een complex systeem van interacties waarin ze elkaar beïnvloeden. Bovendien oefenen ze ook een aanzienlijke invloed uit op hun omgeving en op hun gastheerorganisme.

Deze hechte relatie tussen gastheer en microbiota is in sommige gevallen zo ver ontwikkeld dat het ontbreken van bepaalde leden van invloed kan zijn op de weerbaarheid van de gastheer. De afwezigheid van bepaalde essentiële componenten kan zulke verstrekkende gevolgen hebben dat de levensvatbaarheid van den gastheer wordt aangetast [4]. De nadruk van dit onderzoek ligt op de interactie tussen planten en hun inwonende microbiota, de zogenaamde endofyten.

Om deze relatie te onderzoeken en de interacties tussen de gastheer en zijn microbiota te ontcijferen, zijn in dit werk verschillende benaderingen gebruikt. Deze omvatten microbiële kweek, moleculaire technieken en omics-gebaseerde methoden.

Toch bieden ze slechts beperkt inzicht in de interacties op cellulair, fysiek en structureel niveau. Die zijn echter van cruciaal belang om de interpretaties binnen een biologische context te kunnen interpreteren.

Om deze structurele aspecten van de interacties te bestuderen, zijn technieken toegepast die gebaseerd zijn op microscopie. Deze technieken maakten het onder andere mogelijk om morfologische veranderingen bij de gastheer waar te nemen tijdens de kolonisatie door de endofytische microbiota [5, 184]. Dit suggereert dat de gastheer actief niche specifieke weefselomstandigheden creëert om de microbiële kolonisatie te sturen en te reguleren.

Zowel fluorescentiemicroscopie als lichtmicroscopie zijn echter fundamenteel beperkt in hun resolutie door optische diffractie (~200 nm). Daardoor kunnen cellulaire interacties en structurele veranderingen die op een veel kleinere schaal plaatsvinden, niet alleen met lichtmicroscopie worden waargenomen. Een techniek die de structuren wel in hoge resolutie in beeld kan brengen is cryo-elektronenmicroscopie (cryo-EM).

Cryo-EM is een verdere ontwikkeling van de klassieke transmissie - elektronenmicroscopie (TEM), waarbij elektronen worden gebruikt om cellulaire structuren en moleculen, zoals eiwitten, zichtbaar te maken. De twee technieken verschillen echter in de voorbereiding van de samples. Terwijl bij TEM de samples door middel van chemische en fysische processen worden gefixeerd, worden cryo-TEM-samples gevitrificeerd. Vitrificatie is een vriesproces waarbij het water in het sample zo snel bevriest dat de vorming van ijskristallen wordt voorkomen. Het resultaat is amorf (Engels: vitreous) ijs dat, net als glas, doorlaatbaar is voor elektronen en niet wordt afgebogen door kristallen. Op deze manier biedt de methode diepere inzichten in biologische structuren in hun natuurlijke staat dan TEM.

De vitrificatie van biologische moleculen en ook afzonderlijke cellen behoort inmiddels tot de gestandaardiseerde procedures. De vitrificatie van weefsels is daarentegen vanwege hun grotere volume (Engels: “large-volume”) nog steeds een uitdaging. Met name plantenweefsel vormt vanwege zijn eigenschappen, zoals stijve celwanden, vacuolen en intracellulaire gassen, extra moeilijkheden voor de vitrificatie.

Daarom was het noodzakelijk om eerst een werkwijze te ontwikkelen voor de voorbereiding van samples met een groot volume, om plantenweefsel toegankelijk te maken voor cryo-EM.

Daarnaast werd nagegaan of ook endofytische micro-organismen tijdens de kolonisatie van planten morfologische veranderingen vertonen. Daartoe werden de potentiële hoofdleden van de plantenmicrobiota *Chitinophaga pinensis* en arbusculaire mycorrhiza-schimmels (AMF) in de structuuranalyse meegenomen. In het verdere verloop van het onderzoek bleken fagen een integraal onderdeel te zijn van de plantgerelateerde microbiota en werden daarom in het onderzoek meegenomen.

De volgende hoofdstukken gaan in op verschillende aspecten van dit onderzoek, variërend van structurele bevindingen over bepaalde leden van de endofytische microbiota tot methodologische vooruitgang.

Hoofdstuk 1 schetst de wetenschappelijke achtergrond, de motivatie en de algemene doelstellingen van het werk. De nadruk ligt daarbij op het structurele onderzoek van de plantgerelateerde microbiota met behulp van cryo-EM.

Hoofdstuk 2 geeft een overzicht van de vooruitgang in cryo-EM, met bijzondere aandacht voor cryo-elektronentomografie (cryo-ET) en laat zien hoe deze technieken bijdragen aan ons begrip van de bacteriële celarchitectuur en macromoleculaire machines. Eerst wordt de ontwikkeling van cryo-EM en cryo-ET geschetst en wordt kort ingegaan op de uitdagingen en beperkingen van andere microscopietechnieken. Er worden belangrijke methodologische en technische verbeteringen beschreven die structurele ontdekkingen in prokaryotische cellen mogelijk hebben gemaakt. Tot slot worden de toekomstperspectieven voor cryo-ET besproken, met name met betrekking tot de verwerking van grote samples om hun toegankelijkheid voor cryo-ET te verbeteren.

Hoofdstuk 3 onderzoekt de morfologische structuren van de endofytische bacterie *C. pinensis* met behulp van cryo-ET. Twee verschillende celmorfologieën werden waargenomen: lange draadvormige en kleine bolvormige cellen. Hoewel ze duidelijk in grootte verschillen, vertonen beide een vergelijkbare interne structurele organisatie. Daarnaast werd onderzocht of de bolvormige celmorfologie overeenkomt met een rustende celtoestand, zoals bekend van sporen.

De belangrijkste resultaten tonen aan dat de twee vormen verschillende transcriptomische profielen hebben. Hoewel het profiel van de bolvormige cellen wijst op een vertraagd metabolisme, vertonen ze geen andere typische kenmerken van rustende of persistercellen. De bolvormige cellen blijven delingsactief en vertonen in co-cultuur met beweeglijke bacteriën een gedrag dat overeenkomt met passief meeliften.

Hoofdstuk 4 behandelt de morfologische en structurele organisatie van hyfen van arbusculaire mycorrhiza-schimmels (AMF) in verschillende ontwikkelingsstadia. De nadruk lag op het identificeren van structuren die betrokken zijn bij de regulatie van het bidirectionele transportsysteem. Om dit mogelijk te maken, werd een geschikte werkwijze ontwikkeld die de integriteit van de samples behoudt en een succesvolle vitrificatie van het hyfenetwerk garandeert. Deze methode maakte het vervolgens mogelijk om de samples verder te bewerken met cryo-plasma-focus-ionenstraal-rasterelektronenmicroscopie (kortweg: cryo-PFIB/SEM), een techniek die seriële beeldvorming en voorbereiding van lamellen voor verdere analyse via cryo-ET mogelijk maakte.

Hoofdstuk 5 gaat over de uitdagingen bij het voorbereiden van grote samples van plantenwortelweefsel voor cryo-EM-beeldvorming. Het hoofdstuk schetst de ontwikkeling van een workflow voor het vitrificeren van plantenwortels. De vitrificatie proces wordt gevolgd door volumevermindering in cryogene toestand met behulp van cryo-PFIB/SEM en de lift-out-methode om kleinere volumes te extraheren. Het geëxtraheerde kleinere volume maakte verdere verwerking en de voorbereiding van zogenaamde lamellen voor cryo-EM-beeldvorming mogelijk. In deze studie werden wortelorganen geïdentificeerd als een ideaal modelsysteem voor de preparatie van cryo-EM-samples met een groot volume. De combinatie van dit modelorganisme en de nieuwe workflow leidde tot aanzienlijke verbeteringen in de vitrificatiekwaliteit en de doorvoer van samples.

Hoofdstuk 6 onderzoekt in hoeverre de aanwezigheid van fagen bijdraagt aan de morfologische plasticiteit van *C. pinensis*. Daartoe werd het genoom van *C. pinensis* en verwante endofytische Bacteroidota-stammen geanalyseerd op de aanwezigheid van profagen, met behulp van webgebaseerde voorspellingsmethoden en kweekgebaseerde assays.

De belangrijkste bevinding is dat alle geteste stammen induceerbare en actieve profagensequenties bevatten. Daarnaast wijzen de resultaten op een breed gastheerspectrum van de geïnduceerde fagen binnen endofytische Bacteroidota. Door moeilijkheden bij de verdere isolatie van fagen kon echter geen direct verband worden vastgesteld met de morfologische veranderingen in *C. pinensis*. Niettemin biedt deze studie waardevolle inzichten in de verspreiding van profagen onder endofytische Bacteroidota.

Samenvattende conclusie: De in deze studie ontwikkelde werkmethoden bieden nieuwe mogelijkheden om de interacties tussen planten en hun endofytische microbiota in een natuurlijke omgeving te analyseren. Daarnaast maken ze het mogelijk om de cellulaire en structurele mechanismen te bestuderen die betrokken zijn bij de uitwisseling en het transport van hulpbronnen tussen AMF-symbionten en hun gastheerplanten.

ZUSAMMENFASSUNG

Mikrobiota sind Gemeinschaften von Mikroorganismen, die zusammen einen Lebensraum besiedeln. Sie kommen überall in der Umwelt vor, so auch in Menschen, Tieren und Pflanzen. Und so vielfältig ihre Lebensräume sind, genauso vielfältig ist ihre Zusammensetzung. Sie bestehen dabei nicht nur aus verschiedenen Bakterienarten, sondern können auch Archaeen, Pilze, Viren, Bakteriophagen (Phagen) und teilweise sogar höhere Organismen wie Protisten beinhalten. Dabei leben die Mitglieder der Mikrobiota nicht schlicht nebeneinanderher, sondern stehen viel mehr im ständigen Austausch. Sie bilden ein komplexes System an Wechselwirkungen, in dem sie sich gegenseitig beeinflussen. Darüber hinaus üben sie auch einen erheblichen Einfluss auf ihre Umwelt und auch auf ihren Wirtsorganismus aus.

Diese enge Beziehung zwischen Wirt und seiner Mikrobiota hat sich teils so weit entwickelt, dass sich das Fehlen bestimmter Mitglieder auf die Widerstandsfähigkeit des Wirtes auswirken kann. Es kann sogar so weit gehen, dass das Fehlen sogenannter Schlüsselmitglieder die Lebensfähigkeit des Wirtes beeinträchtigt [4]. Schwerpunkt dieser Arbeit ist die Interaktion zwischen Pflanzen und ihren innenwohnenden Mikrobiota, den sogenannten Endopyhten.

Um diese enge Beziehung zu erforschen und die Wechselwirkungen zwischen dem Wirt und seiner Mikrobiota zu entschlüsseln, wurden in dieser Arbeit verschiedene Ansätze verwendet. Diese umfassen kultivierungs-, molekulare- und omik-basierende Methoden.

Jedoch bieten sie nur einen begrenzten Einblick in die Interaktionen auf der zellulären und physischen bzw. strukturellen Ebene. Diese wiederum ist wichtig für die Interpretation der Interaktionen im biologischen Kontext.

Um diese strukturellen Aspekte der Interaktionen zu untersuchen, wurden Mikroskopie basierende Techniken verwendet. Diese Techniken ermöglichten unter anderem die Beobachtung morphologischer Veränderungen des Wirtes während der Besiedlung durch die endophytische Mikrobiota [5, 184]. Dies deutet darauf hin, dass der Wirt aktiv gewebespezifische Nischenbedingungen gestaltet, um die mikrobielle Besiedlung zu steuern und zu regulieren.

Sowohl die Fluoreszenz- als auch die Lichtmikroskopie sind jedoch grundsätzlich in ihrer Auflösung durch die optische Beugung (˜200 nm) begrenzt. Infolgedessen können zelluläre Interaktionen und strukturelle Veränderungen, die in einem viel kleineren Maßstab stattfinden, nicht allein durch Lichtmikroskopie erfasst werden. Daher ist ein Ansatz erforderlich, der diese Einschränkungen überwindet, wie beispielsweise die Kryo-Elektronenmikroskopie (Kryo-EM).

Die Kryo-EM ist eine Weiterentwicklung der klassischen Transmissionelektronenmikroskopie (TEM), bei der Elektronen verwendet werden um zelluläre Strukturen und Moleküle, wie Proteine, sichtbar zu machen. Jedoch unterscheiden sich die beiden Techniken in der Probenaufbereitung. Während bei der TEM die Proben mittels chemisch und physikalischer

Verfahren fixiert werden, werden Kryo-TEM Proben vitrifiziert. Vitrifizierung beschreibt ein Verfahren des Gefrierens bei dem das Wasser in der Probe so schnell gefriert, dass eine Eiskristallbildung verhindert wird. Das Resultat ist amorphes (engl.: vitreous) Eis, das wie Glas für die Elektronen durchlässig ist und nicht von Kristallen abgelenkt wird. Auf diese Weise erlaubt das Verfahren tiefere Einblicke in biologische Strukturen in ihrem nativen Zustand.

Die Vitrifizierung von biologischen Molekülen und auch einzelnen Zellen, gehört inzwischen zu den standardisierten Verfahren, wohingegen die Vitrifizierung von Geweben aufgrund ihres größeren Volumens (engl. „large-volume“) immer noch eine Herausforderung darstellt. Insbesondere Pflanzengewebe stellt aufgrund seiner Eigenschaften wie rigide Zellwände, Vakuolen und intrazellulären Gase zusätzliche Schwierigkeiten für die Vitrifikation dar.

Daher war es notwendig, zunächst einen Arbeitsablauf für die Vorbereitung großvolumiger Proben zu entwickeln, um Pflanzengewebe für die Kryo-EM zugänglich zu machen.

Zusätzlich wurde untersucht, ob auch endophytische Mikroorganismen während der Pflanzenbesiedlung ebenfalls morphologische Veränderungen erfahren. Zu diesem Zweck wurden die potenziellen Hauptmitglieder der Pflanzenmikrobiota *Chitinophaga pinensis* und Arbuskuläre Mykorrhizapilze (AMF) in die Strukturanalyse einbezogen. Im weiteren Verlauf der Studie erwiesen sich Phagen als integraler Bestandteil der pflanzenassoziierten Mikrobiota und wurden daher in die Untersuchung einbezogen.

Die folgenden Kapitel befassen sich mit verschiedenen Aspekten dieser Untersuchungen, welche von strukturellen Erkenntnissen über bestimmte Mitglieder der endophytischen Mikrobiota bis hin zu methodischen Fortschritten reichen.

Kapitel 1 umreißt den wissenschaftlichen Hintergrund, die Motivation und die allgemeinen Ziele der Arbeit. Der Schwerpunkt liegt dabei auf der strukturellen Untersuchung der pflanzenassoziierten Mikrobiota mittels Kryo-EM.

Kapitel 2 gibt einen Überblick über die Fortschritte in der Kryo-EM mit besonderem Schwerpunkt auf der Kryo-Elektronentomographie (Kryo-ET), sowie deren Beitrag zu unserem Verständnis der bakteriellen Zellarchitektur und makromolekularen Maschinen. Zunächst wird die Entwicklung der Kryo-EM und der Kryo-ET skizziert und kurz auf die Herausforderungen und Grenzen anderer Mikroskopie Techniken eingegangen. Es werden wichtige methodische und technische Verbesserungen beschrieben, die strukturelle Entdeckungen in prokaryotischen Zellen ermöglicht haben. Abschließend werden die Zukunftsaussichten für die Kryo-ET erörtert, insbesondere im Hinblick auf die Aufbereitung von großvolumigen Proben, um deren Zugänglichkeit für die Kryo-ET zu verbessern.

Kapitel 3 untersucht die morphologischen Strukturen des endophytischen Bakterium *C. pinensis* mittels Kryo-ET. Es wurden zwei unterschiedliche Zellmorphologien beobachtet: lange fadenförmige und kleine kugelförmige Formen. Obwohl sie sich in ihrer Größe deutlich unterscheiden, wiesen beide eine ähnliche interne strukturelle Organisation auf. Es wird ferner untersucht, ob die kugelförmige Zellmorphologie einem ruhenden Zellzustand, wie sie bei Sporen angenommen wird, entspricht.

Die wichtigsten Ergebnisse zeigen, dass die beiden Morphologien unterschiedliche transkriptomische Profile aufweisen. Obwohl das Transkriptom-Profil der kugelförmigen Zellen auf eine Verlangsamung des Metabolismus hindeutet, weisen sie keine weiteren typischen Merkmale von ruhenden oder persistierenden Zellen auf. Die sphärischen Zellen bleiben replikationsfähig und zeigen in Co-Kultur mit beweglichen Bakterien ein passives Mittransportverhalten.

Kapitel 4 befasst sich mit der morphologischen und strukturellen Organisation von Hyphen arbuskulärer Mykorrhizapilze (AMF) in verschiedenen Entwicklungsstadien. Das Hauptaugenmerk lag auf der Identifizierung von Strukturen, die an der Regulierung des bidirektionalen Transportsystems beteiligt sind. Um dies zu erreichen, wurde ein geeigneter Arbeitsablauf entwickelt, der die Integrität der Proben bewahrt und eine erfolgreiche Vitrifizierung des Hyphen-Netzwerks gewährleistet. Dies ermöglichte die weitere Bearbeitung der Proben mit Hilfe der Kryo-Plasma-Fokus-Ionenstrahl-Rasterelektronenmikroskopie (kurz: cryo-PFIB/SEM), die eine serielle Bildgebung und Lamellenpräparation für die Kryo-ET-Analyse ermöglichte.

Kapitel 5 befasst sich mit den Herausforderungen bei der Vorbereitung großvolumiger Proben aus Pflanzenwurzelgewebe für die Kryo-EM-Bildgebung. Es skizziert die Entwicklung eines Arbeitsablaufs für die Vitrifizierung von Pflanzenwurzeln. Auf den Arbeitsablauf der Vitrifizierung folgt die Volumenreduzierung im Kryozustand mit Hilfe von cryo-PFIB/SEM und der Lift-out-Methode zum Extrahieren kleinerer Volumina. Das extrahierte kleinere Volumen ermöglichte die weitere Verarbeitung und die Präparation von sogenannten Lamellen für die Kryo-EM-Bildgebung. In dieser Studie wurden Wurzelorgane als ideales Modellsystem für die Präparation großvolumiger Kryo-EM-Proben identifiziert. Die Kombination aus diesem Modellorganismus und dem neuen Arbeitsablauf führte zu erheblichen Verbesserungen bei der Vitrifizierungsqualität und dem Probendurchsatz.

Kapitel 6 untersucht, inwieweit die Anwesenheit von Phagen zur morphologischen Plastizität von *C. pinensis* beiträgt. Zu diesem Zweck wurde das Genom von *C. pinensis* und verwandten endophytischen Bacteroidota-Stämmen mithilfe von webbasierten Vorhersagemethoden und kulturbasierten Assays auf Prophagen untersucht.

Das wichtigste Ergebnis ist, dass alle getesteten Stämme induzierbare und aktive Prophagen-Sequenzen beherbergen. Des Weiteren deuten die Ergebnisse auf ein breites Wirtsspektrum der induzierten Phagen unter endophytischen Bacteroidota hin. Aufgrund von Schwierigkeiten bei der weiteren Phagen Isolierung konnte jedoch kein direkter Zusammenhang mit den morphologischen Veränderungen in *C. pinensis* hergestellt werden. Nichtsdestotrotz bietet die Studie wertvolle Einblicke in die Verbreitung von Prophagen in endophytischen Bacteroidota.

Zusammenfassende Schlussfolgerung: Die in dieser Studie entwickelten Arbeitsabläufe eröffnen neue Möglichkeiten für die Analyse der Interaktionen zwischen Pflanzen und ihrer endophytischen Mikrobiota im naturnahen Zustand. Darüber hinaus ermöglichen sie die Untersuchung der zellulären strukturellen Mechanismen, die unter andrem am Austausch und Transport von Ressourcen zwischen AMF-Symbionten und ihren Wirtspflanzen beteiligt sind.

REFERENCES

[1] Berg G, Rybakova D, Fischer D, Cernava T, Vergès MC, Charles T, et al. Microbiome definition re-visited: old concepts and new challenges. Microbiome. 2020 Jun 30;8(1):103. Erratum in: Microbiome. 2020 Aug 20;8(1):119. doi: 10.1186/s40168-020-00905-x.

[2] Rolfe SA, Griffiths J, Ton J. Crying out for help with root exudates: adaptive mechanisms by which stressed plants assemble health-promoting soil microbiomes. Curr Opin Microbiol. 2019;49:73-82.

[3] Liu H, Li J, Carvalhais LC, Percy CD, Verma JP, Schenk PM, et al. Evidence for the plant recruitment of beneficial microbes to suppress soil-borne pathogens. New Phytol. 2021 Mar;229(5):2873-85.

[4] Spooren J, van Bentum S, Thomashow LS, Pieterse CMJ, Weller DM, Berendsen RL. Plant-Driven Assembly of Disease-Suppressive Soil Microbiomes. Annu Rev Phytopathol. 2024;62(1):1-30.

[5] Hartmann A, Fischer D, Kinzel L, Chowdhury SP, Hofmann A, Baldani JI, et al. Assessment of the structural and functional diversities of plant microbiota: Achievements and challenges - A review. J Adv Res. 2019 Apr 30;19:3-13.

[6] Berg G. Plant-microbe interactions promoting plant growth and health: perspectives for controlled use of microorganisms in agriculture. Appl Microbiol Biotechnol. 2009 Aug;84(1):11-8.

[7] Hadrich D. Microbiome Research Is Becoming the Key to Better Understanding Health and Nutrition. Front Genet. 2018 Jun 13;9:212.

[8] Pan X, Raaijmakers JM, Carrión VJ. Importance of Bacteroidetes in host-microbe interactions and ecosystem functioning. Trends Microbiol. 2023 Sep;31(9):959-71.

[9] Thingstad TF. Elements of a theory for the mechanisms controlling abundance, diversity, and biogeochemical role of lytic bacterial viruses in aquatic systems. Limnology and Oceanography. 2000;45(6):1320-8.

[10] Mann NH, Cook A, Millard A, Bailey S, Clokie M. Marine ecosystems: bacterial photosynthesis genes in a virus. Nature. 2003;424(6950):741.

[11] Wendling CC, Refardt D, Hall AR. Fitness benefits to bacteria of carrying prophages and prophage-encoded antibiotic-resistance genes peak in different environments. Evolution. 2021 Feb;75(2):515-28.

[12] Bulssico J, Papukashvili I, Espinosa L, Gandon S, Ansaldi M. Phage-antibiotic synergy: Cell filamentation is a key driver of successful phage predation. PLoS Pathog. 2023 Sep 13;19(9):e1011602.

[13] Lanfranco L, Bonfante P, Genre A. The Mutualistic Interaction between Plants and Arbuscular Mycorrhizal Fungi. Microbiol Spectr. 2016 Dec;4(6).

[14] Dubochet J. The physics of rapid cooling and its implications for cryoimmobilization of cells. Methods Cell Biol. 2007;79:7-21.

[15] Shimoni E, Müller M. On optimizing high-pressure freezing: from heat transfer theory to a new microbiopsy device. J Microsc. 1998 Dec;192(Pt 3):236-47.

[16] Studer D, Humbel BM, Chiquet M. Electron microscopy of high pressure frozen samples: bridging the gap between cellular ultrastructure and atomic resolution. Histochem Cell Biol. 2008 Nov;130(5):877-89.

[17] Dubochet J, Adrian M, Chang JJ, Homo JC, Lepault J, McDowall AW, et al. Cryo-electron microscopy of vitrified specimens. Q Rev Biophys. 1988;21(2):129-228.

[18] Grimm R, Singh H, Rachel R, Typke D, Zillig W, Baumeister W. Electron tomography of ice-embedded prokaryotic cells. Biophys J. 1998;74:1031.

[19] Jensen GJ, Briegel A. How electron cryotomography is opening a new window onto prokaryotic ultrastructure. Curr Opin Struct Biol. 2007;17(2):260-7.

[20] Latino L, Midoux C, Vergnaud G, Pourcel C. Investigation of Pseudomonas aeruginosa strain PcyII-10 variants resisting infection by N4-like phage Ab09 in search for genes involved in phage adsorption. PLoS One. 2019;14:e0215456.

[21] Nickell S, Hegerl R, Baumeister W, Rachel R. Pyrodictium cannulae enter the periplasmic space but do not enter the cytoplasm, as revealed by cryo-electron tomography. J Struct Biol. 2003;141:34-42.

[22] Hegerl R. The EM program package: A platform for image processing in biological electron microscopy. J Struct Biol. 1996;116:30-4.

[23] Mastronarde DN. Automated electron microscope tomography using robust prediction of specimen movements. J Struct Biol. 2005;152:36-51.

[24] Nickell S, Förster F, Linaroudis A, Del Net W, Beck F, Hegerl R, et al. TOM software toolbox: Acquisition and analysis for electron tomography. J Struct Biol. 2005;149:227-34.

[25] Zheng SQ, Keszthelyi B, Branlund E, Lyle JM, Braunfeld MB, Sedat JW, et al. UCSF tomography: An integrated software suite for real-time electron microscopic tomographic data collection, alignment, and reconstruction. J Struct Biol. 2007;157:138-47.

[26] Kremer JR, Mastronarde DN, McIntosh JR. Computer visualization of three-dimensional image data using IMOD. J Struct Biol. 1996;116:71-6.

[27] Tegunov D, Cramer P. Real-time cryo-electron microscopy data preprocessing with Warp. Nat Methods. 2019;16(11):1146-52.

[28] Baldwin PR, Tan YZ, Eng ET, Rice WJ, Noble AJ, Negro CJ, et al. Big data in cryoEM: automated collection, processing and accessibility of EM data. Curr Opin Microbiol. 2018;43:1-8.

[29] Szwedziak P, Ghosal D. FtsZ-ring architecture and its control by MinCD. In: Löwe J, Amos LA, editors. Subcellular Biochemistry. vol. 84. Cham: Springer; 2017. p. 213-44.

[30] Bi E, Lutkenhaus J. FtsZ ring structure associated with division in Escherichia coli. Nature. 1991;354:161-4.

[31] Li Z, Trimble MJ, Brun YV, Jensen GJ. The structure of FtsZ filaments in vivo suggests a force-generating role in cell division. EMBO J. 2007;26:4694-708.

[32] Szwedziak P, Wang Q, Bharat TAM, Tsim M, Löwe J. Architecture of the ring formed by the tubulin homologue FtsZ in bacterial cell division. Elife. 2014 Dec;3:e04601.

[33] Yao Q, Jewett AI, Chang Y, Oikonomou CM, Beeby M, Iancu CV, et al. Short FtsZ filaments can drive asymmetric cell envelope constriction at the onset of bacterial cytokinesis. EMBO J. 2017;36:1577-89.

[34] Ortega DR, Oikonomou CM, Ding HJ, Rees-Lee P, Alexandria, Jensen GJ. ETDB-Caltech: A blockchain-based distributed public database for electron tomography. PLoS One. 2019;14:e0215531.

[35] Swulius MT, Chen S, Ding HJ, Li Z, Briegel A, Pilhofer M, et al. Long helical filaments are not seen encircling cells in electron cryotomograms of rod-shaped bacteria. Biochem Biophys Res Commun. 2011;407:650-5.

[36] Domínguez-Escobar J, Chastanet A, Crevenna AH, Fromion V, Wedlich-Söldner R, Carballido-López R. Processive movement of MreB-associated cell wall biosynthetic complexes in bacteria. Science. 2011;333:225-8.

[37] Van Teeffelen S, Wang S, Furchtgott L, Huang KC, Wingreen NS, Shaevitz JW, et al. The bacterial actin MreB rotates, and rotation depends on cell-wall assembly. Proc Natl Acad Sci USA. 2011;108:15822-7.

[38] Swulius MT, Jensen GJ. The helical mreb cytoskeleton in Escherichia coli MC1000/pLE7 is an artifact of the N-terminal yellow fluorescent protein tag. J Bacteriol. 2012;194:6382-6.

[39] Pilhofer M, Jensen GJ. The bacterial cytoskeleton: more than twisted filaments. Curr Opin Cell Biol. 2013;25:125.

[40] Al-Amoudi A, Chang JJ, Leforestier A, McDowall A, Salamin LM, Norlén LPO, et al. Cryo-electron microscopy of vitreous sections. EMBO J. 2004;23:3583.

[41] Bleck CKE, Merz A, Gutierrez MG, Walther P, Dubochet J, Zuber B, et al. Comparison of different methods for thin section em analysis of Mycobacterium smegmatis. J Microsc. 2010;237:23-38.

[42] Ebersold HR, Cordier JL, Lüthy P. Bacterial mesosomes: Method dependent artifacts. Arch Microbiol. 1981;130:19-22.

[43] Yonekura K, Braunfeld MB, Maki-Yonekura S, Agard DA. Electron energy filtering significantly improves amplitude contrast of frozen-hydrated protein at 300 kV. J Struct Biol. 2006;156:524-36.

[44] Marko M, Hsieh C, Schalek R, Frank J, Mannella C. Focused-ion-beam thinning of frozen-hydrated biological specimens for cryo-electron microscopy. Nat Methods. 2007;4:215-7.

[45] Melia CE, Bolla JR, Katharios-Lanwermeyer S, Mihaylov DB, Hoffmann PC, Huo J, et al. Architecture of cell-cell junctions in situ reveals a mechanism for bacterial biofilm inhibition. Proc Natl Acad Sci U S A. 2021;118.

[46] Weiss GL, Kieninger AK, Maldener I, Forchhammer K, Pilhofer M. Structure and Function of a Bacterial Gap Junction Analog. Cell. 2019;178:374-84.e15.

[47] Khanna K, Lopez-Garrido J, Sugie J, Pogliano K, Villa E. Asymmetric localization of the cell division machinery during Bacillus subtilis sporulation. Elife. 2021 May;10:e62204.

[48] Tocheva EI, López-Garrido J, Hughes HV, Fredlund J, Kuru E, VanNieuwenhze MS, et al. Peptidoglycan transformations during Bacillus subtilis sporulation. Mol Microbiol. 2013;88:673.

[49] Tocheva EI, Matson EG, Morris DM, Moussavi F, Leadbetter JR, Jensen GJ. Peptidoglycan Remodeling and Conversion of an Inner Membrane into an Outer Membrane During Sporulation. Cell. 2011;146:799.

[50] Harapin J, Börmel M, Sapra KT, Brunner D, Kaech A, Medalia O. Structural analysis of multicellular organisms with cryo-electron tomography. Nat Methods. 2015;12:634-6.

[51] Kuba J, Mitchels J, Hovorka M, Erdmann P, Berka L, Kirmse R, et al. Advanced cryo-tomography workflow developments – correlative microscopy, milling automation and cryo-lift-out. J Microsc. 2021;281:112-24.

[52] Schaffer M, Pfeffer S, Mahamid J, Kleindiek S, Laugks T, Albert S, et al. A cryo-FIB lift-out technique enables molecular-resolution cryo-ET within native Caenorhabditis elegans tissue. Nat Methods. 2019;16:757-62.

[53] Gorelick S, Korneev D, Handley A, Gervinskas G, Oorschot V, Kaluza OL, et al. Oxygen plasma focused ion beam scanning electron microscopy for biological samples. bioRxiv [Preprint]. 2018.

[54] Briegel A, Ding HJ, Li Z, Werner J, Gitai Z, Dias DP, et al. Location and architecture of the Caulobacter crescentus chemoreceptor array. Mol Microbiol. 2008 Jul;69(1):30-41.

[55] Ingerson-Mahar M, Briegel A, Werner JN, Jensen GJ, Gitai Z. The metabolic enzyme CTP synthase forms cytoskeletal filaments. Nat Cell Biol. 2010;128(12):739-46.

[56] Schlimpert S, Klein EA, Briegel A, Hughes V, Kahnt J, Bolte K, et al. General protein diffusion barriers create compartments within bacterial cells. Cell. 2012;151:1270-82.

[57] Basler M, Pilhofer M, Henderson GP, Jensen GJ, Mekalanos JJ. Type VI secretion requires a dynamic contractile phage tail-like structure. Nature. 2012;483:182-6.

[58] Szwedziak P, Pilhofer M. Bidirectional contraction of a type six secretion system. Nat Commun. 2019;10:1-11.

[59] Chang YW, Chen S, Tocheva EI, Treuner-Lange A, Löbach S, Søgaard-Andersen L, et al. Correlated cryogenic photoactivated localization microscopy and cryo-electron tomography. Nat Methods. 2014;11:737-9.

[60] Lučić V, Förster F, Baumeister W. Structural studies by electron tomography: From cells to molecules. Annu Rev Biochem. 2005;74:833-65.

[61] Hrabe T, Chen Y, Pfeffer S, Kuhn Cuellar L, Mangold AV, Förster F. PyTom: A python-based toolbox for localization of macromolecules in cryo-electron tomograms and subtomogram analysis. J Struct Biol. 2012;178:177-88.

[62] Briegel A, Li X, Bilwes AM, Hughes KT, Jensen GJ, Crane BR. Bacterial chemoreceptor arrays are hexagonally packed trimers of receptor dimers networked by rings of kinase and coupling proteins. Proc Natl Acad Sci. 2012;109:3766-71.

[63] Liu J, Hu B, Morado DR, Jani S, Manson MD, Margolin W. Molecular architecture of chemoreceptor arrays revealed by cryoelectron tomography of Escherichia coli minicells. Proc Natl Acad Sci. 2012;109:E1481-8.

[64] Burt A, Cassidy CK, Ames P, Bacia-Verloop M, Baulard M, Huard K, et al. Complete structure of the chemosensory array core signalling unit in an E. coli minicell strain. Nat Commun. 2020;11:1-9.

[65] Muok AR, Briegel A, Crane BR. Regulation of the chemotaxis histidine kinase CheA: A structural perspective. Biochim Biophys Acta - Biomembr. 2020 Jan;1862(1):183030.

[66] Yang W, Keith Cassidy C, Ames P, Diebolder CA, Schulten K, Luthey-Schulten Z, et al. In situ conformational changes of the Escherichia coli serine chemoreceptor in different signaling states. mBio. 2019 Jul;10(4):e00973-19.

[67] Briegel A, Ames P, Gumbart JC, Oikonomou CM, Parkinson JS, Jensen GJ. The mobility of two kinase domains in the escherichia coli chemoreceptor array varies with signalling state. Mol Microbiol. 2013;89:831-41.

[68] Carroll BL, Liu J. Structural Conservation and Adaptation of the Bacterial Flagella Motor. Biomol. 2020;10:1492.

[69] Liu J, Lin T, Botkin DJ, McCrum E, Winkler H, Norris SJ. Intact flagellar motor of Borrelia burgdorferi revealed by cryo-electron tomography: Evidence for stator ring curvature and rotor/C-ring assembly flexion. J Bacteriol. 2009;191:5026-36.

[70] Rossmann FM, Hug I, Sangermani M, Jenal U, Beeby M. In situ structure of the Caulobacter crescentus flagellar motor and visualization of binding of a CheY-homolog. Mol Microbiol. 2020;114:443-53.

[71] Dandey VP, Wei H, Zhang Z, Tan YZ, Acharya P, Eng ET, et al. Spotiton: New features and applications. J Struct Biol. 2018;202:161-9.

[72] Ravelli RBG, Nijpels FJT, Henderikx RJM, Weissenberger G, Thewessem S, Gijsbers A, et al. Cryo-EM structures from sub-nl volumes using pin-printing and jet vitrification. Nat Commun. 2020;11:1-9.

[73] Wei H, Dandey VP, Zhang Z, Raczkowski A, Rice WJ, Carragher B, et al. Optimizing "self-wicking" nanowire grids. J Struct Biol. 2018;202:170-4.

[74] Schwartz O, Axelrod JJ, Campbell SL, Turnbaugh C, Glaeser RM, Müller H. Laser phase plate for transmission electron microscopy. Nat Methods. 2019;16:1016-20.

[75] Chreifi G, Chen S, Jensen GJ. Rapid tilt-series method for cryo-electron tomography: Characterizing stage behavior during FISE acquisition. J Struct Biol. 2021;213:107716.

[76] Eisenstein F, Danev R, Pilhofer M. Improved applicability and robustness of fast cryo-electron tomography data acquisition. J Struct Biol. 2019;208:107-14.

[77] Tegunov D, Xue L, Dienemann C, Cramer P, Mahamid J. Multi-particle cryo-EM refinement with M visualizes ribosome-antibiotic complex at 3.5 Å in cells. Nat Methods. 2021;18:186-93.

[78] Tacke S, Erdmann P, Wang Z, Klumpe S, Grange M, Plitzko J, et al. A streamlined workflow for automated cryo focused ion beam milling. J Struct Biol. 2021;213:107743.

[79] Zachs T, Schertel A, Medeiros J, Weiss GL, Hugener J, Matos J, et al. Fully automated, sequential focused ion beam milling for cryo-electron tomography. Elife. 2020;9:e52286.

[80] Oikonomou CM, Jensen GJ. The Atlas of Bacterial and Archaeal Cell Structure: an Interactive Open-Access Microbiology Textbook. J Microbiol Biol Educ. 2021 Aug;22(2):e00128-1.

[81] Trivedi P, Leach JE, Tringe SG, Sa T, Singh BK. Plant-microbiome interactions: from community assembly to plant health. Nat Rev Microbiol. 2020 Nov;18(11):607-21.

[82] Vandenkoornhuyse P, Quaiser A, Duhamel M, Le Van A, Dufresne A. The importance of the microbiome of the plant holobiont. New Phytol. 2015;206(4):1196-206.

[83] Hildebrand F, Gossmann TI, Frioux C, Özkurt E, Myers PN, Ferretti P, et al. Dispersal strategies shape persistence and evolution of human gut bacteria. Cell Host Microbe. 2021 Jul;29(7):1167-76.e9.

[84] Pérez-Jaramillo JE, Carrión VJ, de Hollander M, Raaijmakers JM. The wild side of plant microbiomes. Microbiome. 2018 Aug;6(1):143.

[85] Carrión VJ, Perez-Jaramillo J, Cordovez V, Tracanna V, de Hollander M, Ruiz-Buck D, et al. Pathogen-induced activation of disease-suppressive functions in the endophytic root microbiome. Science. 2019 Nov;366(6465):606-12.

[86] Liu Y, Zhang H, Wang J, Gao W, Sun X, Xiong Q, et al. Nonpathogenic Pseudomonas syringae derivatives and its metabolites trigger the plant "cry for help" response to assemble disease suppressing and growth promoting rhizomicrobiome. Nat Commun. 2024 Mar;15(1):1907.

[87] Salas-González I, Reyt G, Flis P, Custódio V, Gopaulchan D, Bakhoum N, et al. Coordination between microbiota and root endodermis supports plant mineral nutrient homeostasis. Science. 2021;371(6525):eabd0695.

[88] Matsumoto H, Fan X, Wang Y, et al. Bacterial seed endophyte shapes disease resistance in rice. Nat Plants. 2021;7:60-72.

[89] Vives-Peris V, de Ollas C, Gómez-Cadenas A, et al. Root exudates: from plant to rhizosphere and beyond. Plant Cell Rep. 2020;39:3-17.

[90] Yang W, Briegel A. Diversity of Bacterial Chemosensory Arrays. Trends Microbiol. 2020 Jan;28(1):68-80.

[91] Briegel A, Ladinsky MS, Oikonomou C, Jones CW, Harris MJ, Fowler DJ, et al. Structure of bacterial cytoplasmic chemoreceptor arrays and implications for chemotactic signaling. Elife. 2014 Jun;3:e02151.

[92] Shrivastava A, Berg HC. Towards a model for Flavobacterium gliding. Curr Opin Microbiol. 2015 Dec;28:93-7.

[93] Mattingly AE, Weaver AA, Dimkovikj A, Shrout JD. Assessing Travel Conditions: Environmental and Host Influences On Bacterial Surface Motility. J Bacteriol. 2018 Mar;200(11):e00014-8.

[94] Muok AR, Claessen D, Briegel A. Microbial hitchhiking: how Streptomyces spores are transported by motile soil bacteria. ISME J. 2021;15:2591-600.

[95] Seymour JR, Brumley DR, Stocker R, Raina JB. Swimming towards each other: the role of chemotaxis in bacterial interactions. Trends Microbiol. 2024 Jul;32(7):640-9.

[96] Brinkmann S, Kurz M, Patras MA, Hartwig C, Marner M, Leis B, et al. Genomic and Chemical Decryption of the Bacteroidetes Phylum for Its Potential to Biosynthesize Natural Products. Microbiol Spectr. 2022 Jun;10(3):e0247921.

[97] Sangkhobol V, Skerman VBD. Chitinophaga, a new genus of chitinolytic myxobacteria. Int J Syst Evol Microbiol. 1981;31(3):285-93.

[98] Reichenbach H. The Order Cytophagales. In: Balows A, Trüper HG, Dworkin M, Harder W, Schleifer KH, editors. The Prokaryotes. New York, NY: Springer; 1992. p. 3631-75.

[99] Glavina Del Rio T, Abt B, Spring S, Lapidus A, Nolan M, Tice H, et al. Complete genome sequence of Chitinophaga pinensis type strain (UQM 2034). Stand Genomic Sci. 2010 Feb;2(1):87-95.

[100] Kaplan M, Chreifi G, Metskas LA, Liedtke J, Wood CR, Oikonomou CM, et al. In situ imaging of bacterial outer membrane projections and associated protein complexes using electron cryo-tomography. Elife. 2021 Sep;10:e73099.

[101] Schneider CA, Rasband WS, Eliceiri KW. NIH Image to ImageJ: 25 years of image analysis. Nat Methods. 2012 Jul;9(7):671-5.

[102] Bates D, Mächler M, Bolker B, Walker S. Fitting Linear Mixed-Effects Models Using lme4. Journal of Statistical Software. 2015;67(1):1-48.

[103] Kuznetsova A, Brockhoff PB, Christensen RHB. lmerTest Package: Tests in Linear Mixed Effects Models. Journal of Statistical Software. 2017;82(13):1-26.

[104] Lenth RV, Banfai B, Bolker B, Buerkner P, Giné-Vázquez I, Herve M, et al. emmeans: Estimated Marginal Means, aka Least-Squares Means. Comprehensive R Archive Network (CRAN); 2024. R package version 1.10.6.

[105] Xiong Q, Morphew MK, Schwartz CL, Hoenger AH, Mastronarde DN. CTF determination and correction for low dose tomographic tilt series. J Struct Biol. 2009 Dec;168(3):378-87.

[106] Pham HT, Parkinson JS. Phenol sensing by Escherichia coli chemoreceptors: a nonclassical mechanism. J Bacteriol. 2011 Dec;193(23):6597-604.

[107] Sly LI, Taghavi M, Fegan M. Phylogenetic position of Chitinophaga pinensis in the Flexibacter-Bacteroides-Cytophaga phylum. Int J Syst Bacteriol. 1999 Apr;49(Pt 2):479-81.

[108] McDonald MD, Owusu-Ansah C, Ellenbogen JB, Malone ZD, Ricketts MP, Frolking SE, et al. What is microbial dormancy? Trends Microbiol. 2024 Feb;32(2):142-50. Epub 2023 Sep 7.

[109] Justice SS, Hunstad DA, Seed PC, Hultgren SJ. Filamentation by Escherichia coli subverts innate defenses during urinary tract infection. Proc Natl Acad Sci U S A. 2006 Dec;103(52):19884-9.

[110] Campey A, Chait R, Tsaneva-Atanasova K, Pagliara S. Antibiotic resistant bacteria survive treatment by doubling while shrinking. bioRxiv [Preprint]. 2024 Jun.

[111] Justice SS, Hunstad DA, Cegelski L, Hultgren SJ. Morphological plasticity as a bacterial survival strategy. Nat Rev Microbiol. 2008 Feb;6(2):162-8.

[112] Rizzo MG, De Plano LM, Franco D. Regulation of filamentation by bacteria and its impact on the productivity of compounds in biotechnological processes. Appl Microbiol Biotechnol. 2020 Jun;104(11):4631-42.

[113] Karasz DC, Weaver AI, Buckley DH, Wilhelm RC. Conditional filamentation as an adaptive trait of bacteria and its ecological significance in soils. Environ Microbiol. 2022 Jan;24(1):1-17.

[114] Shah V, Zhao X, Lundeen RA, Ingalls AE, Nicastro D, Morris RM. Morphological Plasticity in a Sulfur-Oxidizing Marine Bacterium from the SUP05 Clade Enhances Dark Carbon Fixation. mBio. 2019 May;10(3):e00216-9.

[115] Ultee E, Ramijan K, Dame RT, Briegel A, Claessen D. Stress-induced adaptive morphogenesis in bacteria. Adv Microb Physiol. 2019;74:97-141.

[116] Xavier JB. Social interaction in synthetic and natural microbial communities. Mol Syst Biol. 2011 Apr 12;7:483.

[117] Santamaria G, Liao C, Lindberg C, Chen Y, Wang Z, Rhee K, et al. Evolution and regulation of microbial secondary metabolism. Elife. 2022 Nov;11:e76119.

[118] Wucher BR, Bartlett TM, Hoyos M, Papenfort K, Persat A, Nadell CD. Vibrio cholerae filamentation promotes chitin surface attachment at the expense of competition in biofilms. Proc Natl Acad Sci U S A. 2019 Jul 9;116(28):14216-21.

[119] Nunan N, Schmidt H, Raynaud X. The ecology of heterogeneity: soil bacterial communities and C dynamics. Philos Trans R Soc Lond B Biol Sci. 2020 May;375(1798):20190249.

[120] Tran TD, Ali MA, Lee D, et al. Bacterial filamentation as a mechanism for cell-to-cell spread within an animal host. Nat Commun. 2022 Feb;13(1):693.

[121] Lyons NA, Kolter R. A single mutation in rapP induces cheating to prevent cheating in Bacillus subtilis by minimizing public good production. Commun Biol. 2018 Sep;1:133.

[122] Weart RB, Lee AH, Chien AC, Haeusser DP, Hill NS, Levin PA. A metabolic sensor governing cell size in bacteria. Cell. 2007 Jul 27;130(2):335-47.

[123] McBride MJ, Zhu Y. Gliding motility and Por secretion system genes are widespread among members of the phylum bacteroidetes. J Bacteriol. 2013 Jan;195(2):270-8.

[124] Samad T, Billings N, Birjiniuk A, et al. Swimming bacteria promote dispersal of non-motile staphylococcal species. ISME J. 2017;11:1933-7.

[125] Li C, Hurley A, Hu W, et al. Social motility of biofilm-like microcolonies in a gliding bacterium. Nat Commun. 2021;12:5700.

[126] Engelhardt IC, Patko D, Liu Y, et al. Novel form of collective movement by soil bacteria. ISME J. 2022;16:2337-47.

[127] Kearns DB. A field guide to bacterial swarming motility. Nat Rev Microbiol. 2010 Sep;8(9):634-44.

[128] Ariel G, Rabani A, Benisty S, et al. Swarming bacteria migrate by Lévy Walk. Nat Commun. 2015;6:8396.

[129] Meacock OJ, Doostmohammadi A, Foster KR, et al. Bacteria solve the problem of crowding by moving slowly. Nat Phys. 2021;17:205-10.

[130] Xavier JB, Kim W, Foster KR. A molecular mechanism that stabilizes cooperative secretions in Pseudomonas aeruginosa. Mol Microbiol. 2011 Jan;79(1):166-79.

[131] Sudo SZ, Dworkin M. Resistance of vegetative cells and microcysts of Myxococcus xanthus. J Bacteriol. 1969 Jun;98(3):883-7.

[132] Chen S, Bagdasarian M, Kaufman MG, Walker ED. Characterization of strong promoters from an environmental Flavobacterium hibernum strain by using a green fluorescent protein-based reporter system. Appl Environ Microbiol. 2007 Feb;73(4):1089-100.

[133] Agarwal S, Hunnicutt DW, McBride MJ. Cloning and characterization of the Flavobacterium johnsoniae (Cytophaga johnsonae) gliding motility gene, gldA. Proc Natl Acad Sci U S A. 1997 Oct;94(22):12139-44.

[134] Brundrett MC. Global Diversity and Importance of Mycorrhizal and Nonmycorrhizal Plants. In: Tedersoo L, editor. Biogeography of Mycorrhizal Symbiosis. vol. 230 of Ecological Studies. Cham: Springer; 2017. p. 533-56.

[135] Noë R, Kiers ET. Mycorrhizal markets, firms, and co-ops. Trends Ecol Evol. 2018;33(10):777-89.

[136] Zhang L, Zhou J, George TS, Limpens E, Feng G. Arbuscular mycorrhizal fungi conducting the hyphosphere bacterial orchestra. Trends Plant Sci. 2022 Apr;27(4):402-11. Epub 2021 Nov 13.

[137] Anckaert A, Declerck S, Poussart LA, Lambert S, Helmus C, Boubsi F, et al. The biology and chemistry of a mutualism between a soil bacterium and a mycorrhizal fungus. Current Biology. 2024 Nov;34(21):4934-50.e8.

[138] Dudhane M, Borde M, Thomas S. Advances in AMF Research: Isolation, Histochemical Staining, Enumeration, Morphological and Molecular Techniques. In: Parihar M, Rakshit A, Adholeya A, Chen Y, editors. Arbuscular Mycorrhizal Fungi in Sustainable Agriculture: Inoculum Production and Application. Singapore: Springer; 2024. p. 23-48.

[139] Ivanov S, Austin Jn, Berg RH, Harrison MJ. Extensive membrane systems at the host-arbuscular mycorrhizal fungus interface. Nat Plants. 2019 Feb;5(2):194-203. Epub 2019 Feb 8.

[140] Roth R, Hillmer S, Funaya C, Chiapello M, Schumacher K, Lo Presti L, et al. Arbuscular cell invasion coincides with extracellular vesicles and membrane tubules. Nat Plants. 2019 Feb;5(2):204-11.

[141] Kuga Y, Saito K, Nayuki K, Peterson RL, Saito M. Ultrastructure of rapidly frozen and freeze-substituted germ tubes of an arbuscular mycorrhizal fungus and localization of polyphosphate. New Phytol. 2008 Jan;178(1):189-200.

[142] Grandmaison J, Benhamou N, Furlan V, Visser SA. Ultrastructural localization of N-acetylglucosamine residues in the cell wall of Gigaspora margarita throughout its life-cycle. Biol Cell. 1988;63(1):89-100.

[143] Kokkoris V, Banchini C, Paré L, Abdellatif L, Séguin S, Hubbard K, et al. Rhizophagus irregularis, the model fungus in arbuscular mycorrhiza research, forms dimorphic spores. New Phytol. 2024;242:1771-84.

[144] Bonfante P, Bianciotto V, Ruiz-Lozano JM, Minerdi D, Lumini E, Perotto S. Arbuscular Mycorrhizal Fungi and Their Endobacteria. In: Seckbach J, editor. Symbiosis. vol. 4 of Cellular Origin, Life in Extreme Habitats and Astrobiology. Dordrecht: Springer; 2001. p. 645-57.

[145] Maia LC, Kimbrough JW, Erdos G. Problems with fixation and embedding of arbuscular mycorrhizal fungi, Glomales. Mycologia. 1993;85(2):323-30.

[146] Nayuki K, Chen B, Ohtomo R, Kuga Y. Cellular imaging of cadmium in resin sections of arbuscular mycorrhizas using synchrotron micro X-ray fluorescence. Microbes Environ. 2014 Feb;29(1):60-6.

[147] Dumoux M, Glen T, Smith JLR, Ho EML, Perdigão LMA, Pennington A, et al. Cryo-plasma FIB/SEM volume imaging of biological specimens. Elife. 2023 Feb;12:e83623.

[148] Goh D, Martin JGA, Banchini C, MacLean AM, Stefani F. RocTest: A standardized method to assess the performance of root organ cultures in the propagation of arbuscular mycorrhizal fungi. Front Microbiol. 2022 Jul;13:937912.

[149] Doner LW, Bécard G. Solubilization of gellan gels by chelation of cations. Biotechnol Tech. 1991;5:25-8.

[150] Kelley K, Raczkowski AM, Klykov O, et al. Waffle Method: A general and flexible approach for improving throughput in FIB-milling. Nat Commun. 2022;13:1857.

[151] Rahman MM, Chang IY, Cohen-Fix O, Narayan K. A Workflow for High-pressure Freezing and Freeze Substitution of the Caenorhabditis elegans Embryo for Ultrastructural Analysis by Conventional and Volume Electron Microscopy. Bio Protoc. 2021 Apr;11(7):e3981.

[152] Schiøtz OH, Kaiser CJO, Klumpe S, et al. Serial Lift-Out: sampling the molecular anatomy of whole organisms. Nat Methods. 2024;21:1684-92.

[153] Klumpe S, Fung HK, Goetz SK, Zagoriy I, Hampoelz B, Zhang X, et al. A modular platform for automated cryo-FIB workflows. Elife. 2021 Dec;10:e70506.

[154] Chang IY, Rahman M, Harned A, Cohen-Fix O, Narayan K. Cryo-fluorescence microscopy of high-pressure frozen *C. elegans* enables correlative FIB-SEM imaging of targeted embryonic stages in the intact worm. Methods Cell Biol. 2021 Nov;162:223-52.

[155] Cole L, Davies D, Hyde GJ, Ashford AE. ER-Tracker dye and BODIPY-brefeldin A differentiate the endoplasmic reticulum and golgi bodies from the tubular-vacuole system in living hyphae of *Pisolithus tinctorius.* J Microsc. 2000 Mar;197(Pt 3):239-49.

[156] Liu S, Pokrovskaya ID, Storrie B. High-Pressure Freezing Followed by Freeze Substitution: An Optimal Electron Microscope Technique to Study Golgi Apparatus Organization and Membrane Trafficking. In: Wang Y, Lupashin VV, Graham TR, editors. Golgi. vol. 2557 of Methods in Molecular Biology. New York, NY: Humana; 2023. p. 211-23.

[157] Franzisky BL, Zhang X, Burkhardt CJ, Majorovits E, Hummel E, Schertel A, et al. Application of cryo-FIB-SEM for investigating ultrastructure in guard cells of higher plants. Plant Physiol Biochem. 2025 Mar;220:109546.

[158] Hylton RK, Swulius MT. Challenges and triumphs in cryo-electron tomography. iScience. 2021 Aug 8;24(9):102959.

[159] Al-Amoudi A, Studer D, Dubochet J. Cutting artefacts and cutting process in vitreous sections for cryo-electron microscopy. J Struct Biol. 2005 Apr;150(1):109-21.

[160] Mahamid J, Schampers R, Persoon H, Hyman AA, Baumeister W, Plitzko JM. A focused ion beam milling and lift-out approach for site-specific preparation of frozen-hydrated lamellas from multicellular organisms. J Struct Biol. 2015 Nov;192(2):262-9.

[161] Burnett TL, Kelley R, Winiarski B, Contreras L, Daly M, Gholinia A, et al. Large volume serial section tomography by Xe Plasma FIB dual beam microscopy. Ultramicroscopy. 2016 Feb;161:119-29.

[162] Zhong X, Wade CA, Withers PJ, Zhou X, Cai C, Haigh SJ, et al. Comparing Xe^+ pFIB and Ga^+ FIB for TEM sample preparation of Al alloys: Minimising FIB-induced artefacts. J Microsc. 2021 May;282(2):101-12.

[163] Depelteau JS. Development and application of cryo-EM tools to study the ultrastructure of microbes in changing environments. Leiden, The Netherlands: Leiden University; 2022. PhD thesis.

[164] Yaroslavsky AN, Feng X, Muzikansky A, et al. Fluorescence Polarization of Methylene Blue as a Quantitative Marker of Breast Cancer at the Cellular Level. Sci Rep. 2019;9:940.

[165] Otegui MS, Pennington JG. Electron tomography in plant cell biology. Microscopy (Oxf). 2019 Feb 1;68(1):69-79.

[166] Pöge M, Dickmanns M, Xu P, Li M, Schiøtz OH, Kaiser COJ, et al. Making plant tissue accessible for cryo-electron tomography. bioRxiv [Preprint]. 2025 Feb:2025.02.14.638237.

[167] Houston K, Tucker MR, Chowdhury J, Shirley N, Little A. The Plant Cell Wall: A Complex and Dynamic Structure As Revealed by the Responses of Genes under Stress Conditions. Front Plant Sci. 2016 Aug;7:984.

[168] Ulrich L, Giez C, Steiner LX, Hentschel U, Lachnit T. Adaptive lifestyle of bacteria determines phage-bacteria interaction. Front Microbiol. 2022 Dec;13:1056388.

[169] Ongenae V, Mabrouk AS, Crooijmans M, Rozen D, Briegel A, Claessen D. Reversible bacteriophage resistance by shedding the bacterial cell wall. Open Biol. 2022 Jun;12(6):210379.

[170] Middelboe M, Traving SJ, Castillo D, Kalatzis PG, Glud RN. Prophage-encoded chitinase gene supports growth of its bacterial host isolated from deep-sea sediments. ISME J. 2025 Jan;19(1):wraf004.

[171] Filipiak M, Łoś JM, Łoś M. Efficiency of induction of Shiga-toxin lambdoid prophages in Escherichia coli due to oxidative and antibiotic stress depends on the combination of prophage and the bacterial strain. Journal of Applied Genetics. 2020 Feb;61(1):131-40.

[172] Song W, Sun HX, Zhang C, Cheng L, Peng Y, Deng Z, et al. Prophage Hunter: an integrative hunting tool for active prophages. Nucleic Acids Res. 2019;47(W1):W74-80.

[173] Zhou Y, Liang Y, Lynch KH, Dennis JJ, Wishart DS. PHAST: a fast phage search tool. Nucleic Acids Res. 2011;39(Web Server issue):W347-52.

[174] Arndt D, Grant JR, Marcu A, Sajed T, Pon A, Liang Y, et al. PHASTER: a better, faster version of the PHAST phage search tool. Nucleic Acids Research. 2016 Jul;44(W1):W16-21.

[175] Arndt D, Marcu A, Liang Y, Wishart DS. PHAST, PHASTER and PHASTEST: Tools for finding prophage in bacterial genomes. Briefings in Bioinformatics. 2019;20(4):1560-7.

[176] Mazzocco A, Waddell TE, Lingohr E, Johnson RP. Enumeration of Bacteriophages Using the Small Drop Plaque Assay System. In: Clokie MR, Kropinski AM, editors. Bacteriophages. vol. 501 of Methods in Molecular Biology^{TM}. Humana Press; 2009. p. 81-5.

[177] Stenholm AR, Dalsgaard I, Middelboe M. Isolation and Characterization of Bacteriophages Infecting the Fish Pathogen Flavobacterium psychrophilum. Appl Environ Microbiol. 2008 May;74(13):4070-8.

[178] Wang X, Tang Y, Yue X, Wang S, Yang K, Xu Y, et al. The role of rhizosphere phages in soil health. FEMS Microbiol Ecol. 2024 Apr;100(5):fiae052.

[179] Sirén K, Millard A, Petersen B, Gilbert MTP, Clokie MRJ, Sicheritz-Pontén T. Rapid discovery of novel prophages using biological feature engineering and machine learning. NAR Genom Bioinform. 2021 Jan;3(1):lqaa109.

[180] Silpe JE, Duddy OP, Bassler BL. Induction mechanisms and strategies underlying interprophage competition during polylysogeny. PLoS Pathog. 2023 May;19(5):e1011363.

[181] Silpe JE, Duddy OP, Johnson GE, Beggs GA, Hussain FA, Forsberg KJ, et al. Small protein modules dictate prophage fates during polylysogeny. Nature. 2023 Aug;620(7974):625-33.

[182] Backman T, Latorre SM, Symeonidi E, Muszyński A, Bleak E, Eads L, et al. A phage tail-like bacteriocin suppresses competitors in metapopulations of pathogenic bacteria. Science. 2024 Jun;384(6701):eado0713.

[183] Sun M, Yuan S, Xia R, Ye M, Balcázar JL. Underexplored viral auxiliary metabolic genes in soil: Diversity and eco-evolutionary significance. Environ Microbiol. 2023 Apr;25(4):800-10.

[184] Assmus B, Hutzler P, Kirchhof G, Amann R, Lawrence JR, Hartmann A. In Situ Localization of Azospirillum brasilense in the Rhizosphere of Wheat with Fluorescently Labeled, rRNA-Targeted Oligonucleotide Probes and Scanning Confocal Laser Microscopy. Appl Environ Microbiol. 1995 Mar;61(3):1013-9.

[185] Kiers ET, Rousseau RA, West SA, Denison RF. Host sanctions and the legume-rhizobium mutualism. Nature. 2003 Sep 4;425(6953):78-81.

[186] Vierheilig H. Further root colonization by arbuscular mycorrhizal fungi in already mycorrhizal plants is suppressed after a critical level of root colonization. J Plant Physiol. 2004 Mar;161(3):339-41.

[187] Goss WA, Deitz WH, Cook TM. Mechanism of action of nalidixic acid on Escherichia coli. II. Inhibition of deoxyribonucleic acid synthesis. J Bacteriol. 1965 Apr;89(4):1068-74.

[188] Deitz WH, Cook TM, Goss WA. Mechanism of action of nalidixic acid on Escherichia coli. 3. Conditions required for lethality. J Bacteriol. 1966 Feb;91(2):768-73.

CURRICULUM VITÆ

Janine Liedtke was born in Berlin, Germany, in 1983. She studied Biology at the Freie Universität Berlin and obtained her B.Sc. in 2012. She continued her studies in microbiology at the Rheinische Friedrich-Wilhelms-Universität Bonn, earning her M.Sc. degree in 2015. During her master's studies, she participated in the Erasmus programme at the University of Bergen, Norway (2013–2014), focusing on environmental and food microbiology.

From 2016 to 2018, she worked at the European Space Research and Technology Centre (ESTEC) in the Netherlands, contributing to ESA's MELiSSA project on microbial life support systems for long-term space missions, as well as to activities within the Human Spaceflight and Robotic Exploration department.

Between 2018 and 2020, she worked at the Norwegian University of Life Sciences (NMBU) on the *Bacillus cereus* endospore appendages project in the field of food safety. She performed method development for the extraction and purification of non-soluble spore surface structures for further structural investigation and conducted a short-term research visit at Vrije Universiteit Brussel in Belgium in 2019, focusing on structural investigation techniques by cryo-EM.

In 2020, she joined the Microbial Ultrastructure group led by Prof. Ariane Briegel at Leiden University to pursue her PhD. Her research focused on the structural investigation of plant-associated microbiota and the development of workflows for large-volume biological sample preparation for cryo-electron tomography (cryo-ET).

From January to March 2024, she conducted a research visit at the Central European Institute of Technology (CEITEC) in Brno, Czech Republic, in the group of Jiří Nováček, Ph.D. There, she worked on PFIB/SEM instruments and developed workflows for high-resolution imaging of cryofixed samples, including plant tissue, and arbuscular mycorrhizal fungi. She optimized her experimental design and cryo-electron microscopy techniques to establish reproducible protocols for future studies.

LIST OF PUBLICATIONS

1. **Liedtke, J.**, Rodenburg, F., Du, C., Zhang, L., van Wezel, G. P., & Briegel, A. (2025). Morphological plasticity of endophytic *Chitinophaga pinensis*. *bioRxiv*, 2025.07.09.663833. https://doi.org/10.1101/2025.07.09.663833. (preprint)
2. Munar-Palmer, M., Santamaría-Hernando, S., **Liedtke, J.**, Ortega, D. R., López-Torrejón, G., Rodríguez-Herva, J. J., Briegel, A., & López-Solanilla, E. (2024). Chemosensory systems interact to shape relevant traits for bacterial plant pathogenesis. mBio, 15(7), e0087124. https://doi.org/10.1128/mbio.00871-24.
3. **Liedtke, J.**, Depelteau, J. S., & Briegel, A. (2022). How advances in cryo-electron tomography have contributed to our current view of bacterial cell biology. Journal of Structural Biology X, 6, 100065. https://doi.org/10.1016/j.yjsbx.2022.100065.
4. Kaplan, M., Chreifi, G., Metskas, L. A., **Liedtke, J.**, Wood, C. R., Oikonomou, C. M., Nicolas, W. J., Subramanian, P., Zacharoff, L. A., Wang, Y., Chang, Y. W., Beeby, M., Dobro, M. J., Zhu, Y., McBride, M. J., Briegel, A., Shaffer, C. L., & Jensen, G. J. (2021). In situ imaging of bacterial outer membrane projections and associated protein complexes using electron cryo-tomography. eLife, 10, e73099. https://doi.org/10.7554/eLife.73099.
5. **Liedtke, J.***, Pradhan, B.*, Sleutel, M., Lindbäck, T., Zegeye, E. D., O'Sullivan, K., Llarena, A. K., Brynildsrud, O., Aspholm, M., & Remaut, H. (2021). Endospore Appendages: a novel pilus superfamily from the endospores of pathogenic Bacilli. EMBO Journal, 40(17), e106887. https://doi.org/10.15252/embj.2020106887. (*shared first authorship)
6. Weber, M., **Liedtke, J.**, Plattes, S., & Lipski, A. (2019). Bacterial community composition of biofilms in milking machines of two dairy farms assessed by a combination of culture-dependent and -independent methods. PLOS ONE, 14(9), e0222238. https://doi.org/10.1371/journal.pone.0222238.
7. Brinkert, K., Akay, Ö., Richter, M. H., **Liedtke, J.**, Giersig, M., Fountaine, K. T., & Lewerenz, H.-J. (2019). Experimental methods for efficient solar hydrogen production in microgravity environment. Journal of Visualized Experiments, 154, e59122. https://doi.org/10.3791/59122.
8. Brinkert, K., Richter, M. H., Akay, Ö., **Liedtke, J.**, Giersig, M., Fountaine, K. T., & Lewerenz, H.-J. (2018). Efficient solar hydrogen generation in microgravity environment. Nature Communications, 9(1), 2527. https://doi.org/10.1038/s41467-018-04968-w.
9. **Liedtke, J.**, & Vahjen, W. (2012). In vitro antibacterial activity of zinc oxide on a broad range of reference strains of intestinal origin. Veterinary Microbiology, 160(1-2), 251-255. https://doi.org/10.1016/j.vetmic.2012.05.013.

ISBN 978-94-6496-461-5